Modeling and Simulation of Nano-Porous Media and Heat Transfer at High Knudsen Numbers for Applications in Vacuum Insulation Panels with Lattice Boltzmann Methods

Zur Erlangung des akademischen Grades eines

DOKTORS DER INGENIEURWISSENSCHAFTEN (DR.-ING.)

von der KIT-Fakultät für Chemieingenieurwesen und Verfahrenstechnik des
Karlsruher Instituts für Technologie (KIT)
genehmigte

DISSERTATION

von
M. Sc. Jesse Ross-Jones
aus Caracas, Venezuela

Tag der mündlichen Prüfung: 12.01.2021

Referent: Prof. Dr. Matthias Rädle
Korreferent: Prof. Dr.-Ing. Hermann Nirschl
Korreferent: Dr. rer. nat. Mathias J. Krause

Summary

New materials for improved thermal insulation are required in order to reach and surpass the current goal of a 32.5 % increase in energy efficiency by 2030 (EU 2030 climate & energy framework). Potential candidates for new insulation materials are Vacuum Insulation Panels (VIPs), which provide five to ten times improvement in insulation performance. With an Effective Thermal Conductivity (ETC) between 0.004 and 0.008 W/mK, VIPs combine superior thermal insulation performance with a reduction in the space required by the insulation. Improvements to the VIP, such as reduction of the cost of the structural media and increase the lifetime of the panels, are required to increase market adoption.

VIP cores are composed of complex particle systems. In this work, investigation into precipitated silica was performed with the goal of increasing the internal system pressure of VIPs. By maximizing the minimum required pressure inside the VIP while maintaining a low effective thermal conductivity, not only can the lifetime of the panel be extended, this would also decrease the unwanted thermal conductivity rise of a damaged panel. However, not all particle parameters and their influence on insulation performance are entirely understood. Therefore, this work is a multi-scale approach towards increased understanding of precipitated silica and its use as a vacuum insulation media.

In order to understand effects of different packing geometry such as porosity and aggregate size on the individual contributions that make up the heat transfer through the VIP, a high fidelity model of the packing geometry is required. A measurement system and two independent numerical simulations were developed, one based on Mie Static Light Scattering (SLS) and the other on Montecarlo Light Scattering (MLS), for use in obtaining further understanding of the silica's aggregate size and form. The SLS automated laboratory apparatus measures light scattering intensity over a range

of angles from 20° to 160°. Through subsequent data analysis the characterization of particle size and form is obtained. The MLS numerical simulations for light scattering are initially performed and tested with spherical particles and compared to Mie simulations, thereafter they are used for elliptical particles. The MLS numerical simulations are able to evaluate light scattering for any convex form, which is not possible with Mie light scattering simulations.

Following, a method was developed and implemented for numerical modeling of the silica agglomerate geometry based on silica measurements from Small Angle X-Ray Scattering (SAXS), Mercury Intrusion Porosimetry (MIP) and Analytical Ultra-centrifugation (AUC). A procedural workflow to generate mesoscopic geometries of precipitated silica was developed whereby the input parameters for the geometry generation include primary particle size, primary pore size, aggregate diameter, shape and standard deviation, as well as overall packing porosity. The generated geometries are periodic in all axis directions, and are further analyzed to obtain a pore size distribution.

Lastly, using the generated geometry, heat transfer through the nano-porous geometries is simulated using Lattice Boltzmann Methods (LBMs), including heat transfer due to radiation as well as conduction through solid and fluid components. Radiation and conduction are coupled to simulate heat transfer at the nano-scale for a range of pressures, from 1 bar down to 10 mbar. This enables an in depth understanding of the heat transfer mechanism at the nano-scale and leads to both an improvement in the lifetime and reduction of the manufacturing costs of VIPs. To simulate heat transfer, the open source implementation of LBM, OpenLB, is used with a parallel execution capable of handling the complex geometry generated in this work. Additional algorithms and test cases were developed for continuous normal implementations in two and three dimensions which can be used for future slip boundary implementations.

Using the SLS measurement system, silica particles of sizes 314 nm, 407 nm, 507 nm, 546 nm, 640 nm, 681 nm, 726 nm, 812 nm, 900 nm and 987 nm were measured. The subsequent curve fitting demonstrated an accuracy within 5 % for silica particles of diameter 314 nm, 507 nm, 681 nm, 900 nm and 987 nm. The remaining silica particles of diameter 407 nm, 546 nm, 640 nm and 812 nm, while not accurately characterized, demonstrate close resemblance to their numerical counterparts. Furthermore, the particle form was estimated for 500 nm particles using SLS, whereby the estimated diameter along the z-axis was 585 nm. MLS numerical simulations were conducted for spherical particles of radii: 10 nm, 50 nm, 100 nm, 150 nm and 200 nm and the resulting scattering patterns are presented and compared to Mie simulations. The

results demonstrate particularly good agreement with the results of Mie scattering for the same particle diameter. Furthermore, MLS numerical simulations were conducted for an ellipsoidal particle, with a long axis radius $r_z = 200\,\text{nm}$ and short axis radii of $r_x = r_y = 50\,\text{nm}$, at various angles of rotation. The resulting scattering patterns are presented and discussed.

The geometry generation was evaluated by calculating the pore size distributions, with results demonstrating acceptable agreement with measurements of the silica samples (KS, CP and GT). Moreover, the pore distance calculation was validated against an analytical solution for a cubic ordered packing of spherical particles. Part of the pore distribution evaluation includes reduction of pore diameters for overlapping pores. The performance of this algorithm is evaluated and a clear advantage is apparent from the provided implementation over a brute force implementation where each pore is checked for overlap with every other pore. The implementation grows linearly with increasing number of pores, while the brute force method grows exponentially.

Two sets of heat transfer studies are conducted using the numerically generated precipitated silica media. The initial study uses a globally defined pore size, whereas in the subsequent study, the local pore size and local Knudsen number is evaluated. Both studies numerically simulate the effective heat transfer through the generated three-dimensional packing of silica particles. The numerically evaluated ETCs for the precipitated silica are compared to measurements as well as to literature values for VIPs. Using a globally defined pore size the ETC was underestimated for lower system pressures. By extending the method to evaluate the local Knudsen number and therefore the local heat transfer within nano-pores, the ETC closely predicts measured values at lower pressures. A discrepancy however appears at higher pressures and is primarily due to the lack of larger pores in the numerical geometry, in the order of 200 nm and above. Despite the lack of larger pores, the effective heat conductivities predicted follow the trends reported in literature, with KS having the highest thermal conductivity at ambient pressure of $20.78\,\text{mW/(m\,K)}$, followed by GT at $19.29\,\text{mW/(m\,K)}$ and CP at $16.4\,\text{mW/(m\,K)}$. The implementations were tested for mesh sensitivity and the Error of Convergence (EOC) are evaluated.

The methodology presented is able to numerically estimate heat transfer due to radiation and conduction through both the nano-porous silica particles and the surrounding fluid over a range of pressures, from 1 bar to 10 mbar. Thus, this work presents an automated numerical method, featuring direct control and tuning of the desired microstructure parameters, to obtain a complete methodological pathway from measured particle characteristics to the resulting effective macroscopic heat transfer.

Zusammenfassung

Neue Materialien für eine verbesserte Wärmedämmung sind erforderlich, um das aktuelle Ziel einer Steigerung der Energieeffizienz um 32,5 % bis 2030 zu erreichen oder gar zu übertreffen (EU klima- und energiepolitischer Rahmen bis 2030). Potenzielle Kandidaten für neue Dämmmaterialien sind Vacuum Isolationspanelen (VIPs), die eine fünf- bis zehnfache Verbesserung der Dämmleistung bieten. Mit einer effektiven Leitfähigkeit (ETC) von 0,004 bis 0,008 W/mK vereinen VIPs eine optimierte Wärmedämmleistung bei gleichzeitiger Reduzierung des Platzbedarfs. Um die Marktakzeptanz zu erhöhen, müssen unter anderem die Kosten für die strukturellen Medien reduziert und die Lebensdauer der Paneele erhöht werden.

VIPs bestehen aus ein komplex aufgebauten partikulären Systemen. In dieser Arbeit wird die Verwendung von gefällter Kieselsäure untersucht, mit dem Ziel die Erhöhung des internen Systemdruck von VIPs zu realisieren. Durch die Maximierung des minimal erforderlichen Drucks im VIP, bei gleichzeitiger Beibehaltung einer niedrigen effektiven Wärmeleitfähigkeit, kann nicht nur die Lebensdauer der Panele verlängert werden, sondern auch den unerwünschten Anstieg der Wärmeleitfähigkeit einer beschädigten Panele verringert werden. Da nicht alle Partikelparameter und ihr Einfluss auf die Dämmleistung vollständig verstanden sind, verfolgt diese Arbeit ein mehrskaliger Ansatz für ein besseres Verständnis von gefällter Kieselsäure und ihrer Verwendung als Vakuumisolationsmedium.

Um die Auswirkungen unterschiedlicher Packungsgeometrien, wie Porosität und Aggregatgröße, auf die einzelnen Teile des Wärmeübergangs durch das VIP zu verstehen, ist ein hochgenaues Modell der Packungsgeometrie erforderlich. Um ein besseres Verständnis der Aggregatgröße und -form der Kieselsäure zu erhalten, wird ein Messsystem und zwei numerische Simulationen entwickelt, die zum einen auf statischer Mie Lichtstreuung (SLS) und zum anderen auf Montecarlo-Modellen der Lichtstreuung

(MLS) basieren. Das automatisierte SLS Laborgerät misst die Lichtstreuungsinten-sität über einen Winkelbereich von 20° bis 160°. Durch anschließende Datenanalyse erfolgt die Charakterisierung von Partikelgröße und -form. Die numerischen MLS Simulationen für die Lichtstreuung werden zunächst an kugelförmigen Partikeln durchgeführt und getestet und mit Mie Simulationen verglichen, danach werden sie für elliptische Partikel verwendet. Die numerischen MLS Simulationen sind in der Lage die Lichtstreuung für jede konvexe Form zu berechnen, was mittels Mie Lichtstreuungssimulationen nicht möglich ist.

Anschließend wird eine Methode zur numerischen Modellierung der Partikelaggre-gaten innerhalb der komplexen Kieselsäuregeometrie entwickelt und implementiert, die auf Kieselsäuremessungen aus Kleinwinkel Röntgenstreuung (SAXS), Quecksilber Intrusionsporosimetrie (MIP) und analytischer Ultrazentrifugation (AUC) basiert. Es wird ein prozeduraler Arbeitsablauf zur Generierung mesoskopischer Geometrien von gefällter Kieselsäure entwickelt, unter Verwendung der Eingangsparameter für die Geometriegenerierung der Primärteilchengröße, Primärporengröße, Aggregat-durchmesser, -form und -standardabweichung sowie der Gesamtpackungsporosität. Die erzeugten Geometrien sind in allen Achsenrichtungen periodisch und werden analysiert, um eine Porengrößenverteilung zu erhalten.

Schließlich wird mittels der erzeugten Geometrien die Wärmeübertragung durch nanoporösen Geometrien, einschließlich der Wärmeübertragung durch Strahlung sowie der Konduktion durch feste und flüssige Komponenten, mittels Lattice Boltz-mann Methoden (LBM) simuliert. Strahlung und Konduktion werden gekoppelt, um die Wärmeübertragung auf der Nanoskala für einen Druckbereich von 1 bar bis hinunter zu 10 mbar zu simulieren. Dies ermöglicht ein vertieftes Verständnis des Wärmeübertragungsmechanismus auf der Nanoskala und führt perspektivisch sowohl zu einer Verbesserung der Lebensdauer als auch zu einer Senkung der Her-stellungskosten von VIPs. Zur Simulation der Wärmeübertragung wird die Open-Source-Implementierung von LBM, *OpenLB*, in paralleler Ausführung verwendet, die in der Lage ist, die in dieser Arbeit erzeugte komplexe Geometrie zu handhaben. Für kontinuierliche Normalimplementierungen in zwei und drei Dimensionen wurden zusätzliche Algorithmen und Testfälle entwickelt, die für zukünftige Gleitgrenzenim-plementierungen verwendet werden können.

Mit dem SLS-Messsystem wurden Kieselsäurepartikel der Größen 314 nm, 407 nm, 507 nm, 546 nm, 640 nm, 681 nm, 726 nm, 812 nm, 900 nm and 987 nm gemessen. Die Kurvenanpassung zeigt eine Genauigkeit von 5 % für Kieselsäurepartikel mit einem Durchmesser von 314 nm, 507 nm, 681 nm, 900 nm und 987 nm. Die verbleibenden

Siliziumdioxidpartikel mit einem Durchmesser von 407 nm, 546 nm, 640 nm und 812 nm konnten zwar nicht exakt charakterisiert werden, zeigten aber große Ähnlichkeit mit ihren numerischen Gegenstücken. Darüber hinaus wurde die Partikelform für 500 nm Partikel mittels SLS untersucht, wobei der geschätzte Durchmesser entlang der z-Achse 585 nm betragt. Numerische MLS Simulationen werden für kugelförmige Partikel mit Radien: 10 nm, 50 nm, 100 nm, 150 nm und 200 nm durchgeführt und die resultierenden Streumuster werden dargestellt und mit Mie Simulationen verglichen. Die Ergebnisse zeigen eine besonders gute Übereinstimmung mit den Ergebnissen der Mie Streuung bei gleichem Partikeldurchmesser. Darüber hinaus wurden MLS numerische Simulationen für ein ellipsoidisches Teilchen mit einem langen Achsenradius $r_z = 200$ nm und kurzen Achsenradien von $r_x = r_y = 50$ nm bei verschiedenen Drehwinkeln durchgeführt. Die resultierenden Streumuster werden vorgestellt und diskutiert.

Die Geometrieerzeugung wurde durch Berechnung der Porengrößenverteilungen charakterisiert, wobei die Ergebnisse eine akzeptable Übereinstimmung mit den Messungen der Silika-Proben zeigten (KS, CP und GT). Darüber hinaus wurde die Berechnung des Porenabstands anhand einer analytischen Lösung für eine kubisch geordnete Packung kugelförmiger Partikel validiert. Ein Teil der Auswertung der Porenverteilung umfasst die Reduzierung des Porendurchmessers für überlappende Poren. Die Leistung dieses Algorithmus wird evaluiert und es zeigt sich ein klarer Vorteil der bereitgestellten Implementierung gegenüber einer Brute-Force-Implementierung, bei der jede Pore auf Überlappung mit jeder anderen Pore überprüft wird. Die Implementierung wächst linear mit zunehmender Anzahl von Poren, während die Brute-Force-Methode exponentiell wächst.

Zwei Fallstudien zur Wärmeübertragung werden unter Verwendung der numerisch erzeugten Fällungskieselsäureaggregate durchgeführt. Zunächst wird eine global definierte Porengröße verwendet, während nachfolgend die lokale Porengröße und die lokale Knudsenzahl ausgewertet werden. Beide Studien simulieren numerisch die effektive Wärmeübertragung durch die erzeugte dreidimensionale Packung der Siliziumdioxidpartikel. Die numerisch ausgewerteten ETC für die gefällte Kieselsäure werden sowohl mit Messungen, als auch mit Literaturwerten für VIPs verglichen. Unter Verwendung einer global definierten Porengrösse wurden die ETC für niedrigere Systemdrücke unterschätzt. Durch die Erweiterung der Methode zur Bewertung der lokalen Knudsen-Zahl und damit des lokalen Wärmetransfers innerhalb von Nanoporen bestimmt das ETC die Messwerte bei niedrigeren Drücken genau. Eine Diskrepanz tritt jedoch bei höheren Drücken auf und ist in erster Linie auf das Fehlen größerer Poren

in der numerischen Geometrie, ab einer Größe von 200 nm, zurückzuführen. Trotz des Fehlens größerer Poren folgen die vorhergesagten effektiven Wärmeleitfähigkeiten den in der Literatur berichteten Trends, wobei KS die höchste Wärmeleitfähigkeit bei Umgebungsdruck von 20.78 mW/(m K) aufweist, gefolgt von GT bei 19.29 mW/(m K) und CP bei 16.4 mW/(m K). Die Implementierungen wurden auf Netzempfindlichkeit getestet und die Konvergenzordnung werden evaluiert.

Die vorgestellte Methodik ist in der Lage die Wärmeübertragung aufgrund von Strahlung und Konduktion sowohl durch die nanoporösen Siliziumdioxidpartikel als auch durch das Partikel umgebende Gas über einen Druckbereich von 1 bar bis 10 mbar numerisch abzuschätzen. Somit stellt diese Arbeit eine automatisierte numerische Methode vor, die eine direkte Kontrolle und Abstimmung der gewünschten Mikrostrukturparameter ermöglicht, um einen vollständigen methodischen Weg von den gemessenen Partikeleigenschaften bis zur resultierenden effektiven makroskopischen Wärmeübertragung zu erhalten.

Contents

Glossary

NEMS   Nanoelectromechanical Systems. 4, 9
NIST   National Institute of Standards and Technology. 81

PCM   Phase Change Material. 3, 9
PLA   Polylactic Acid. 14

ROI   Return on Investment. 5
RTE   Radiative Transfer Equation. 61

SAXS   Small Angle X-Ray Scattering. ii, 11–13, 39, 94, 95
SLS   Static Light Scattering. i, ii, xv, xvii, xviii, 9, 12, 13,
        15, 17, 20, 21, 23, 31–36, 93–96, 109

TDMS   Technical Data Management System. 15

VIP   Vacuum Insulation Panel. i–iii, xvi, 1, 3–6, 8, 9, 38,
        53, 55, 56, 58, 63–65, 77–79, 81, 85–87, 90, 91,
        96

Nomenclature

α Angle of rotation about vertical axis for Static Light Scattering (SLS) measurement

A Area

A_p Estimated particle area

An Negative area between $\dot{I}_M$ and $\dot{I}_Q$

Ap Positive area between $\dot{I}_M$ and $\dot{I}_Q$

β Angle of rotation about horizontal axis in SLS measurements

β_f Weighting factor representing the efficiency of energy transfer between fluid molecules and the solid boundaries

c Speed of light in a vacuum

C_{os} Number of negative intervals between $\dot{I}_M$ and $\dot{I}_Q$

C_{ss} Number of positive intervals between $\dot{I}_M$ and $\dot{I}_Q$

c_i Discrete lattice velocities

c_p Specific heat capacity

δ Estimated average pore size

d	Distance
d_{agg}	Average aggregate diameter
D_{mf}	Mass fractal dimension
d_p	Primary particle size
D_{sf}	Surface fractal dimension
d_{VIP}	Thickness of Vacuum Insulation Panel (VIP)
ϵ	Relative error
f_{os}	Relative occurrence of negative intervals between $\dot{I}_M$ and $\dot{I}_Q$
f_{ss}	Relative occurrence of positive intervals between $\dot{I}_M$ and $\dot{I}_Q$
f_S	Mass fraction
Γ	Domain boundary
d_{pore}	Primary pore size
I	Light intensity
$\dot{I}_M$	First derivative of the measured light intensity
$\dot{I}_Q$	First derivative of the analytical Mie light intensity
Kn	Knudsen number
λ	Wavelength
L	Lattice cell length
λ_C	Heat transfer through the coupling effect
λ_ϕ	Total effective heat transfer
λ_f	Heat transfer through fluid

λ_{f0} Heat transfer through fluid at 1 bar atmospheric pressure

λ_R Heat transfer through radiation

λ_S Heat transfer through solid

λ_{S0} Heat transfer through compacted solid

l_f Mean free path

μ Extinction coefficient

N Grid resolution

n Molecular density

n_o Refractive index

Ω Domain

p_f System pressure

$p_{1/2}$ Fluid pressure at half of the full gaseous thermal conductivity

ϕ Light intensity density

Φ Characteristic length

Π Packing porosity

Ψ Sphericity

q Heat flux

$\dot{Q}_L$ Power losses

$\dot{Q}_M$ Measured power

R_s Specific gas constant

r_x Particle radius on x-axis measured with SLS

r_y Particle radius on y-axis measured with SLS

r_z Particle radius on z-axis estimated with SLS

ρ Aspect ratio

ρ_f Fluid density

ρ_S Solid density

σ_B Stefan-Boltzmann constant

σ_a Absorption coefficient

σ_f Molecular diameter

σ_{agg} Standard deviation of the aggregate diameter

σ_s Scattering coefficient

τ Relaxation time

T Temperature

t Time

Δt Time step

v Speed of sound

V_p Estimated particle volume

w Frequency

w_i Discrete lattice direction weights

Δx Grid spacing

1

Introduction

1.1 Problem Statement

New materials for improved thermal insulation need to be developed in order to reach and surpass current goals of a 32.5% increase in energy efficiency by 2030 [23].

1.2 Motivation

Good potential candidates for insulation materials are Vacuum Insulation Panels (VIPs), seen in Figure 1.1, which provide five to tens times increase in thermal insulation performance, (0.004-0.008 W/(mK), see Table 1.1) [40], compared to traditional insulation materials. Due to this very low Effective Thermal Conductivity (ETC), space requirements for insulation can decrease five to ten times, meaning superior thermal insulation performance combined with a reduction in the space required by the insulation. However, in order to increase adoption, improvements to the panels need to be made, such as reduction of the cost of the structural media and increase in the lifetime of the thermal insulation panels.

Table 1.1: *Comparison of thermal conductivity λ_ϕ, and density of high performance thermal insulation materials [7] (EPS and XPS are expanded and extruded polystyrene respectively).*

Material	Thermal Conductivity λ_ϕ in W/mK	Density ρ_S in kg/m^3
Polystyrene (EPS, XPS)	0.034 - 0.036	15 - 30
Mineralwool	0.033 - 0.040	8 - 500
VIP	0.004 - 0.008	150 - 350
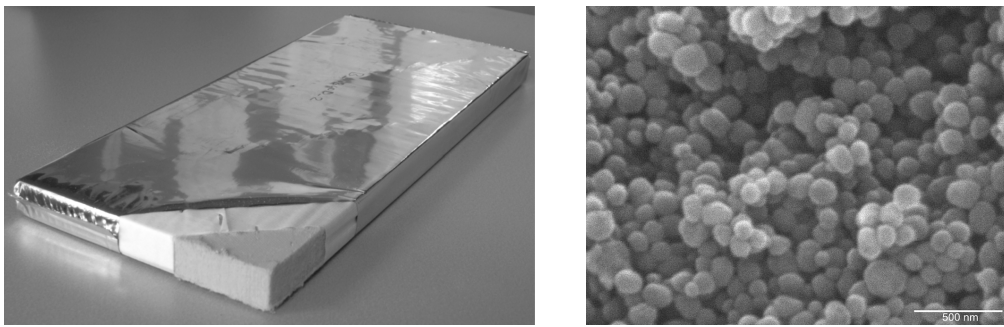
(a) *Vacuum insulation panel external structure [5].* **(b)** *Nano-silica structure, pore size: 50-500nm [87].*

Figure 1.1: *Composition of Vacuum Insulation Panel (VIP).*

1.3 Application

While improvements to energy efficiency are necessary in a wide range of areas, focus was placed on insulation of transport vehicles. By increasing the insulation performance of transportation vehicles, goods can be kept cool for longer periods of time. Furthermore, the space required by the insulation decreases. To provide a concrete example, in 1996, EU regulations were set such that vehicles must have a maximum width of 2.5 meters with the exception of those vehicles carrying goods, in which case the maximum width was increased to 2.55 meters [79]. Following, in 2015 this restriction was relaxed to 2.6 meters for conditioned vehicles or conditioned containers [80], due to additional space requirements of insulation materials. This is a 0.2 m^2 increase in frontal vehicle surface area (where the vehicle height is limited to 4 meters [79]). These dimensions were required to allow for two EU pallets (1.2 meters by 0.8 meters) to be loaded in parallel. Through the use of space-saving

VIPs, this additional vehicle width would be unnecessary, thus not only increasing the thermal efficiency of the transport vehicle, but increasing fuel efficiency as well.

An example of using a VIP in a cooling box application for transportation vehicles is show in Figure 1.2. Using precipitated silica as a core with an Expanded Polystyrene (EPS) frame and Glass Reinforced Plastic (GRP) sandwiching material, the cooling container was constructed. This construction took place at our partner's facility, KRESS Fahrzeugbau GmbH in Meckesheim, Germany. The construction incorporated a vacuum pump in order to recover the vacuum pressure periodically. To overcome the necessity of permanent connection to a vacuum pump, improved core materials can be used which no longer require lower vacuum pressures to maintain a low ETC. Not all particle parameters and their influence on insulation performance are entirely understood [31]. Therefore, this work is a multi-scale approach towards increased understanding of precipitated silica and its use as a vacuum insulation media.

(a) *Internal construction of a VIP cooling box wall.*   **(b)** *Completed construction of cooling box.*

Figure 1.2: *Vacuum Insulation Panel (VIP) in a transportation cooling box.*

While the methodology presented here focuses on thermal engineering solely through VIPs, other applications can benefit from the proposed methodology. An emerging application of VIPs further reduces power consumption by combining thermal energy storage using Phase Change Materials (PCMs) [55]. More directly, integration via PCM micro-encapsulation, by Zhang et al. [86], as well as nano-particle PCM impregnation, by Singh et al. [73], are investigated. Numerical evaluation of thermal conductivity through such nano-structures, using the methods presented in this work, will allow for directed optimization of production parameters for improved energy storage and thermal performance.

Moreover, the application of the proposed methodology to other areas of thermal engineering are prevalent. The most readily evident is the application to silica aerogels, an

example of which is the extension of models using elementary geometrical structures for silica aerogels thermal conductivity estimation by Dai et al. [18], similar to the work of Fang et al. [24]. Furthermore, with the advent of Nanoelectromechanical Systems (NEMS), applications for the estimation of thermal conductivity through these nano-structures are of significant interest as shown by Kim et al. [44]. Moreover, with the inclusion of slip boundary conditions in Lattice Boltzmann Methods (LBMs) such as those by Augusto et al. [3] or Li et al. for conjugate heat and mass transfer [51], the proposed methodology may also be applied to numerical evaluations of thermal behaviors in nano-catalyts at various pressures, similar to Cao et al. [14].

1.3.1 Advantages

Several significant advantages are provided by VIPs over traditional insulation materials. These advantages are highlighted in the following list:

- VIPs have an insulation performance which ranges from $0.004\,\mathrm{W/(m\,K)}$ in pristine condition to typical $0.008\,\mathrm{W/(m\,K)}$ after 25 years of ageing [40].

- When damaged, the panel using fumed silica still has a thermal conductivity of $0.02\,\mathrm{W/(m\,K)}$ [40].

- Use of VIPs can increase commercial or residential usable space as well as transportation volume.

1.3.2 Disadvantages

The corresponding disadvantages which limit the widely accepted use of VIPs [40], are similarly listed:

- VIP core materials are expensive.

- Life span is limited (projected to be 25 years), and is difficult to quantify/measure.

- Often damaged during production/transport/installation.

- Construction using VIPs require additional planning during construction the panels are not flexible nor can they be cut on site.

- Density is greater than $150 \, \mathrm{kg/m^3}$ which is heavier than other insulation materials.

- Sealing envelope is made from Aluminum allowing thermal bridging.

1.3.3 Possible Improvements of VIPs

The following improvements to the VIPs can be considered, in order to increase adoption of the panels:

- Improvements to the panel envelope can allow for cheaper cores (glass fiber and polyurethane foams).

  - reduce permeability

  - reduce thermal bridging

  - improve sealing technique

- Improve the core material.

  - reduce solid and radiative conductivity

  - find a core that rejects permeating gases and maintains a vacuum on its own

  - find a core material which minimizes ETC at atmospheric pressure

- Improve production and installation procedures to reduce incidents of damage.

- Return on Investment (ROI) improved when including space savings and acoustic absorption

1.4 Literature Review

An in depth review of VIPs in building construction, with economic, acoustic and thermal analysis, is provided by Baetens et al. [4] and Kalnæs et al. [40], which includes a summary of VIP products on the market. As well, an overview of materials and production of VIP media is presented by Berge et al. [7]. Bouquerel et al. [10] discuss analytical methods for modeling the ETC of different VIP constructions. An approach often used to model nano-silica geometries involves the use of fractals

or repetitions, of base/elementary geometries. For example, Enguehard et al. [22] generate elementary geometry units based on transmission electron microscopy (TEM) images of nano-porous silica. Similarly, Jae-Sung Kwon [46] and Kim et al. [43] use idealized geometry to model VIPs, and therefore simulate solid and gaseous thermal conductivity as well as radiation. Also, using elementary structures, Rochais et al. [67] present a method for procedural (fractal) generation of VIP nano-structure geometry, based on information from the fractal dimension. The generated geometry is used to simulate diffusion and conduction. Coquard et al. [16] also simulate heat transfer in VIPs, including the effects of moisture, using geometry based on elementary cubes modeled with a global porosity and contact surface area. Kan et al. [41] present a simple but effective model to predict the ETC of VIPs. However, the limitations of these aforementioned methods are: a sparse focus on structural parameters (macro porosity or primary particle size), exclusion of micro and nano-pores and generation of homogeneous geometries where the elementary structures at the nano-scale are the same at larger scales.

As an alternative to geometry generated with elementary structures, procedural methods have been presented here. For example, Lallich et al. [47] studied radiative heat transfer through single silica aggregates which vary in specific surface area, primary particle diameter and composition. The cluster geometry is generated using a diffusion limited cluster-cluster aggregation algorithm to achieve a close approximation of the fractal dimension. However, the study was limited to evaluation of only radiative heat transfer through single aggregates. In a followup work, Coquard et al. [17] use a particle cluster procedure to improve the geometrical modeling of the silica particles. The disadvantage of these methods is a lack of control over the internal pore size of the aggregates. Moreover, the pre-factor used in the generation algorithm is difficult to define precisely and causes large changes in the aggregate form [11, 76].

In contrast to modeling the particles themselves, Wang et al. [82] simulate the formation of pores, based on core distribution probability, growth directionality, porosity and phase interaction growth probability. Similarly, Qu et al. [63] stochastically generated porous geometry. In both cases, the LBM is used to simulate heat transfer due to gas and solid heat conduction; heat radiation was assumed to be negligible. However, radiation is considered to be a major component of the thermal conductivity and at low vacuum pressures, contributes around 40% of the heat flux [39].

A review of fluid-solid interactions was written by Cao et al. [13] where the dependence of slip on various physical factors is discussed. These factors include: liquid

polarity, viscosity, temperature, pressure, surface wettability, surface roughness, shear rate, and the presence of nanobubbles or gas films.

Guo et al. [34] propose two boundary conditions for microscale gas flows in LBM, those being discrete Maxwellian boundary condition (DMBC) and combination boundary condition (CBC). The CBC method was shown to be valid over a larger range of Knudsen number. CBC is a method which combines bounceback with specular reflection based on a factor r in (1.1), where Kn is the Knudsen number and A_1 and A_2 "are two parameters relating to the gas-wall interactions". For Poiseuille Flow and Kn=0.1 the results of CBC are in good agreement with numerical predictions. An analysis of the switching condition based on a local Knudsen number is provided by Lockerby et al. [52].

$$r = \left\{ 1 + \sqrt{\frac{\pi}{6}} \left[\frac{\Delta^2}{4Kn} + A_1 + \left(2A_2 - \frac{8}{\pi} \right) Kn \right] \right\}^{-1} \tag{1.1}$$

1.5 Overview and Aims

The following items outline the contribution of this work. First several topics are listed which have not been addressed by the current state of the art. Following, the scope of this work is outlined proceeded by topics which lie outside the scope of this work. Lastly the aims of the following chapters of this work are outlined.

Missing from Current Research

- The ability to monitor inline product characteristics for their evaluation related to the aggregate's form and diameter.

- Multivariate control over particle parameters (primary particle size, primary pore size, aggregate diameter, shape and standard deviation, overall packing porosity) to generate fully resolved and periodic particle geometries.

- Numerical simulation of effective thermal conductivity at the local pore-scale through fully resolved silica nano-particle geometries.

Scope of Work

- Measurement of particle size for silica particles within a range between 300 nm and 1000 nm using angle dependent light scattering.

- Numerical simulation of light scattering from arbitrary convex forms smaller than 100 nm.

- Numerical generation of silica aggregate geometries where primary particles are spherical.

- Control over the process of generating silica aggregate geometries by controlling variable primary particle size, primary pore size, aggregate diameter, aggregate shape and standard deviation, as well as overall packing porosity.

- Periodicity of silica packing in all axis directions (X, Y, Z, XY, XZ, YZ and XYZ).

- Numerical simulation of ETC due to radiation as well as conduction through solid and fluid components.

- Comparison of ETC to measurements and literature values in physical units.

Limitations

- Assumes that the VIP media evaluated is completely dry and does not retain water vapour.

- Assumes that convective heat transfer through the media is negligible, as the pore size is smaller than 3 mm [33].

- Averaged emission/absorption coefficients are used on the basis of a representative elementary volume (REV) [42] to simulate radiation through silica geometries.

Aims

- Develop a methodology to measure the dimensions of the sub-micrometer silica aggregates in order to obtain estimated diameter and shape information.

- Develop a procedural methodology for generating the sub-micrometer particle geometry in order to obtain a representative periodic packing of silica aggregates.

- Develop a methodology to numerically simulate ETC through a geometry of silica aggregates.

- Numerically evaluate the ETC through silica VIPs media and validate the results against measurement and literature values.

1.6 Solution Strategy

To maximize the minimum required pressure inside the VIP, the geometry of the packing medium can be modified. In order to understand effects of different packing geometry such as porosity and aggregate size on the individual contributions that make up the heat transfer through the VIP, a high fidelity model of the packing geometry is required. Increasing the internal pressure of the VIP while maintaining a

low effective thermal conductivity, can not only extend the lifetime of the panel, but would also decrease the unwanted thermal conductivity rise of a damaged panel as well as its cost of production.

To produce a high fidelity model of the silica media's geometry, measurements of primary particle size, primary pore size, aggregate diameter, shape and standard deviation, as well as overall packing porosity are made. Furthermore, a measurement and numerical simulation system is developed based on Static Light Scattering (SLS) and Montecarlo Light Scattering (MLS), to further understand the aggregate form. Thereafter, a procedural workflow to generate mesoscopic geometries of precipitated silica is developed. Finally, the heat transfer through these nano-porous geometries will be simulated using LBMs, including heat transfer due to radiation as well as conduction through solid and fluid components. The advantage of LBM, on the one hand, is that by using simple grids in combination with an efficient parallel algorithm, allows for resolving complex geometries with greater ease than with comparable methods. The other advantage is that no special interface consideration is needed in LBM to assure temperature and heat flux continuities at the solid-fluid interfaces.

1.7 Alternative Applications

While the methodology presented here focuses on heat transfer engineering through VIPs, other applications can benefit from the proposed methodology. An emerging application of VIPs further reduces power consumption by combining thermal energy storage using PCMs [55]. More directly, integration via PCM micro-encapsulation, by Zhang et al. [86], as well as nanoparticle PCM impregnation, by Singh et al. [73], are investigated. Numerical evaluation of thermal conductivity through such nano-structures, using the methods presented in this work, that allow for directed tuning of production parameters for improved energy storage and thermal performance, are already a prerequisite of such applications, and is proposed by Gaedtke et al. [29].

Moreover, the application of the proposed methodology to other areas of thermal engineering are prevalent. The most readily evident is the application to silica aerogels, for example, the extension of models using elementary geometrical structures for silica aerogels thermal conductivity estimation by Dai et al. [18], similar to the work of Fang et al. [24]. Furthermore, with the advent of NEMS, applications for the estimation of thermal conductivity through these nano-structures are of significant interest, as shown by Kim et al. [44]. Additionally, with the inclusion of slip boundary conditions in LBMs, such as those by Augusto et al. [3] or Li et al. for conjugate heat and mass

transfer [51], the proposed methodology may also be applied to enhance numerical evaluations of thermal behaviors in nano-catalyts at various pressures, similar to Cao et al. [14].

1.8 Chapter Overview

The proceeding chapters of this work are structured as follows with silica measurement and characterization methods that are described in Chapter 2. Followed in Chapter 3 by the methodology to generate silica geometry procedurally and calculate local pore distances. Heat transfer through nano-porous materials is described in Chapter 4 alongside a description of tools implemented for the development of slip boundary conditions. The ETC results through the modeled silica media are presented in Chapter 5 together with comparisons to literature and measurement values. Lastly, conclusions are presented in Chapter 6.

2

Silica Measurements and Light Scattering Simulations

Suppose you want to measure the size of something, then you need to figure out where the ends of this moving object are. You can never do this accurately, because it will involve making a measurement of both the positions of something and its speed at the same time.

Stephen Hawking

2.1 Aims and Overview

The goal of this chapter is to develop a methodology for measurement of sub-micrometer particles in order to obtain diameter and shape information. The methodology is designed to augment measurement results obtained from Small Angle X-Ray Scattering (SAXS), Mercury Intrusion Porosimetry (MIP) and Analytical Ultracentrifugation (AUC). With the additional information of the diameter and shape of the silica aggregates more precise models for geometry generation will be developed.

This chapter is organized as follows. The motivation is presented in Section 2.2. Thereafter included in the methods is a description of the Static Light Scattering (SLS) experimental apparatus is provided in Section 2.3.1, followed by the data evaluation algorithm for the SLS measurements in Section 2.3.2. The generation of the Mie light scattering database is described in Section 2.3.3 and a description of how to obtain shape information from the SLS measurements in Section 2.3.4. To complete the methods for this chapter, an overview of the Montecarlo Light Scattering (MLS) algorithm is provided in Section 2.3.5. The results are thereafter presented, with the characterization of diameter results from the SLS provided in Section 2.4.1 and shape results in Section 2.4.2. Thereafter, the Montecarlo Light Scattering (MLS) results for spherical and elliptical particle forms are presented in Section 2.4.3 and Section 2.4.4 respectively. Lastly, a discussion and outlook are presented in Section 2.5 and conclusion in Section 2.6.

The SLS measurement apparatus, measurements and subsequent data analysis were developed and conducted in collaboration with Tobias Teumer, Susann Wunsch and Lukas Petri. The Mie database generation and SLS measurement automation were performed solely by Jesse Ross-Jones. These methods and results have also been published in a *Feasibility Study for a Chemical Process Particle Size Characterization System for Explosive Environments using Low Laser Power* [69]. The particle measurements described in this chapter were performed by Manuel Meier. The MLS simulations were developed in collaboration with Fernando Garcia, with the visualizations generated solely by Jesse Ross-Jones.

2.2 Motivation

Different measurement methodologies are used to infer a near complete picture of the nano-structure of precipitated silica. Three precipitated silica samples were measured (GT, KS and CP from Grace Silica GmbH) and three analytical measurement (MIP, SAXS and AUC) methods are used to obtain information at different measurement scales and for different packing properties.

MIP measurements, where mercury at increasing pressures is forced into a sample, provide insight into the volumetric pore size distribution and porosity of each sample. To obtain insight into the size of the primary particles and of the size and shape of the silica aggregates, SAXS measurements are conducted [56], which measure the scattering angles of X-Rays transmitted through a sample. Lastly, an AUC, which

optically measures sedimentation times, was used to obtain insights into the aggregate diameter and its variation.

The MIP, SAXS and AUC measurements are presented in Table 2.1 and provide a multi-scale description of the precipitated silica samples. The geometry generation methodology, built around these measurements, is described in Chapter 3. While these measurements provide important insights into the geometry parameters of the precipitated silica, significant information is still missing, such as sub-micrometer aggregate form, obtaining of which is the goal of the following sections.

Table 2.1: *Silica particle measurements, from left to right: primary pore size and porosity measurements obtained from Mercury Intrusion Porosimetry (MIP) measurements; primary particle size, surface fractal dimension and mass fractal dimension obtained from Small Angle X-Ray Scattering (SAXS) measurements and average aggregate diameter and standard deviation obtained from Analytical Ultracentrifugation (AUC) measurements [56].*

	Mercury Porosimetry		Small Angle X-Ray Scattering			Analytical Ultracentrifugation	
Sample	d_{pore} [nm]	Π [%]	d_p [nm]	D_{sf} [-]	D_{mf} [-]	d_{agg} [nm]	σ_{agg} [%]
GT	28.3	89.7	20.8	2.05	1.95	120.35	13.51
KS	25.2	86.6	19.8	1.88	2.07	116.20	13.44
CP	9.1	87.4	11.9	1.93	1.85	107.25	22.27

2.3 Methods

The following section presents the methodologies used to obtain the SLS measurements of particle diameter and shape, as well as the MLS simulations of light scattering from different particle forms.

2.3.1 Static Light Scattering Experimental Setup

To measure the light scattered from silica particles, a laboratory apparatus was constructed. Instead of measuring over different wavelengths a single wavelength is used for measuring side scattering over a range of angles.

The apparatus is demonstrated in Figure 2.1. With this setup, scattered light is measured at angles within a range between 20° and 160° around the cuvette. The axis of rotation is coaxial with the cuvette center. The cuvette is constrained to only move vertically, co-axially with the axis of rotation. For certain measurements, the cuvette may also be rotated slightly. For the majority of the measurements described, the rotation is fixed at 90°, further description being available in Section 2.3.4. The source laser impinges on the center of the glass cuvette perpendicular to the flow direction.

A fiber optic cable is placed in a holder which feeds the received light into a Customized Photon Counting Module (CPM). The CPM CM 93YE and CM 93LB from ProxiVision GmbH boasts a maximum of 10 megacounts per second and typical dark counts of between 3 and 10 counts per second respectively [2].

A dispersion of silica particles is prepared with a concentration of 0.015 mg/mL. The cuvette has an inner diameter of 1 cm through which the dispersion is pumped, using a peristaltic pump. A stepper motor controlled by an Arduino Uno, with a 3 pin momentary rocker switch to control movement direction, moves the fiber optic receiver through the measurement angles. The use of automation allows for reproducable fine angle adjustments and high resolution measurements. The repository for the Arduino code is described in the Appendix Section D.

In order to reduce background light (noise), the apparatus is placed in a light limiting enclosure, and the entire experiment is conducted in a dark room. Moreover, the Arduino Uno and thus the Light Emitting Diode (LED) indicators are kept covered and outside the enclosure. The gearing and adapters for the setup were printed on an Ultimaker 2+ in white Polylactic Acid (PLA). In order to assure tightly fitting parts, a tolerance of 0.1 mm is used.

2.3.2 Data Evaluation Algorithm

The following workflow describes the curve matching algorithm used to select the closest matching signal from the Mie simulation database, presented in Figure 2.2. The presented algorithm finds matches based on the signal's shape despite intensity differences of several magnitudes. The method implements curve shape matching following a similar method as Buchin et al. [12], where the curve is divided into intervals and positive and negative slopes are compared.
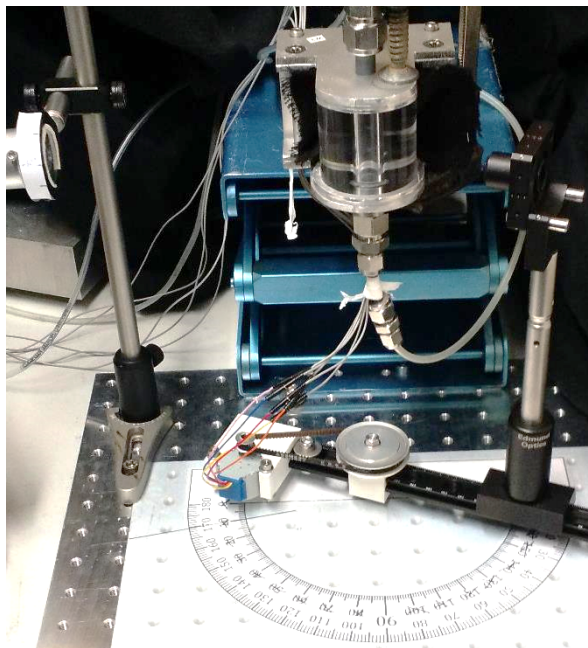
Figure 2.1: *Implemented SLS measurement apparatus demonstrating laser light source, fiber optic receiver, cuvette, rotational center*

The inputs to the system are: the path to the simulation database, as well as the measurement parameters (step size, starting angle, ending angle, and layer number). The measurement data is parsed from the Technical Data Management System (TDMS) data file provided by the measurement equipment. Following, the measurement signal is approximated using a combination of sinusoidal functions (selected using Mean Squared Error (MSE)), providing both a smoothing of the signal and allows for the derivative to be calculated in a following step. The function is then normalized and the first derivative is evaluated.

In order to reduce the number of possible solutions a filter is introduced, allowing for the number of extema to be evaluated. If the number of extrema in the measurement is less than or equal to four, the database is filtered for signals with the same number ± one of extrema. This is the case for particles with a diameter less than approximately 700 nm. If on the other hand, the measurement signal has more than four extrema (which is the case for larger diameter particles in the range of 700 nm to 1000 nm) the database is simply filtered to find signals which have the same or more number of extrema. The reason for filtering for larger number of extrema is to exclude the possibility of aliasing, where possible extrema are overlooked during measurement.

This filter may also be skipped by the user to instead compare against all available curves in the Mie database.

The next step iterates over each signal (i) in the measurement database (or filtered database). For each angle (a), counts of the number of occasions where the signs of $\dot{I}_M(a)$ and $\dot{I}_{Q,i}(a)$ are the same and opposite respectively are maintained (in variables C_{ss} and C_{os}, following (2.1), respectively). Furthermore, for each signal, an array of the areas (Ap_i and An_i) for each measurement angle between $\dot{I}_M(a)$ and $\dot{I}_{Q,i}(a)$ are evaluated in (2.2). Ap is evaluated as one over the area (Ap increases as the curves get closer together) when the two curves have the same sign (positive), and An evaluated as the area when the two curves have opposite sign (negative). Following, leaving the loop, the two area arrays Ap_i and An_i are normalized (to Ap'_i and An'_i respectively) and the relative occurrence of positive and negative intervals, f_{ss} and f_{os}, given by (2.3), are calculated. The closest matching curve is then the maximum as derived in (2.4).

$$
\begin{aligned}
C_{ss} &= \sum_{min(\alpha)}^{max(\alpha)} \left(sgn(\dot{I}_M(\alpha)) = sgn(\dot{I}_Q(\alpha)) \right) \\
C_{os} &= \sum_{min(\alpha)}^{max(\alpha)} \left(sgn(\dot{I}_M(\alpha)) \neq sgn(\dot{I}_Q(\alpha)) \right)
\end{aligned}
\tag{2.1}
$$

$$
\begin{aligned}
Ap_i &= \int_{a_l}^{a_u} \frac{1}{\left| \dot{I}_M(a) - \dot{I}_{Q,i}(a) \right|} \to sgn\left(\dot{I}_M(a)\right) = sgn\left(\dot{I}_{Q,i}(a)\right) \\
An_i &= \int_{a_l}^{a_u} \left| \dot{I}_M(a) - \dot{I}_{Q,i}(a) \right| \to sgn\left(\dot{I}_M(a)\right) \neq sgn\left(\dot{I}_{Q,i}(a)\right)
\end{aligned}
\tag{2.2}
$$

$$
f_{ss} = \frac{C_{ss}}{C_{ss} + C_{os}} \quad \text{and} \quad f_{os} = \frac{C_{os}}{C_{ss} + C_{os}}
\tag{2.3}
$$

$$
fit = max \left(\frac{Ap'_i \cdot f_{ss}}{An'_i \cdot f_{os}} \right)
\tag{2.4}
$$

In the case where multiple curves display congruence with the measurement, other local maxima are present in the fit vector.
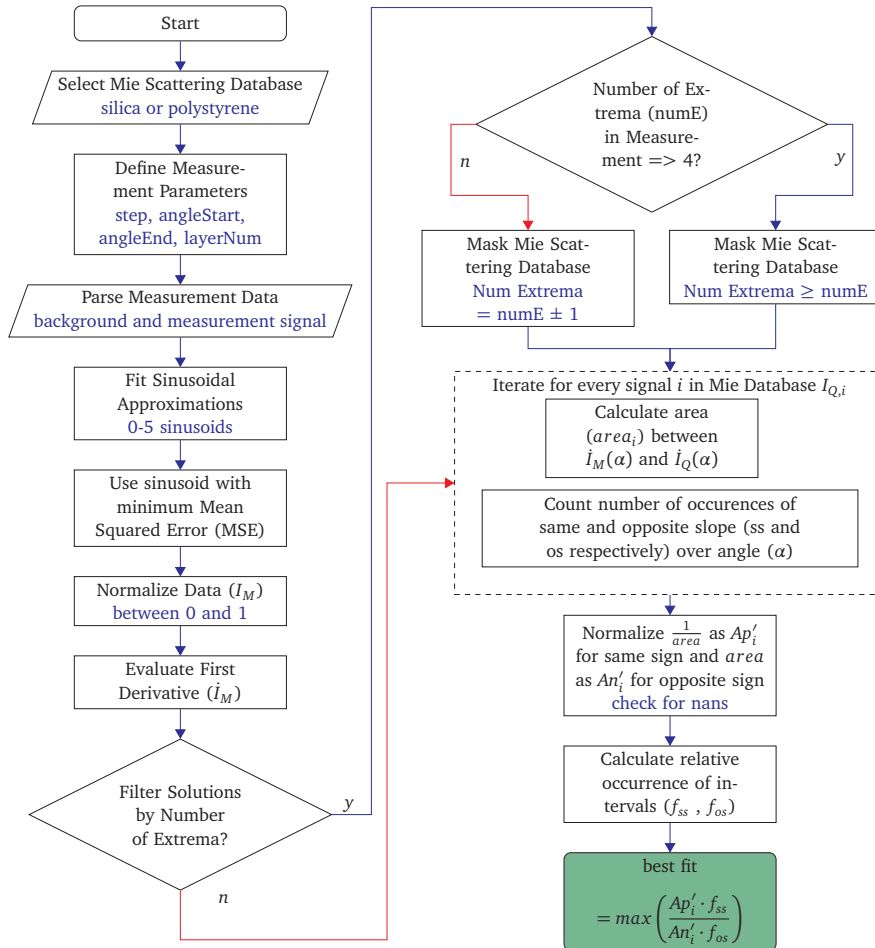

Figure 2.2: *Algorithmic flowchart for evaluating particle diameter from Static Light Scattering (SLS) measurement data*

2.3.3 Mie Light Scattering Database

The light scattering database used to evaluate particle size as described in Section 2.3.2 is generated using MiePlot software by Phillip Laven [59], with sample profiles, from 200 nm to 2000 nm, shown in Figure 2.3. The refractive index is wavelength dependent and is defined as described in Table 2.2.
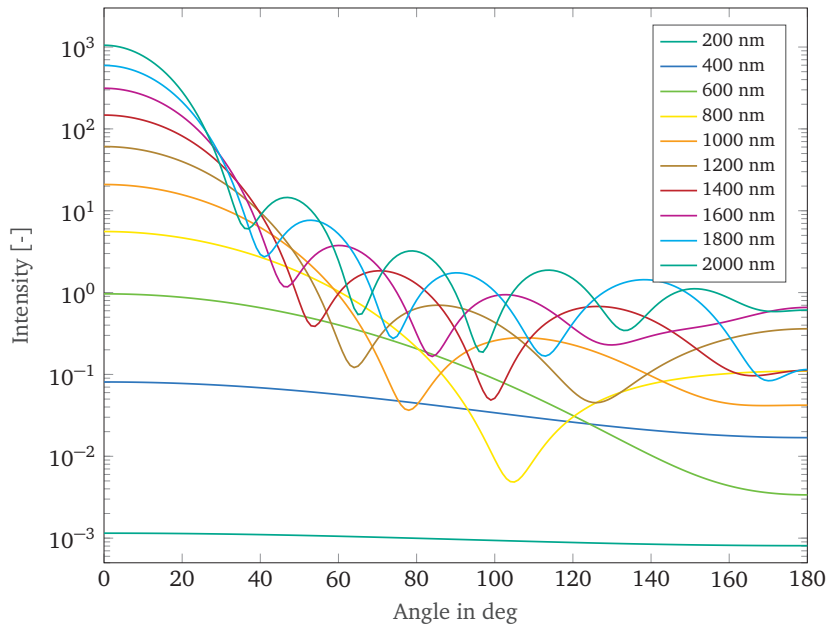
Figure 2.3: *Sample profiles of Mie side scattering from particles of diameter* 200 nm *to* 2000 nm*, generated with MiePlot by Phillip Laven.*

Table 2.2: *Wavelength dependent refractive index of silica [60].*

Wavelength [μm]	Refractive Index [-]
0.43584	1.4667
0.47998	1.4635
0.58756	1.4585
0.70652	1.4551

Calculations are performed for spheres with radii between 100 nm to 550 nm with a 5 nm step size. To facilitate the calculation, MiePlot enables the use of batch files. For this calculation the batch file shown in Source Code 2.1 is utilized, with the remaining parameter settings manually established in MiePlot before loading the batch file. These parameters are shown in Table 2.3. The calculations are saved to a single 'mut' file by MiePlot; the first 20 lines are shown in Source Code 2.2.

```
1 MiePlot 4100 batch file
2 step
3 radius
4 0.1 0.55 0.005
5 run
```

Source Code 2.1: *Batch File for MiePlot*

Table 2.3: *Parameters used in MiePlot light scattering calculations.*

Parameter	Value
Calculation	Intensity v. Scattering Angle
Wavelength	650 nm
Sphere	Silica
Medium	Water (Segelstein)
Minimum Angle	0°
Maximum Angle	180°
Polarization	Both
Dispersion	Monodisperse
Light Source	Point

```
 1 MiePlot v4.1
 2
 3 Date & Time: 06-Mar-19 12:43:07 PM
 4 Calculation Method:        Mie (plane wave)
 5
 6 Sphere:          silica
 7 Medium:          Water
 8 Refractive index (sphere)     Real part:      1.456704
            Imaginary part:       0
 9 Refractive index (medium)     1.330687
10 Wavelength:      0.65     um
11 Radius:           0.1     um     Size parameter x:
      1.2863
12 Graph type:     Intensity v. scattering angle
13
14 Angle    Perpendicular     Parallel        Unpolarised
15 theta    (S1(theta))^2   (S2(theta))^2   (S1(theta))^2 + (S2(
      theta))^2
16 0        1.89802770873478E-02    1.89802770873478E-02
      1.89802770873478E-02
17 0.1     1.89802576676967E-02    1.89802015475017E-02
      1.89802296075992E-02
18 0.2     1.89801994089039E-02    1.89799749294722E-02
      1.89800871691881E-02
```

```
19   0.3       1.89801023114511E-02      1.89795972377848E-02
         0.018979849774618
20   0.4       1.89799663761411E-02      0.018979068479982
         1.89795174280616E-02
```

Source Code 2.2: *MiePlot Caclulation Output*

2.3.4 Obtaining Shape Information from SLS

During the design of the SLS apparatus, additional considerations were taken into acccount to allow for pitch rotations of the cuvette, so as to include the option of making off axis measurements. The on and off axis measurements can be combined to form an estimate by extrapolation of the particles shape. Measurements are made for a total of four angles (β) [$-30°$, $-15°$, $0°$ and $15°$]. Each separate measurement is processed with the workflow described in Section 2.3.2, which produce a diameter estimate. To visualise the various estimates, each diameter is displayed along its measurement axis, which is accomplished by using the rotation matrix (2.5)

$$R = \begin{bmatrix} 1 & 0 & 0 \\ 0 & cos(\beta) & -sin(\beta) \\ 0 & sin(\beta) & cos(\beta) \end{bmatrix}. \tag{2.5}$$

An example of the visualized measurement diameters is presented in Figure 2.5. The particle is assumed to be an ellipsoid. With the radii r_x and r_y (as shown in Figure 2.4) both being defined by the $0°$ measurement and by continuing the same assumption, $r_x = r_y$ (defined by a circle). For the remaining, off axis, measurements, the measured forms are no longer circular and instead are elliptical. The radius r_x or 'width' is assumed to be the same as r_x at $0°$. The radius r_y is larger and is defined such that the average of r_y and r_x results in the measured radius. Once the r_y for all three off axis measurements are calculated, an elliptical function is fit to the four data points with the minimum MSE. This function can be used to predict the height, sphericity (Ψ) given by (2.6) and aspect ratio (ρ) given by (2.7). Where V_p and A_p are the estimated volume and surface area of the ellipsoid respectively.

$$\Psi = \frac{\pi^{1/3}(6V_p)^{2/3}}{A_p} \tag{2.6}$$

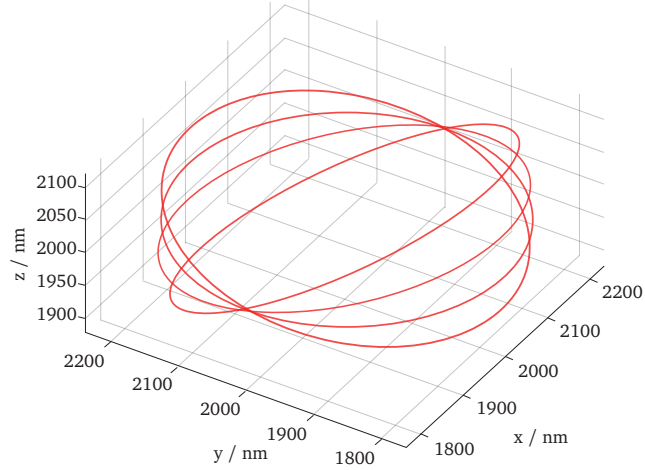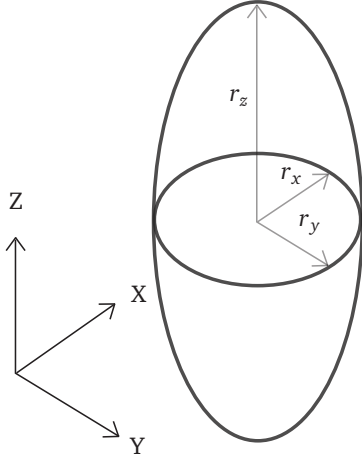$$\rho = \frac{d_z}{d_x} = \frac{d_z}{d_y} \tag{2.7}$$

Figure 2.4: *Ellipsoid radii definition*

Figure 2.5: *Shape estimation using multi-angle SLS*

2.3.5 Montecarlo Light Scattering Algorithm Overview

The workflow in Figure 2.6 outlines the procedure used to simulate constructive and destructive interference from scattered light. The light rays are considered plane waves with the incident intensity defined in (2.8), where I is the light intensity at a given distance d and time t, with extinction (attenuation) coefficient μ, wavelength λ, the phase shift is $k \cdot d$ and the frequency w and are defined in (2.9). A distinction is required for rays traveling out and inside the particle, where the refractive index alters the speed of light $c = 299\,792\,458 \times 10^9$ nm/s.

$$I(d,t) = e^{-2\pi \mu d / \lambda} cos(kd - wt) \tag{2.8}$$

$$k = \frac{2\pi n}{\lambda} \quad \text{and} \quad w = \frac{2\pi c}{\lambda} \tag{2.9}$$

The simulation environment is composed of two polygons: a particle of interest, and a sensor object. The sensor object is required to collect the scattered rays, where the faces of the polygon act as individual detectors. To minimize projection distortions and maintain approximately equal size/shaped faces, the sensor object is a quadri-lateralized spherical cube [15]. The environment is simulated within the software

Blender [9], and is built around ray_cast in blender python's $bpy.types.Object$. The ray_cast returns: result (boolean), location of intersection, face normal direction, and face index, whereby the face index is used to aggregate successfully scattered rays.
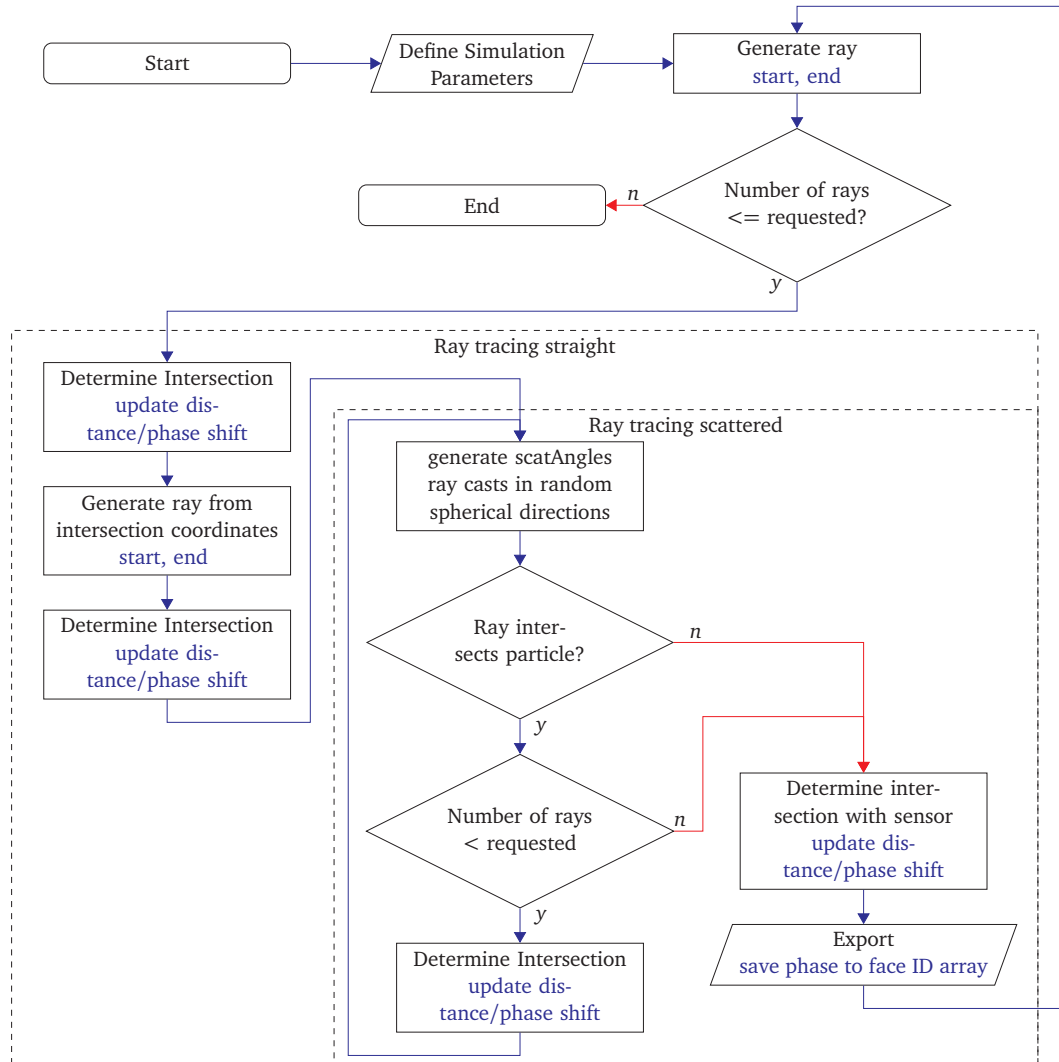

Figure 2.6: *Algorithmic flowchart for numerical evaluation of light scattered from nano-particles*

The algorithm initially generates parallel rays, which travel directly towards the particle. These 'straight' rays intersect with the particle and from these coordinates, a large number of scattered rays are generated. These rays must be slightly offset

in the direction of travel to avoid repeat intersection of the ray and particle. The scattering rays section of the algorithm is recursive, and continues to call itself until the requested number of internally scattered rays have been reached or a ray no longer intersects with the particle. Once either of these two conditions are reached, the ray will intersect with the sensor object and the recursion breaks. This workflow is presented in Figure 2.6, with the simulation parameters outlined in Table 2.4.

Table 2.4: *Parameters used in Montecarlo light scattering simulations.*

Parameter	Value
Calculation	Intensity v. Scattering Angle
Wavelength	650 nm
Sphere	Water
Medium	Vacuum
Minimum Angle	0°
Maximum Angle	359°
Polarization	Perpendicular
Dispersion	Monodisperse
Light Source	Point

2.4 Results

The following section presents the results from the SLS measurements of particle diameter and shape, as well as the MLS simulations of light scattering from different particle forms.

2.4.1 Static Light Scattering Diameter Evaluation

Silica particles of sizes 314 nm, 407 nm, 507 nm, 546 nm, 640 nm, 681 nm, 726 nm, 812 nm, 900 nm and 987 nm were measured. The results presented in Table 2.5 are an overview of the characterization analysis of the measured silica dispersions. While most of the measured silica particles are accurately characterized to within 5 %, some show deviations as high as 66 %, from the manufacturer provided particle size. As observed in Table 2.5, poor accuracy resulted when measuring particle sizes of 407 nm, 640 nm and 812 nm.

Additional details are provided by Figures 2.7–2.10, which display the characterization results for 407 nm, 640 nm, 681 nm and 812 nm particles. These example results demonstrate both well-classified as well as miss-classified particle diameters. Each of the figures contains four subplots. The top left is a representation of the measured signal together with the sinusoidal approximation. The top center subplot displays the most congruent simulation curve. The top right subplot displays the simulation curve of the known particle diameter. Lastly, the bottom subplot displays the fit vector which is the congruence of the measurement signal to each simulation in the database.
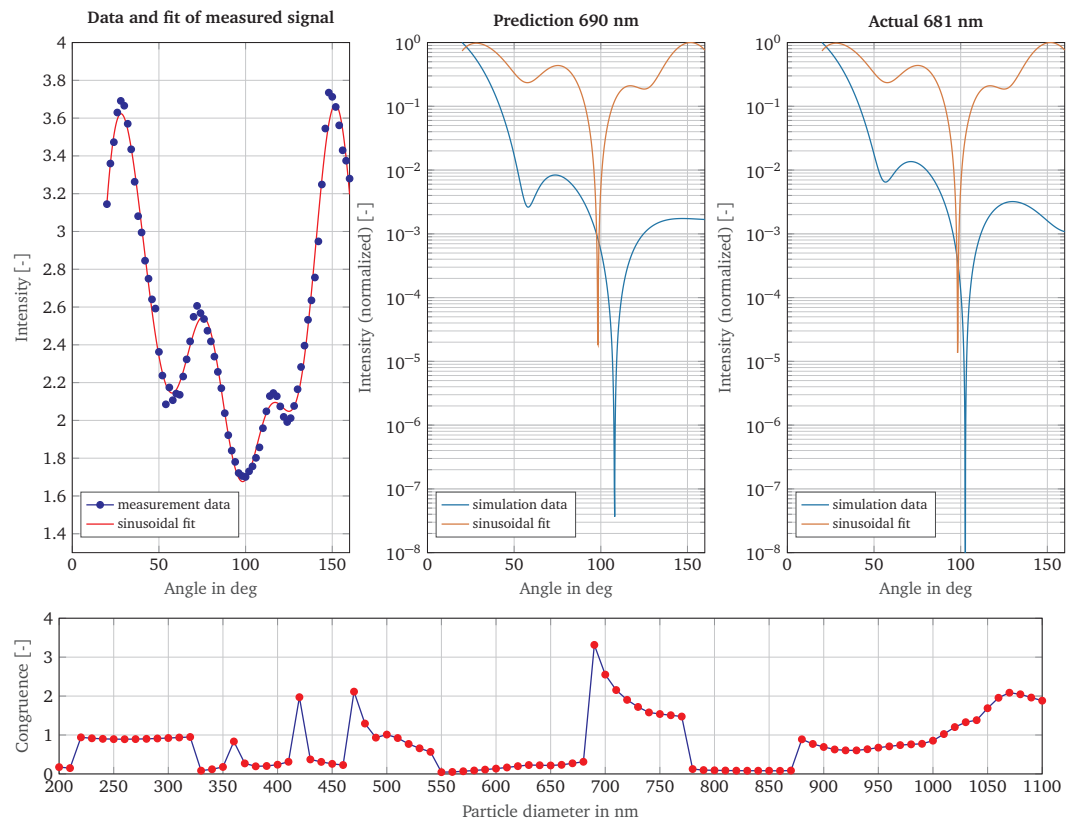

Figure 2.7: *Particle size characterization for* 681 nm *silica particles, filtering the possible simulation results by the number of local extrema. Light scatter measured in 5 degree increments from 20 to 160 degrees. Measurement and sinusoidal fit (top left), comparison to best fit result (top center) and comparison to actual particle size (top right), overall congruence to simulation database (bottom)*

The 681 nm silica particles were accurately characterized with a diameter of 690 nm, as shown in Figure 2.7. Similarly, the silica particles: 507 nm, 900 nm and 987 nm were quite accurately characterized (see Table 2.5). However, the 410 nm silica particles were characterized with a diameter of 710 nm, as shown in Figure 2.8. However, good agreement can be seen between the simulation data for 410 nm and the measurement data (Figure 2.8 top right). This disparity is likely due to the difference in slope occurring below 50° and above 140°. Furthermore, the curve for 710 nm contains an extra peak at 55° which excludes it as a possible candidate.
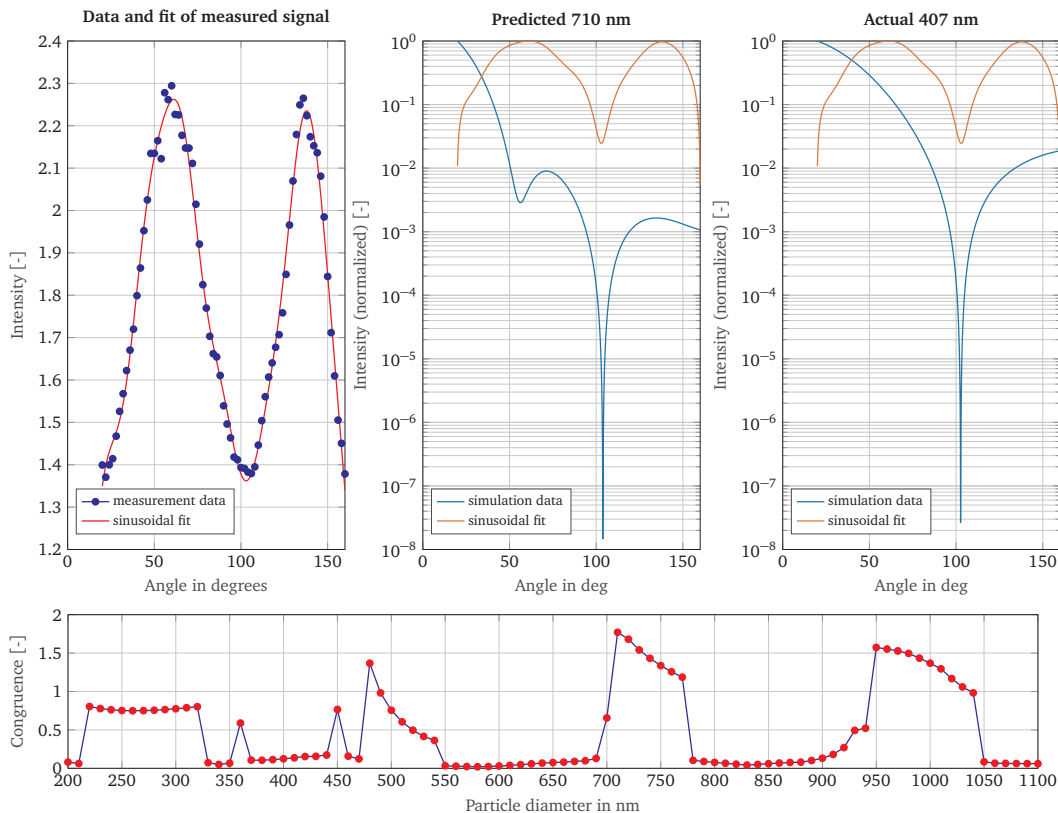

Figure 2.8: *Particle size characterization for* 407 nm *silica particles, filtering the possible simulation results by the number of local extrema. Light scatter measured in 5 degree increments from 20 to 160 degrees. Measurement and sinusoidal fit (top left), comparison to best fit result (top center) and comparison to actual particle size (top right), overall congruence to simulation database (bottom)*

A similar miss-characterization occurs with the 640 nm particles being labeled as 200 nm, as shown in Figure 2.9. In this case, the measurement curve contains a peak

at 65°, which is not reflected in the simulation. The simulation curve for 640 nm actually fits quite well to the measurement data when consideration is made for the two peaks shifting closer together (Figure 2.9 top right).
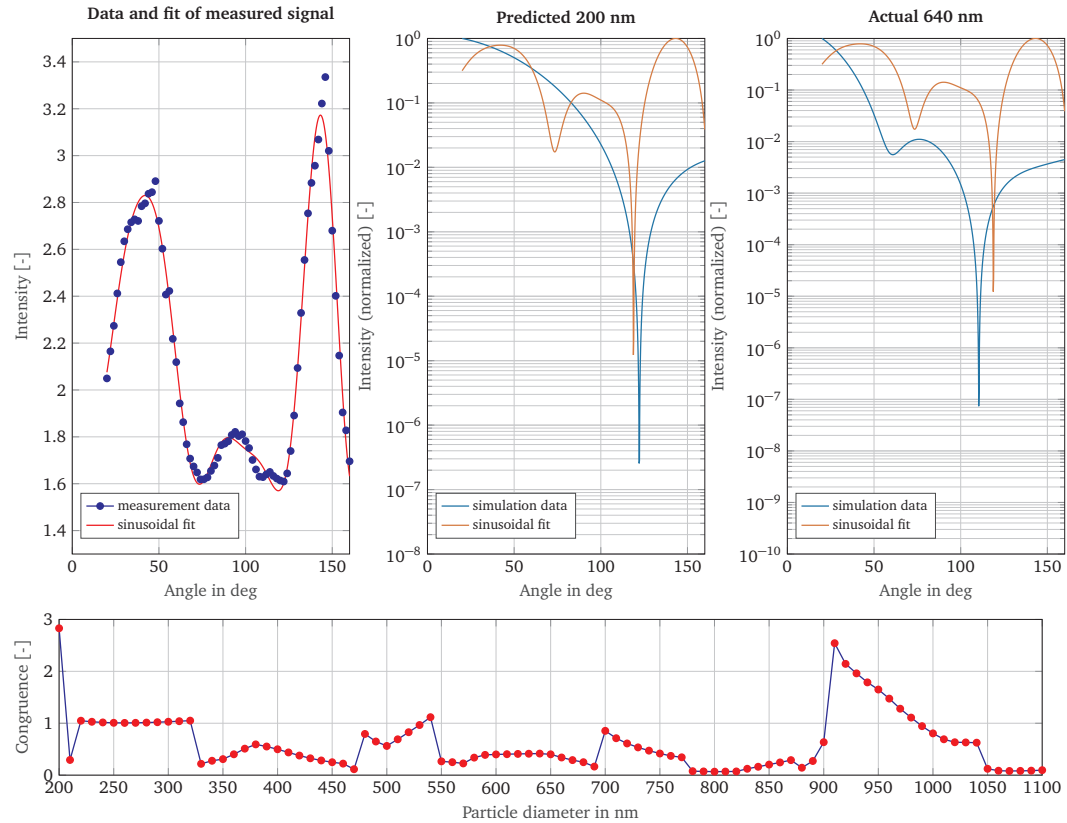

Figure 2.9: *Particle size characterization for 640 nm silica particles, filtering the possible simulation results by the number of local extrema. Light scatter measured in 5 degree increments from 20 to 160 degrees. Measurement and sinusoidal fit (top left), comparison to best fit result (top center) and comparison to actual particle size (top right), overall congruence to simulation database (bottom)*

The last example characterization of 812 nm, where the particles are labled as 690 nm is shown in Figure 2.10. In this case the measurement signal contains three peaks, the third of which is not present in the simulation of 690 nm. Once again the three peaks are present (but shifted) in the 812 nm simulation.

In particular, these results show the importance of using a high angular resolution when measuring light scattering over a broad range of angles, otherwise aliasing of peaks occurs and false deductions are made when interpreting the particle diameter,
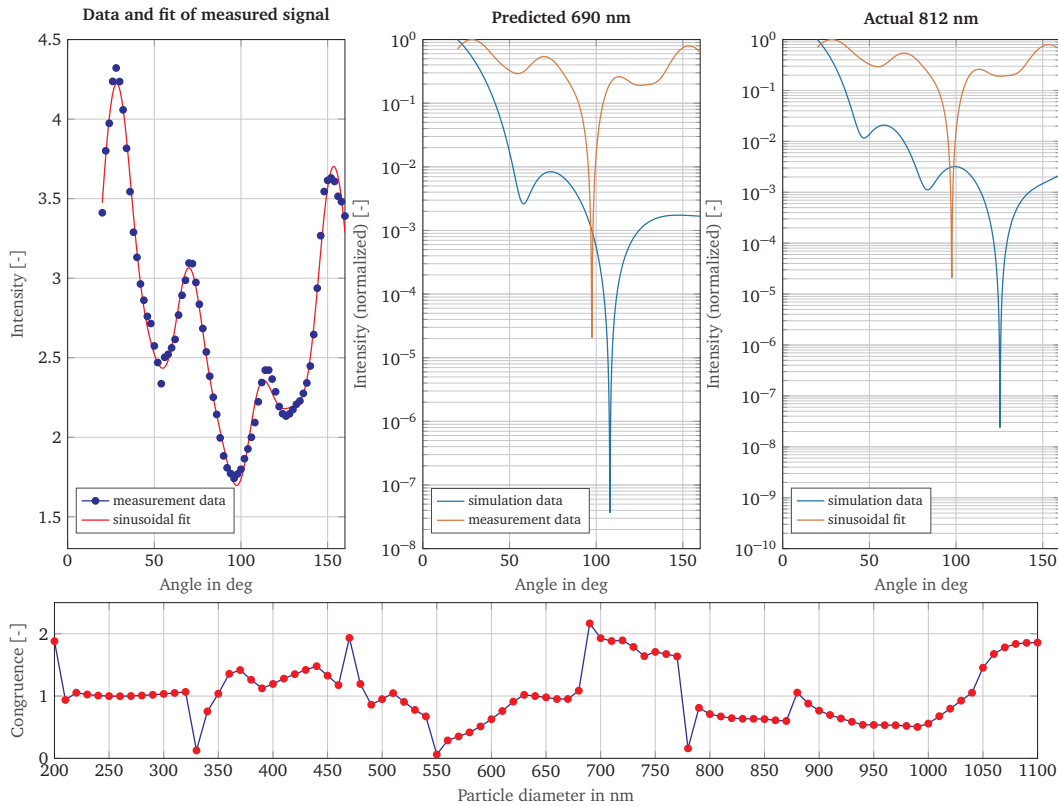
Figure 2.10: *Particle size characterization for 812 nm silica particles, filtering the possible simulation results by the number of local extrema. Light scatter measured in 5 degree increments from 20 to 160 degrees. Measurement and sinusoidal fit (top left), comparison to best fit result (top center) and comparison to actual particle size (top right), overall congruence to simulation database (bottom)*

as was the case with the measurement of 1000 nm polystyrene particles. Since 71 measurements between 20° and 160° with 2° angle increments were taken, the number of peaks resolved in the signal could be leveraged to filter out unlikely particle size candidates. While this work obtains the mean particle size, a second iteration is planned whereby the particle size distribution is estimated. The workflow entails first characterizing the mean particle size as described here, followed by a second characterization whereby the measured signal is compared to simulated Mie scattering signals with fixed mean particle size and increasing diameter distribution width. In this way, the mean particle size as well as particle distribution are procedurally characterized.

Table 2.5: *Overview of light scattering diameter estimation results using unpolarized as well as perpendicularly polarized light, with shaded cells highlighting good predictions of silica particle diameter.*

Particle Diameter	Diameter Prediction		Relative Error	
DataSheet	Unpolarized	Perpendicular Pol.	Unpolarized	Perpendicular Pol.
[nm]	[nm]	[nm]	%	%
314	330	1050	5.09	234.39
407	710	460	74.45	13.02
507	480	460	5.33	9.27
546	460	460	15.75	15.75
640	200	910	68.75	42.19
681	690	750	1.32	10.13
726	690	650	4.96	10.47
812	690	1090	15.02	34.24
900	880	940	2.22	4.44
987	960	950	2.73	3.75

2.4.2 Static Light Scattering Shape Evaluation

Using the methodology presented in Section 2.3.4, 500 nm particles were measured at the four angles −30°, −15°, 0° and 15° with the corresponding evaluated particle diameters: 480 nm, 480 nm, 470 nm and 470 nm. This experiment was conducted prior to the purchase of silica particles and was conducted on polystyrene particles with a refractive index of 1.59 (which was considered in the simulation parameters). The measurements are visualized in Figure 2.11, with each measurement at their corresponding angle and distance from the origin. Through minimization of the MSE, the particles longest dimension d_z is estimated: 585 nm.

2.4.3 Montecarlo Light Scattering Spherical Particles

MLS numerical simulations were conducted for spherical particles of radii: 10 nm, 50 nm, 100 nm, 150 nm and 200 nm, following the methodology described in Section 2.3.5. The results are displayed in Figure 2.12 [left] alongside results from Mie light scattering [right] (for perpendicularly polarized light). For these simulations, only a two dimensional slice of the simulation is presented, where the scattered rays arriving at the sensors on the X-Y plane are considered. The light scattered is symmetrical around the measurement axis (X-axis) in the case of these spherical
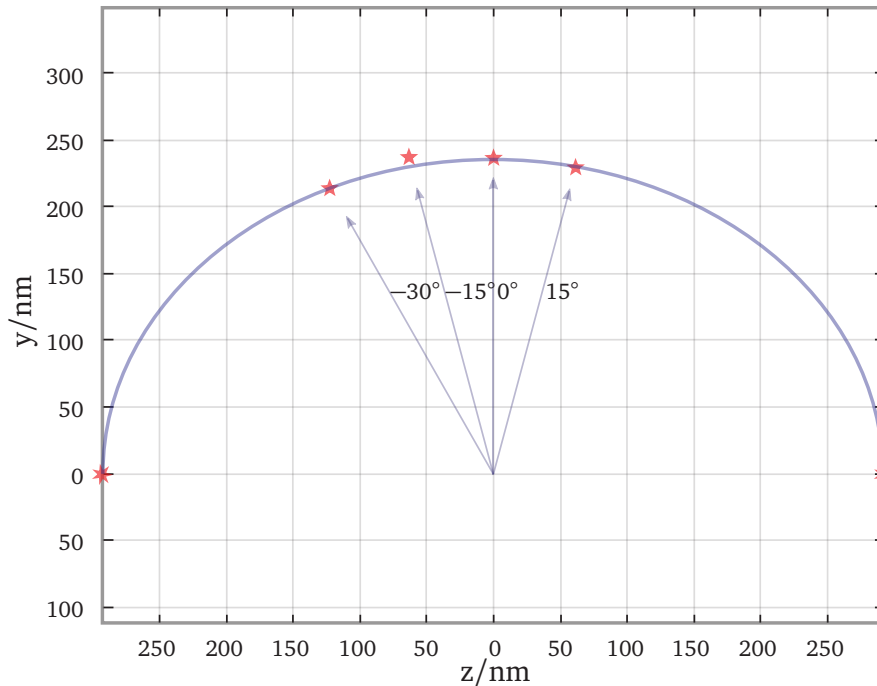
Figure 2.11: *Shape estimation using light scattered at multiple measurement angles, −30°, −15°, 0° and 15°*

particles. The three dimensional visualization of the MLS results for a 100 nm particle are presented in Figure 2.14.

Figure 2.12 shows the relative intensities of the forward and back scattered light for each particle considered. The results demonstrate particularly good agreement, with the relative intensity of back scattered light decreasing as the particle diameter increases in both the MLS and Mie simulations.

A particular difference is notable in the missing lobe in the back scattering for the 150 nm and 200 nm radius particles. However, when the parallelly polarized component of the Mie scattering is considered, this lobe is present (see Figure 2.13). Further work is recommended in this direction, to consider diffracted and refracted rays separately to capture these polarization effects.

The results comparing the light scattering from spherical particles are used as an initial validation of the method, before considering the light scattering from ellipsoidal particles in the following section.
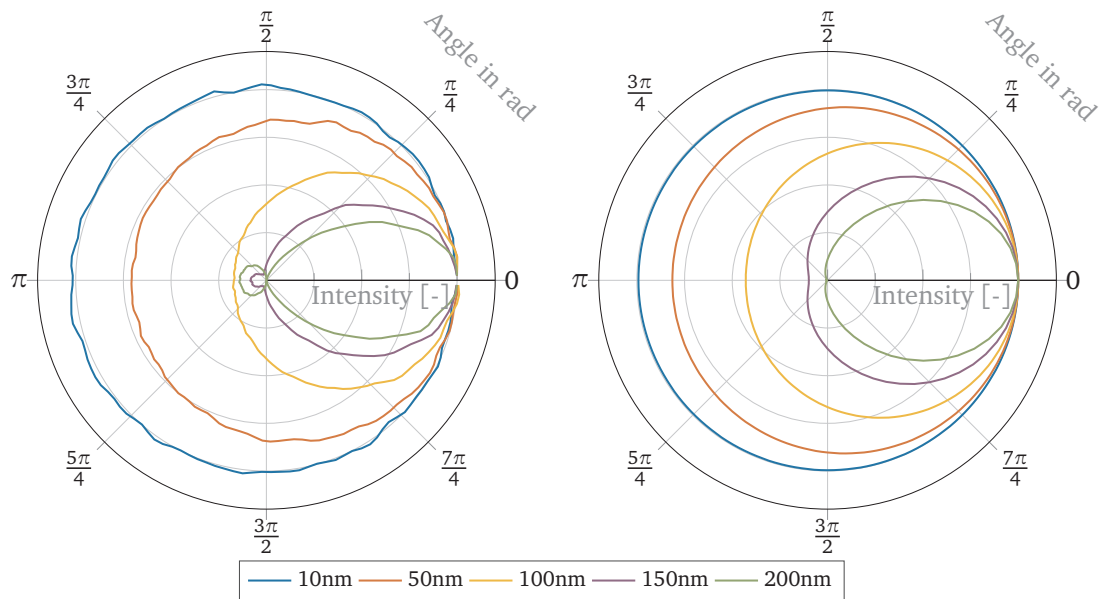
Figure 2.12: *Relative light intensity from 2D montecarlo light scattering [left] and Mie simulations [right] (perpendicularly polarized) of* 10 nm*,* 50 nm*,* 100 nm*,* 150 nm *and* 200 nm *radii spherical particles*

2.4.4 Montecarlo Light Scattering Ellipsoid Particles

MLS numerical simulations were conducted for an ellipsoidal particle of radius $r_z = 200$ nm and $r_x = r_y = 50$ nm at various angles of rotation. The results are presented in Figures 2.15–2.18. The figures contain several subplots, including: a three dimensional representation of the relative light intensity recorded [left], a two dimensional slice of the relative light intensity [top right] as well as a three dimensional visualization of the ellipsoidal particle [bottom right]. In both three dimensional representations [left and bottom right] a red arrow demarcates the direction of the emitted rays.

Upon inspection of the light scattered on the X-Y plane of the 200 nm × 50 nm particle rotated 90° in Figure 2.16, the two dimensional scatter plot appears to resemble that of a 200 nm particle. However, upon closer inspection, the intensity decreases at π rad (180°). This decrease in intensity may be due to the lack of constructive interference which would result from refracted light leaving from the center of the particle.
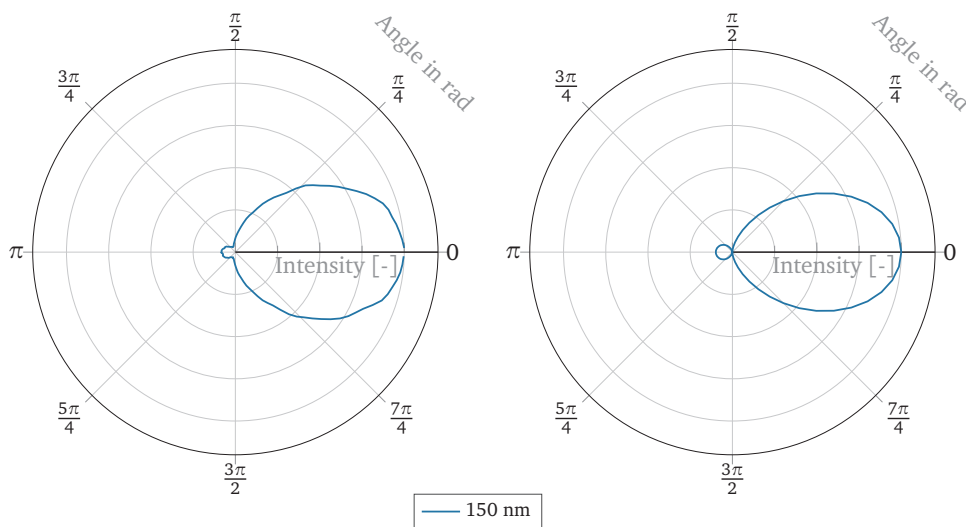
Figure 2.13: *Relative light intensity from 2D montecarlo light scattering [left] and Mie simulations [right] (parallely polarized) of a* 150 nm *radius spherical particle*

Upon inspection of the light scattered on the X-Y plane of the 200 nm × 50 nm particle without rotation in Figure 2.17, the two dimensional scatter plot is initially indistinguishable from that of a 50 nm spherical particle. Only upon inspection of the light scattered vertically (Z-axis), can the difference be spotted. A significant portion of the light being scattered vertically received destructive interference. As such the recorded light intensity is relatively low.

Lastly, inspecting the light scattered on the X-Y plane of the 200 nm × 50 nm particle rotated 45° in Figure 2.18, the two dimensional scatter plot is comparable to that of a 100 nm spherical particle. However, upon inspection of the three dimensional scattering other differences are readily visible. The scattering pattern is no longer symmetrical on the horizontal axis and the necessity for measurements of oriented particles or along multiple axis become imperative.

2.5 Discussion and Outlook

The simulations and measurements conducted in this chapter, outline methodologies for obtaining particle diameter and shape of sub-micrometer particles and aggregates. Two methodologies and their results were presented, SLS, used to measure light
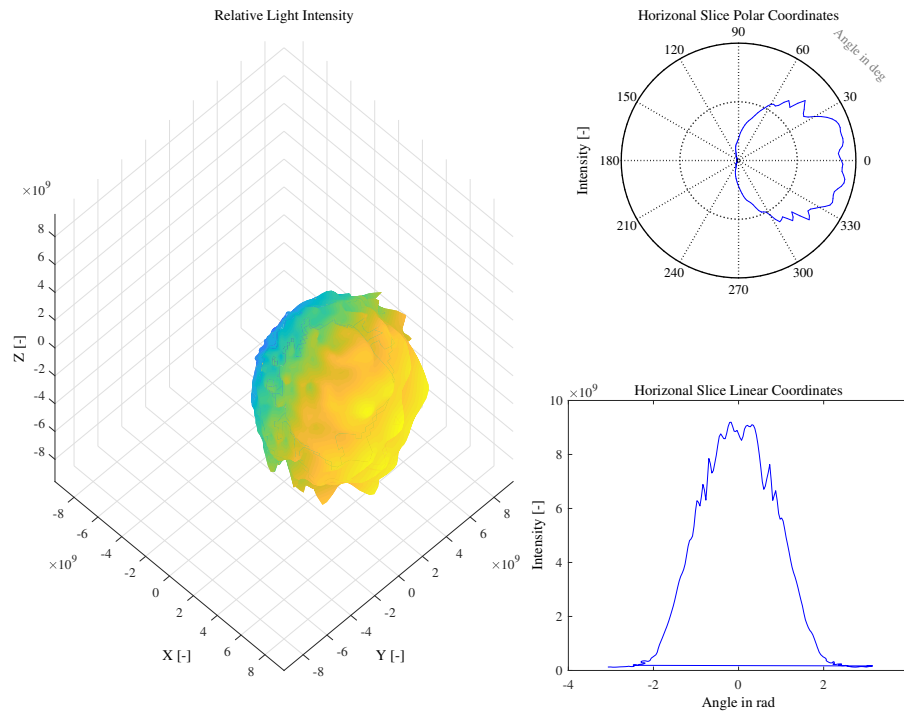
Figure 2.14: *Relative light intensity from 2D montecarlo light scattering simulations of* 100 nm *radius spherical particle.*

scatter from sub-micrometer spherical particles, and MLS, used to simulate light scatter from spherical and non-spherical sub-micrometer particles.

The SLS methodology presented measured side scattering between 20° and 160° around the cuvette, and where the optical probe of the detector was rotated automatically around the cuvette. The measurement took place in 2° and 5° incremental steps. The measurements and subsequent curve fitting demonstrated an accuracy of within 5 % for silica particles of diameter 314 nm, 507 nm, 681 nm, 900 nm and 987 nm. The remaining silica particles of diameter 407 nm, 546 nm, 640 nm and 812 nm, while not accurately characterized demonstrate close resemblance to their numerical counterparts. These results may be further improved by measuring and simulating with a second wavelength to decrease the number of potential particle size matches. Furthermore, it should be noted that the methodology presented here is should not be limited to only Mie scattered light, and may be extended by simulating the angle dependent light scattering for larger and smaller particles.
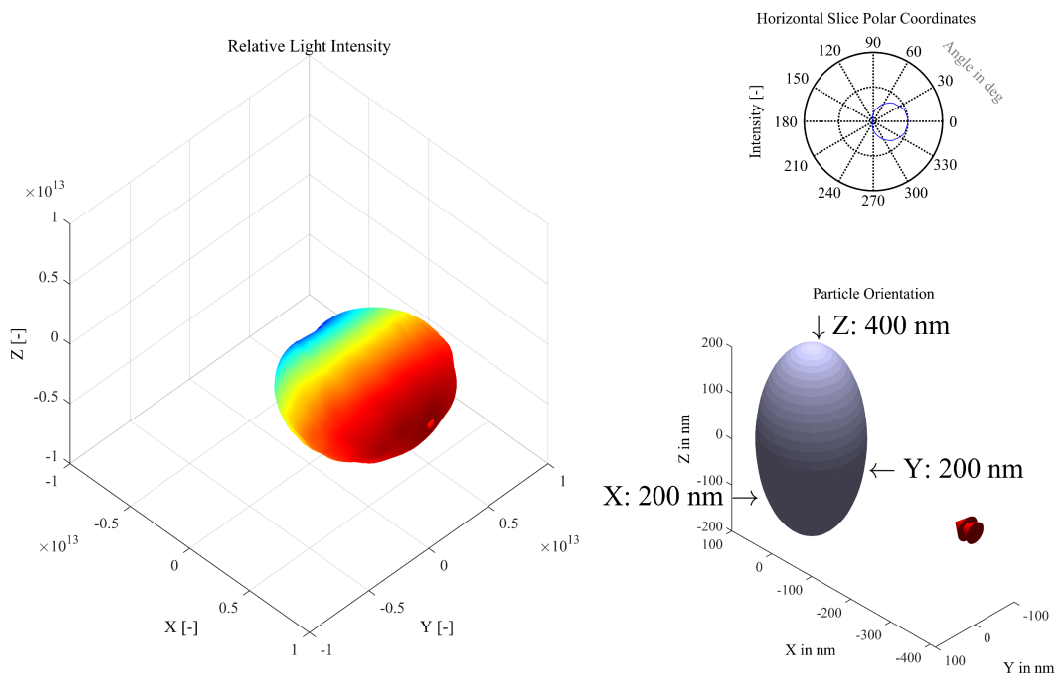
Figure 2.15: *Relative light intensity from 2D montecarlo light scattering simulations of 200 nm × 100 nm radius ellipse at 0°.*

The SLS curve matching results demonstrate that further research and improvements to the classification methodology are warranted. While least squares methods may be challenged due to the significant magnitude differences of the peaks and troughs of the measurements, these and other methods should be further tested. For example, measuring the Fréchet distance and using Dynamic Time Warping (DTW) [21] between the two curves may provide additional flexibility when searching for similarities between the measurement and simulated curves. These algorithms must be evaluated however, to ensure the warping of the measurement curves does not impact the accuracy of the prediction.

In the future, it would also be of interest to add polarizing filters to the detector to obtain additional layers of information, which could be combined to obtain enhanced diameter resolution. Furthermore, the influence of bimodal systems could be evaluated, building upon work conducted previously [78]. Proceeding beyond bimodal systems, light scattering can also be simulated using procedurally aggregated silica particles [68].
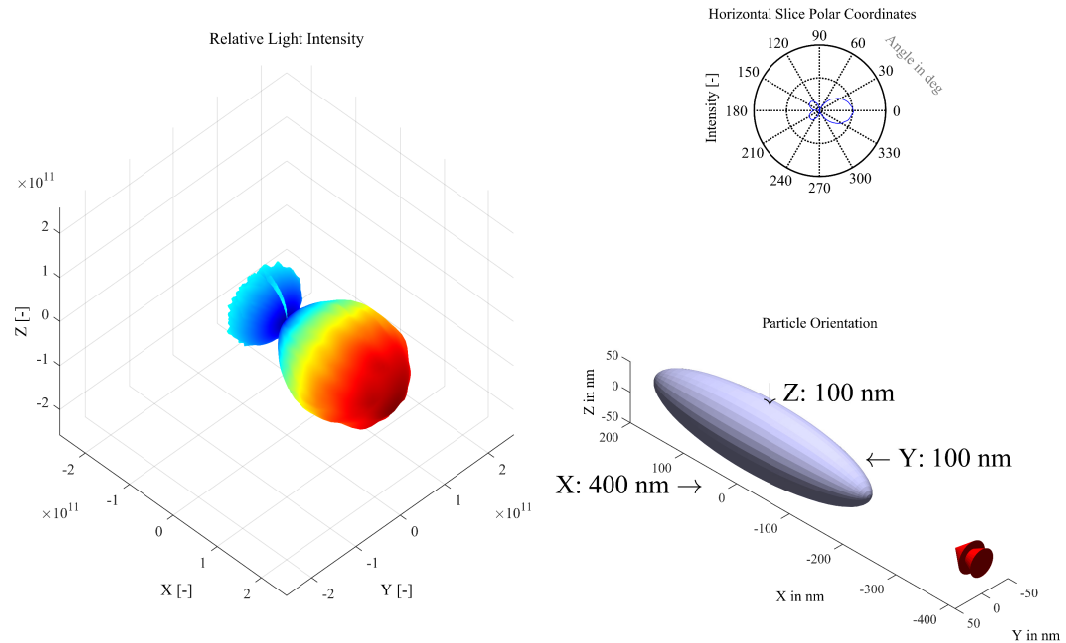
Figure 2.16: *Relative light intensity from 2D montecarlo light scattering simulations of 200 nm × 50 nm radius ellipse rotated 90°.*

Preliminary results were presented using SLS to evaluate particle shape. Spherical particles were measured on several measurement axis and the evaluated particle sizes combined to create a three dimensional prediction of the particles form. The particles height was evaluated to be 585 nm, representing a relative error of 17 %. While it is assumed that the particles are perfectly spherical, this assumption must be confirmed with the manufacturer. Thereafter, the multi axis measurements should be used to calibrate the measurements. It is possible that the additional glass present in the −30°, −15° and 15° measurements causes alterations to the scattering profile of the particle. These alterations should be investigated and incorporated into the curve matching algorithm. Further studies should thereafter be conducted using ellipsoidal particles of known diameter and sphericity.

The results of the MLS from the spherical particles demonstrated particularly good agreement with the results of Mie scattering for the same particle diameter. Further simulations were conducted on ellipsoidal particles which expose the necessity of evaluating three dimensional light scattering for non spherical particles. While the current implementation of the MLS workflow currently assumes purely convex forms, such that a ray leaving the particle will not intersect a second time with the particle.
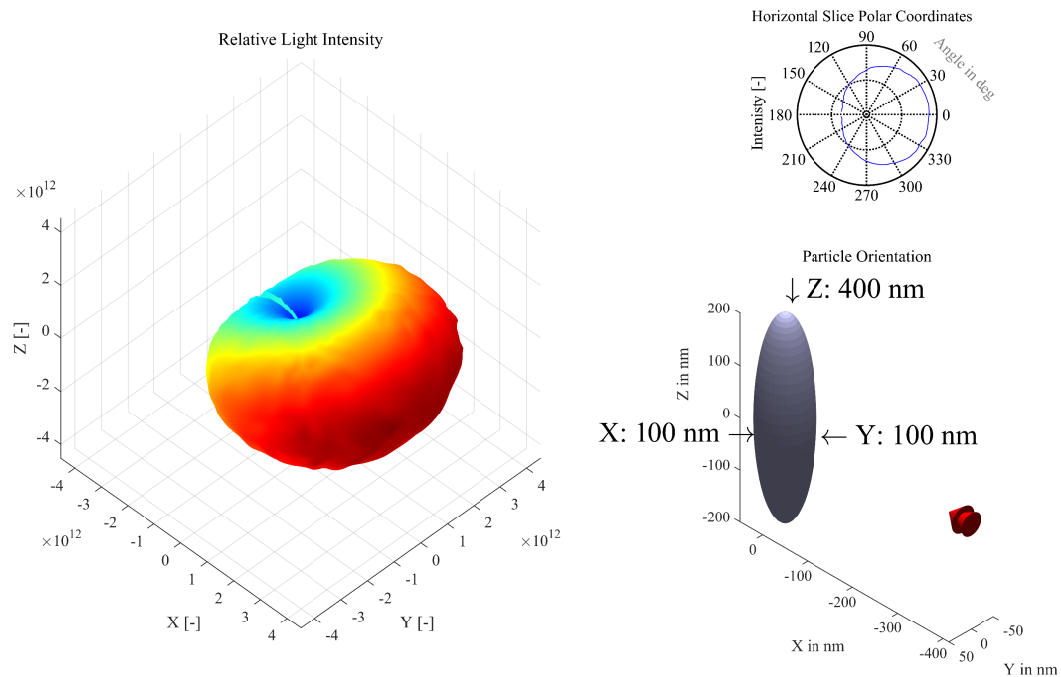
Figure 2.17: *Relative light intensity from 2D montecarlo light scattering simulations of* 200 nm × 50 nm *radius ellipse rotated* 0°.

Initial work was conducted to include secondary intersections, which would not only allow for concave particles, but also particle clusters. However, a reference method must be generated to verify results. Further work is recommended to consider diffracted and refracted rays separately to capture polarization effects.

In order to use these measurements to evaluate aggregate size and form, a rigorous size classification is required, to separate the silica aggregates by size. Each class would be measured with SLS using the volume or weight of each class to define the probability density distribution. The narrower that each class can be made, the more precise the diameter and shape prediction becomes. The ultimate goal will be to develop an inline system for evaluating particle size during the synthesis of precipitated silica in order to control its precipitation parameters, allowing to obtain precise particle/aggregate diameters and forms.
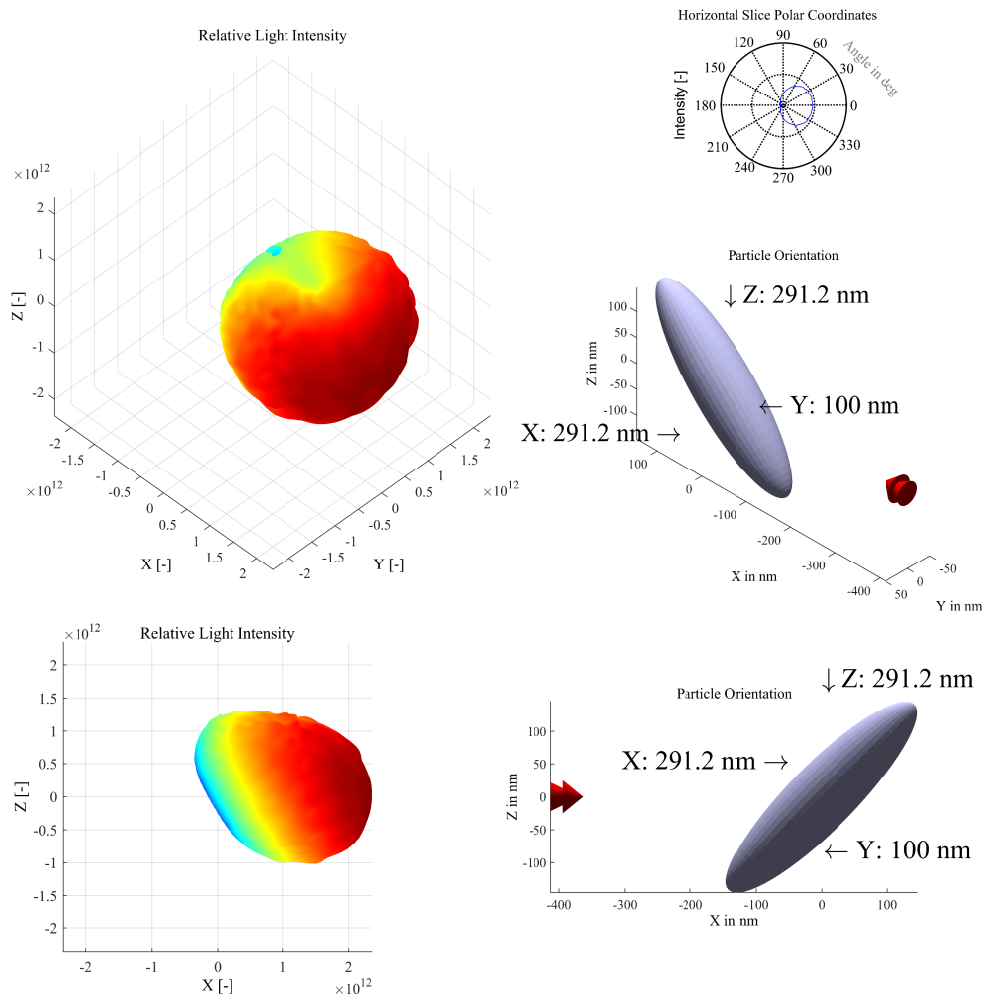
Figure 2.18: *Relative light intensity from 2D montecarlo light scattering simulations of 200 nm × 50 nm radius ellipse rotated 45°.*

2.6 Conclusion

The goal of this chapter was to provide a methodology to obtain diameter and shape information from sub-micrometer silica particles. This was achieved through the use of Static Light Scattering (SLS), to measure a particle's diameter, together with preliminary results of the particle's shape. Furthermore, a second methodology using Montecarlo Light Scattering (MLS), was presented to augment the shape determination of non-spherical particles, necessary when evaluating the shape of silica aggregates.

3

Modeling and Generation of Silica Geometries

We can describe a sphere packing in R^n just by specifying the centers u and the radius. Everything is done with coordinates, and there is no need to draw pictures. There has been a great deal of nonsense written in science fiction about the mysterious fourth dimension. One should certainly not think that the fourth dimension represents time. In mathematics 4-dimensional space just consists of points with four coordinates instead of three (and similarly for any number of dimensions).

John H. Conway

3.1 Aims and Overview

The goal of this chapter is to develop a methodology for geometry generation of sub-micrometer particles in order to obtain a representative periodic packing of silica aggregates. The provided methodology should procedurally generate sub-micron particle geometry directly from particle measurement data.

This chapter is organized as follows. The motivation is presented in Section 3.2. Thereafter included in the methods is a description of the generation algorithms for silica based Vacuum Insulation Panel (VIP) media in Sections 3.3.1–3.3.4, followed by the calculation of the local pore distance in Section 3.3.5. To complete the methods for this chapter, the estimation of the pore size distribution is described in Section 3.3.6. The results are thereafter presented, with the validation of the pore size presented in Section 3.4.1, the results of the pore overlap reduction in Section 3.4.2 and pore size distribution analysis in Section 3.4.3. Lastly, a discussion and outlook are presented in Section 3.5 and conclusion in Section 3.6.

The aggregate generation methodology, validation and analysis presented in this chapter has been developed and performed by Jesse Ross-Jones and has been previously published in *Conjugate heat transfer through nano scale porous media to optimize vacuum insulation panels with lattice Boltzmann methods* [68] and *Pore-Scale Conjugate Heat Transfer Simulations Using Lattice Boltzmann Methods for Industrial Applications* [70]. The pore distance field was developed in collaboration with Maximilian Gaedtke with analysis and further processing performed by Jesse Ross-Jones.

3.2 Motivation

By developing a procedural methodology for generating particle geometry, multiple geometries can be generated based on the same base geometry. For example, different levels of compression can be applied to procedurally generated aggregates, allowing for control over the aggregate size, shape and pore size distributions. The end result is a set of similarly packed geometries of slightly varying pore and particle sizes. This methodology allows for investigation of the influence of small changes in aggregate pore size on thermal heat transfer. Furthermore, the effects of aggregate shape and particle size distribution on heat transfer can also be investigated.

Furthermore, the procedural methodology is modular providing several advantages to having independent geometry workflows. By having independent workflows, different compression ratios can be obtained from the same base geometry, enabling further study into macroporosity effects on heat transfer. Furthermore, should different aggregate generation methods be used, the aggregates can still be imported directly by the workflow without necessitating reprogramming.

3.3 Methods

In this section, the methodology for geometry generation is presented in Sections 3.3.2–3.3.4, followed by a description of the methodology for evaluation of the local pore distance in Section 3.3.5, and the estimation of the pore size distribution in Section 3.3.6.

3.3.1 Geometry Generation Overview

A multi-scale description of the precipitated silica samples is generated from the Mercury Intrusion Porosimetry (MIP), Small Angle X-Ray Scattering (SAXS) and Analytical Ultracentrifugation (AUC) measurements, which have been summarized in Chapter 2, Table 2.1 [56]. The open source framework for discrete element methods, *Yet Another Dynamic Engine* (YADE DEM), is used to generate the geometry and compress the resulting aggregates [74]. The generation of packing geometry is composed of three workflows. The first workflow generates a set of silica aggregates, the second workflow creates a randomized loose packing of the silica aggregates, while the third workflow compresses the silica aggregate packing. Each workflow is described in the following sections. The workflows are diagrammatically presented in Figures 3.1–3.3, and the *YADE* functions used are included in the relevant steps of the diagrams. The geometry generated is passed automatically to *OpenLB* to simulate the Effective Thermal Conductivity (ETC), described in Chapter 4.

The overall packing porosity (Π) of the precipitated silica samples used in this study, measured using Mercury Intrusion Porosimetry (MIP), range from 85 % to approximately 90 %. The primary pore sizes, estimated from the MIP measurements, (d_{pore}) range from 5 nm to 28 nm. The primary particle diameters, measured using Small Angle X-Ray Scattering (SAXS), (d_p) range from 7 nm to 25 nm. The SAXS measurements also provide the fractal dimension of mass (D_{mf}) and surface (D_{sf}). A mass fractal dimension can range between 1 and 3, where 1 indicates a long cylindrical form, 2 a disk-like form and 3 a spherical form [32]. The mass fractal dimension of the silica samples, varies between 1.85 and 2.25, describing predominantly disc-like aggregate structures. The surface fractal dimension characterizes a particle's roughness, and can range from near 2 (smooth surface) to 3 (rough surface) [53]. The surface fractal dimension of the silica samples, ranges from 1.88 to 2.08, describing smooth particle surfaces. The description of a smooth surface, also indicates that representing the particles as spheres is appropriate. Lastly, the aggregate diameter (d_{agg}) of the silica

samples, measured using Analytical Ultracentrifugation (AUC), varies between 107 nm and 120 nm with a standard deviation (σ_{agg}) between 13 % and 28 %.

3.3.2 Aggregate Generation

The first workflow, presented in Figure 3.1, generates parameter data sets describing silica aggregates. The first step of this workflow sets the number of different aggregate data sets to generate, the silica primary particle size, primary pore size, aggregate shape and diameter as well as diameter standard deviation. To model the distribution of the aggregate diameter, a list of diameters is generated following a normal distribution. This is accomplished with *rand.normal* from the python numpy package. The parameter inputs to *rand.normal* are the aggregate average diameter, the standard deviation and the number of aggregates requested: *rand.normal(d_{agg}, σ_{agg}, num_{Agg})*.

For each element in the list of aggregate sizes, a particle cloud is generated using the *YADE* function *makeCloud()*. The diameter parameter for the particles is defined by the silica primary particle diameter. Moreover, *makeCloud()* allows for particle generation with a size distribution, which will be incorporated once further measurements have been made, and the primary particle size distribution estimated. A secondary particle cloud is generated which represents the internal pores of the silica aggregates. These particle diameters are defined by the pore sizes measured with MIP. The two particle clouds are appended simultaneously and added to the simulation space using the *YADE* function *O.bodies.append()*.

The two particle packings are compressed using *TriaxTest()* which compresses on all axis isotropically. The internal nano-porosity of the aggregates is maintained, due to the presence of the pore spheres packing. When the compressed packing dimensions are larger than the requested aggregate diameter, then the aggregate form can be generated using a defined predicate *yade.pack.inElliposid()*. The aggregate shape is inferred from the mass fractal dimension measurement, where 1 indicates a long cylindrical form, 2 a disk-like form and 3 a spherical form [32]. Only the silica particles which are contained within the aggregate shape are exported using *yade.export.textClumps()*. This function exports a list of sphere locations and sphere radii: *x, y, z, r*. The pore particles are not exported, resulting in voids in the aggregate packing.

These steps are repeated for each aggregate diameter requested. By exporting each aggregate in separate files and by using a modular workflow, future improvements

are easily integrated. For example, other works have suggested using diffusion limited cluster-cluster methods [47] to generate aggregates. The aggregates could be generated and exported using a similar text format and passed to workflow 2 without requiring the workflow to be altered.

3.3.3 Loose Packing Generation

The second workflow, presented in Figure 3.2, generates a loose packing of silica aggregates. The aggregates generated by the first workflow are imported using *yade.ymport.textClumps*. A pre-defined volume is filled with randomly placed and rotated aggregates using *yade.makeClumpCloud*. The function *makeClumpCloud* takes as parameters: the minimum and maximum corners of the defined volume, a list of lists containing the locations of each particle in each aggregate, as well as the *periodic* = **True** flag to generate periodic boundaries and *num* = **-1** which fills the volume with as many aggregates as possible. Thereafter, to keep track of the aggregates, each particle belonging to an aggregate is assigned a group index. This index is used by the third workflow. The loose packing is exported using *yade.export.textExt*, which exports a list of sphere locations, sphere radii and aggregate group indices: *x, y, z, r, i*.

3.3.4 Compressed Periodic Packing Generation

The third workflow, presented in Figure 3.3, generates the periodic packing of compressed silica aggregates. The loose packing generated in the second workflow is imported using *yade.ymport.textExt*, which additionally parses the aggregate indices. By using the index, each particle is re-grouped and appended to the simulation as an aggregate.

The *YADE* particle compression engine *PeriTriaxController* is initialized and then run within a while loop: *while porosity() > targetPorosity*. The compression engine applies periodic forces equally on all axis and uses virtual/ghost particles, mirrored across the boundaries, to ensure periodic compression. The engine runs in small increments within each iteration, with *O.run(5000,True)*, which runs for 5000 time steps and the True flag indicating the simulation should wait for further instructions before terminating. Using the total porosity of the silica, measured with MIP, the target porosity of the packing is defined. The total porosity is the total pore volume over the whole volume, where the total pore volume includes the pores between
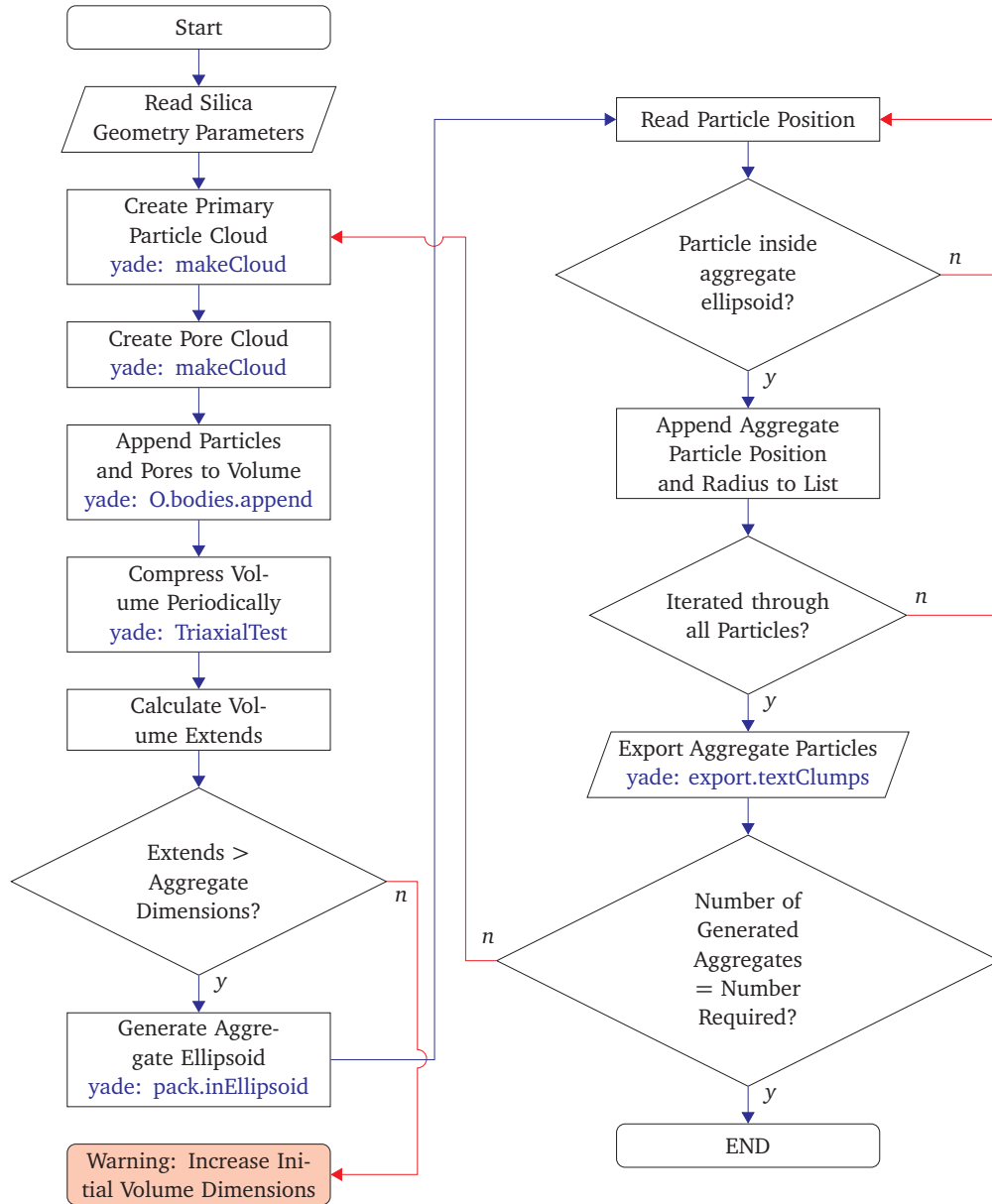
```
                ┌─────────────────┐
                │     Start       │
                └─────────────────┘
                         │
                         ▼
              ╱──────────────────╲
              │   Read Silica     │
              │ Geometry Parameters│
              ╲──────────────────╱
```

Start

Read Silica Geometry Parameters

Create Primary Particle Cloud
yade: makeCloud

Create Pore Cloud
yade: makeCloud

Append Particles and Pores to Volume
yade: O.bodies.append

Compress Volume Periodically
yade: TriaxialTest

Calculate Volume Extends

Extends > Aggregate Dimensions?

n

y

Generate Aggregate Ellipsoid
yade: pack.inEllipsoid

Warning: Increase Initial Volume Dimensions

Read Particle Position

Particle inside aggregate ellipsoid?

n

y

Append Aggregate Particle Position and Radius to List

Iterated through all Particles?

n

y

Export Aggregate Particles
yade: export.textClumps

Number of Generated Aggregates = Number Required?

n

y

END

Figure 3.1: *Algorithmic flowchart of aggregate geometry generation*
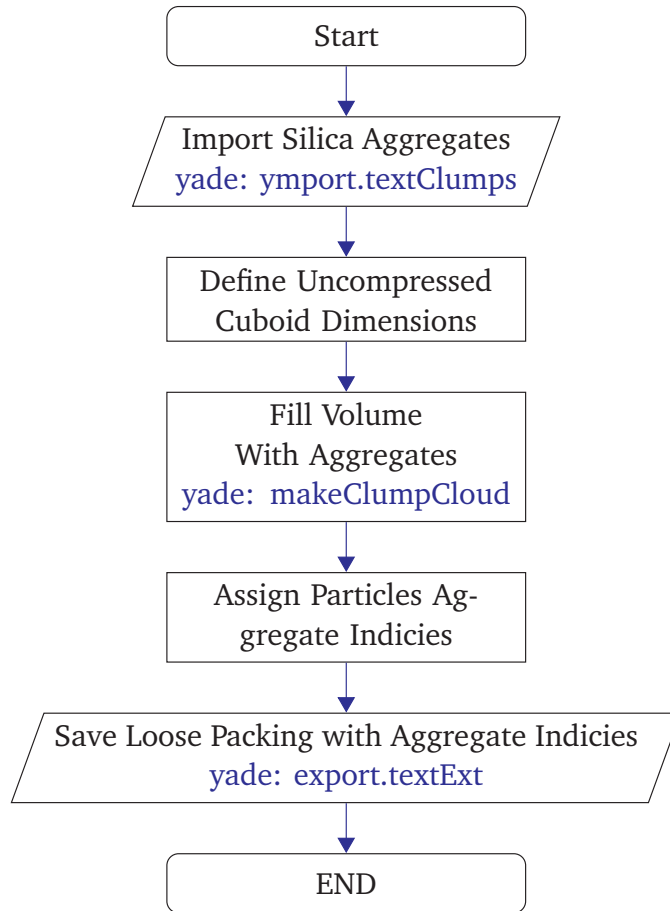
Figure 3.2: *Algorithmic flowchart of loose packing geometry generation*

aggregates as well as the pores within the aggregates. The particles, within each aggregate, are rigidly constrained. Therefore, compression forces acts to reduce the bulk packing porosity without affecting the internal aggregate pore volume.

Once the target porosity has been reached, the volume dimensions are calculated. These dimensions are necessary in order to replace the virtual/ghost particles, used in the periodic compression, with real particles. The particles are copied across the x, y, z planes as well as the xy, xz, yx and xyz planes to generate a fully periodic packing. Just before the final export, a last parameter allows for the adjustment of particle diameter in order to compensate for particle-particle point contacts. The particles and volume are then separately exported as XML files for later use in *OpenLB* [27].

The packing volume is encapsulated in a *IndicatorCuboid3D*, and is necessarily exported to define the periodic boundary limits of the packing, in order to recreate these boundaries in *OpenLB*. This is exemplified in the XML in Source Code 3.1.
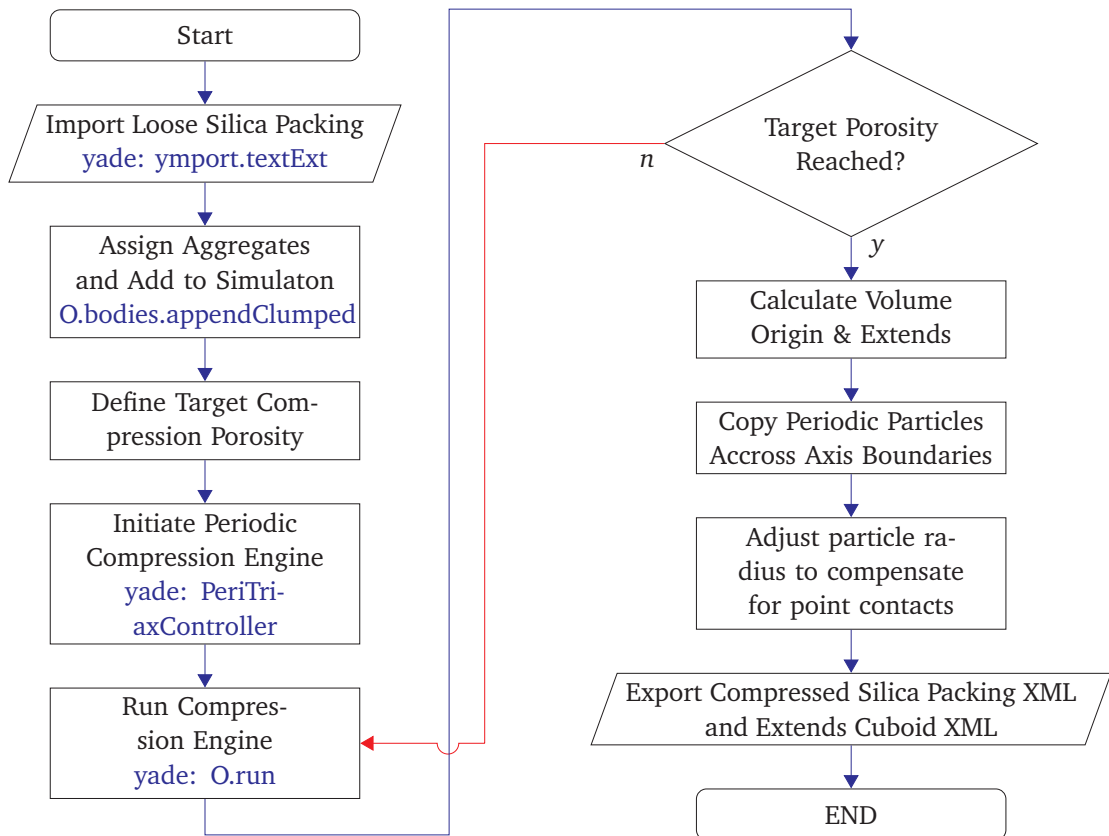
Figure 3.3: *Algorithmic flowchart of compressed packing geometry generation*

```xml
1 <?xml version="1.0" ?>
2 <IndicatorUnion3D>
3   <IndicatorCuboid3D
4     extend="xDim yDim zDim"
5     origin="xOrigin yOrigin zOrigin" />
6 </IndicatorUnion3D>
```

Source Code 3.1: *Indicator Cuboid*

The compressed particles are similarly encapsulated in a list of *IndicatorSphere3D*. Each particle is defined with its x, y, z location and radius as shown in Source Code 3.2.

```xml
1  <?xml version="1.0" ?>
2  <IndicatorUnion3D>
3    <IndicatorSphere3D
4      center="xOrigin1 yOrigin1 zOrigin1"
5      radius="radius1" />
6    <IndicatorSphere3D
7      center="xOrigin2 yOrigin2 zOrigin2"
8      radius="radius2" />
9    <IndicatorSphere3D
10     center="xOrigin3 yOrigin3 zOrigin3"
11     radius="radius3" />
12   ...
13 </IndicatorUnion3D>
```

Source Code 3.2: *Indicator Sphere*

3.3.5 Local Pore Distance

The local pore size is defined here as the distance from each lattice point to the closest particle's surface. This calculation would normally be computationally inhibitory, however, by taking advantage of the particle packing being defined analytically instead of as a surface mesh, the local pore size can be calculated efficiently. For each lattice point, the list of particles is iterated over, and the minimum euclidean distance from the lattice center to the each particle center minus the particle radius is calculated. The resulting minimum is then the distance from the current lattice point to the closest silica particle surface.

The distance field is used to calculate the local heat transfer through the fluid as shown in Equations (3.1)–(3.3),

$$\lambda_f(p_f) = \frac{\lambda_{f0}}{(1 + 2\beta \cdot Kn)} \qquad \text{in } W/mK \qquad (3.1)$$

where λ_{f0} is the effective heat transfer in a continuum (26.606×10^{-3} W/m K [81]), and β is a weighting factor representing the efficiency of energy transfer between gas molecules and the solid boundaries. Commonly used β values for air and water vapor are 1.63 and 1.5 respectively [81]. Kn is the Knudsen number, which is the ratio

of the mean free path of the gas molecules and the characteristic length, outlined in (3.2).

$$Kn = \frac{l_f}{\Phi} \tag{3.2}$$

In this case the characteristic length, Φ, is defined as the local pore size, and the mean free path, l_f, is further expanded in (3.3),

$$l_f = \frac{1}{\sqrt{2}\pi\sigma_f^2 n} \qquad \text{in } m \tag{3.3}$$

with n being the number of molecules per volume $\frac{N}{V}[m^{-3}]$ and σ_f the molecular diameter. For air, the molecular diameter is $\sigma_f = 3.7 \times 10^{-10}$ m [62].

As the internal pressure decreases, the mean free path increases, which in turn increases the Knudsen number. As a result, as shown in (3.1), the heat transfer through the fluid/gas decreases, [28, 81].

3.3.6 Pore Size Distribution Estimation

Through further processing of the distance field a pore size distribution is estimated. The methodology is based on maximum inscribed spheres, which is described in further detail by Silin et al. and Dong et al. [20, 72]. From the distance field described in Section 3.3.5 and displayed graphically in Figure 3.5, local maxima are evaluated. Each maxima represents the largest inscribed sphere fitting within the local pore [54].

To obtain an accurate evaluation of the pore size distribution, the radii of the maximum inscribed spheres must be reduced slightly so as to remove existing overlap with the neighboring pores. See Figure 3.6 for a visualization of the pore size reduction and Figure 3.7 which shows the change in the pore size distribution after the reduction.

The algorithm uses a form of Axis Aligned Bounding Box (AABB) [8] collision detection to reduce the computations by performing a filter for potential collisions. Furthermore, since collisions are detected locally, the algorithm is apt for use in distributed processes. The implementation is available in the code repository described in the Appendix Section D. The first step reads the Paraview VTI file and creates a *filter* for

$physPoreSizeDistribution > 0.0$, which generates a list of coordinates and distances representing the local maxima, as seen in Source Code 3.3.

```python
reader = vtk.vtkXMLImageDataReader()
reader.SetFileName(path + filename)
reader.Update()

reader.PointArrayStatus = ['geometry', 'physBoundaryDistance',
    'physPoreSizeDistribution']

usg = dsa.WrapDataObject(reader.GetOutput())
physPoreSizeDistribution = usg.PointData['
    physPoreSizeDistribution']
physBoundaryDistance = usg.PointData['physBoundaryDistance']

positivePoresfilter = physBoundaryDistance[np.where(
    physPoreSizeDistribution > 0.00)[0]]
poreRadius = physBoundaryDistance[np.where(
    physPoreSizeDistribution > 0.0)[0]]

filter = np.where(physPoreSizeDistribution > 0.0)
```

Source Code 3.3: *Python Read VTI*

In order to efficiently detect pore overlap the individual pores are projected onto the X, Y and Z axes. Only pores which intersect on all three axes are potentially overlapping. To accomplish this, an array of *pores* as well as $arrayX$, $arrayY$ and $arrayZ$ are needed. Where *pores* contains the complete list of $poreID$, X, Y and Z coordinates as well as the *radius* of each pore. The arrays $arrayX$, $arrayY$ and $arrayZ$ contain two columns with the $poreID$ in the first column and the starting point or ending point of the pore in the second. The start and ending points are calculated by taking the X, Y, or Z coordinates of each pore and subtracting or adding the pore's radius respectively.

The *pores* array is then sorted by *radius* from smallest to largest and $arrayX$, $arrayY$ and $arrayZ$ are stored by the second column containing the starting or ending points on each axis. Iterating then through *pores* (again from smallest radius to largest), the $poreID$ is used to crop $arrayX$, $arrayY$ and $arrayZ$ between the starting and ending points of the current pore on each axis. Following, by taking the union of the three cropped arrays, a list remains containing the pores which may intersect with the current pore. The overlap distance, being the distance between the pore

centers minus the radius of each pore, is calculated for these pores only. If the overlap distance is less than zero, then the pores overlap and the radius of the smaller of the two pores is reduced by the overlap distance.

3.4 Results and Validation

In this section the geometry generation as well as two and three dimensional normal methodologies are evaluated. The pore distance calculation is first validated in Section 3.4.1. Thereafter, the pore size reduction algorithm is evaluated for computational efficiency in Section 3.4.2. Following, the estimated pore size distribution is compared to the original measurements in Section 3.4.3.

3.4.1 Validation of Numerical Pore Size
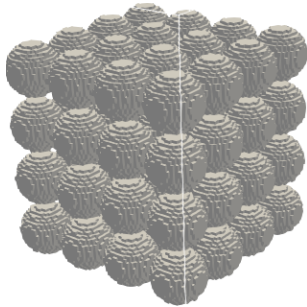
Figure 3.4: *Cubic ordered packing used for validation of pore distance evaluation*

The pore distance calculation was validated against the analytical solution for an ordered packing of spherical particles. A compact simple cubic ordered packing was generated with a particle size of $0.4\,\mathrm{m}$. The packing is shown in Figure 3.4. Following the pore distance calculation described in Section 3.3.5, a pore size of $0.2928\,\mathrm{m}$ was calculated. This result matches the analytical solution for a cubic packing which has a known pore size of $0.366 \cdot 2 \cdot radius$ [30, 65]. As mentioned, here the pore size is defined as the largest inscribed sphere fitting within a pore.

A visualization of a two dimensional slice of the distance field is presented in Figure 3.5, where solid blue indicates points located within a silica particle, and a gradient from light blue to deep red indicates an increasing pore size.

3.4.2 Evaluation of Pore Overlap Reduction

In order to properly evaluate the pore size distribution of the generated geometries, the pore sizes obtained from the distance field are reduced to eliminate overlapping pores. This algorithm is described in Section 3.3.6. Visually, the results of the algorithm are presented in Figure 3.6, with the pores in red obtained from the local maxima of the distance field, and in blue the result of the reduced non-overlapping pores. Both

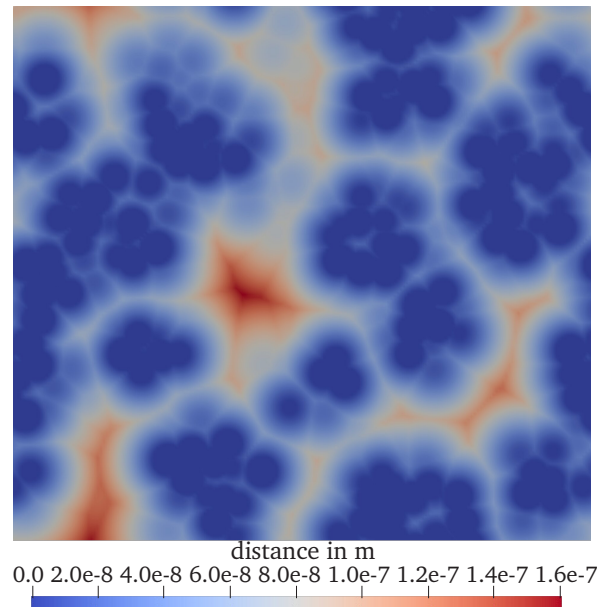distance in m
0.0 2.0e-8 4.0e-8 6.0e-8 8.0e-8 1.0e-7 1.2e-7 1.4e-7 1.6e-7

Figure 3.5: *Two dimensional slice of the distance field used for the local heat transfer simulation within each pore. Solid blue indicating the lattice is located within a particle, light blue to deep red indicating an increasing pore size.*

pore systems are presented as maximum inscribed spheres. Looking further at the pore distribution shown in Figure 3.7, a shift is visible towards smaller pores after the reduction. Furthermore, a significant number of larger pores are no longer present. These results highlight the importance of the pore overlap reduction when comparing generated geometries to measurement values.

The performance of the pore overlap reduction implementation is also evaluated. By comparing the elapsed time for the computation of pore overlap and radius reduction, a clear advantage is apparent from the provided implementations over a brute force implementation where each pore is checked for overlap with every other pore, see Figure 3.8. The implementation grows linearly with increasing number of pores, while the brute force method grows exponentially.

3.4.3 Analysis of Pore Size

In order to evaluate the geometry produced by the described methodology in Sections 3.3.2–3.3.4, visual data analysis is conducted using the pore size distributions.
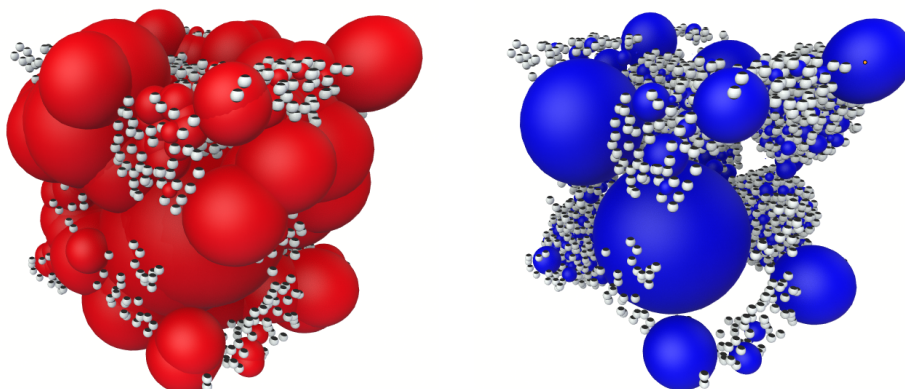
Figure 3.6: *Visualization of pores in red [left] from the local maxima of the distance field as seen in Figure 3.5, and reduced non-overlapping pores in blue [right]. Both pore systems are presented as maximum inscribed spheres.*

Moreover, a visualization of the geometry generation for a GT sample is presented in Figure 3.9, showing the aggregate and pore extraction on the left and the compressed and periodic packing of aggregates on the right.

The pore diameter cumulative density function (see Reboul et al. [66] for more detail) is displayed graphically in Figure 3.10. Both the GT and KS samples, with similar primary particle and aggregate sizes, follow similar distributions. Both samples contain an increased number of larger pores (larger than 10 nm). On the other hand, the CP sample, with both smaller primary particles and smaller aggregates, contains an increased number of smaller pores (between 1 and 10 nm).

In addition to the cumulative distribution curves, the average primary pore size of silica samples, reported by Meier et al. [56], are displayed as vertical bars, GT (28.3 nm), KS (25.2 nm) and CP (9.1 nm), see Table 2.1. The KS geometry has a particularly large number of pores centered around its corresponding value. This sudden increase is not visible for the CP sample which only has an increased number of smaller primary pores (9.1 nm). Statistical details regarding the pores is also displayed in Table 3.1, which also demonstrates CP having much smaller pores and a shifted distribution.
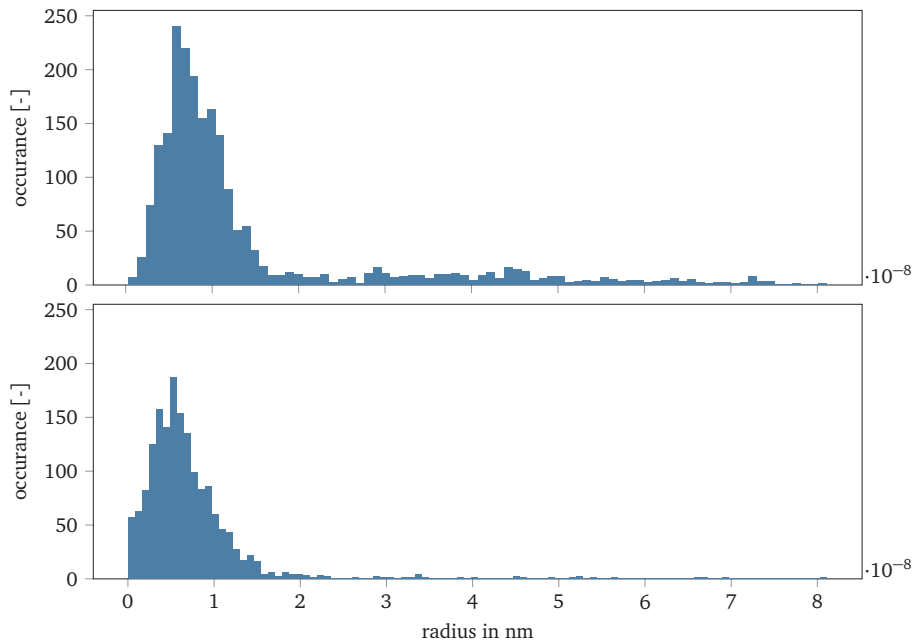
Figure 3.7: *Change in pore size distribution of sample CP*
Above: Original overlapping radii distribution of pore sizes
Below: Reduced non overlapping radii distribution of pore sizes

Table 3.1: *Pore distribution statistics for GT, KS and CP silica samples.*

	Unit	GT	KS	CP
count	-	3.45×10^{3}	2.14×10^{3}	3.43×10^{3}
mean	m	1.30×10^{-8}	1.21×10^{-8}	1.06×10^{-8}
std	m	1.54×10^{-8}	1.33×10^{-8}	9.39×10^{-9}
min	m	3.04×10^{-11}	6.05×10^{-13}	4.02×10^{-12}
25%	m	5.98×10^{-9}	5.29×10^{-9}	4.75×10^{-9}
50%	m	9.14×10^{-9}	8.24×10^{-9}	8.66×10^{-9}
75%	m	1.52×10^{-8}	1.41×10^{-8}	1.41×10^{-8}
max	m	4.05×10^{-7}	1.42×10^{-7}	1.01×10^{-7}

3.5 Discussion and Outlook

The algorithms presented and evaluated in this chapter outline the methodology for generating sub-micron silica geometry used in the upcoming heat transfer numerical simulations in Chapter 4. Three methodologies for geometry generation were
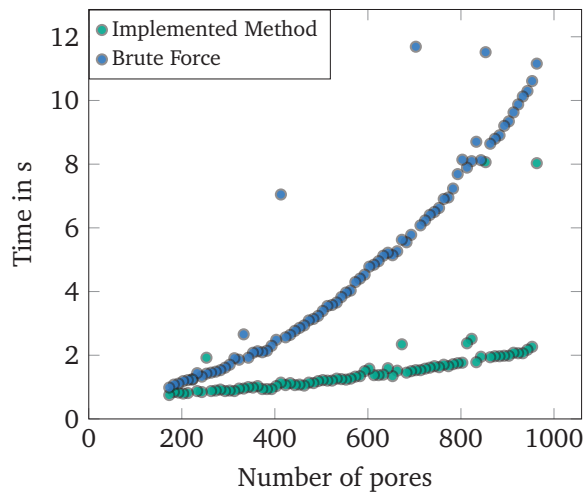
Figure 3.8: *Elapsed time benchmarking of implemented method and brute force detection of pore radius reduction for overlapping pores.*

presented. The first to generate individual aggregates in Section 3.3.2, followed by the second to generate a loose packing in Section 3.3.3 and the third to generate a compressed periodic packing of silica aggregates in Section 3.3.4. Furthermore, the algorithm for the characterization of the local pore field was presented and the pore field was evaluated.

A significant assumption affecting the silica geometry generation, was made in regards to the form of the silica aggregates. In Chapter 2, the methodology was presented to obtain information regarding the aggregates shape. While this information is not yet available for precipitated silica, further studies should be conducted to understand the impact of other aggregates on the overall packing geometry and subsequent heat transfer numerical evaluation. Other aggregate generation algorithms may be used as "drop in" replacements for workflow one, such as diffusion limited cluster-cluster methods [47]. Furthermore, when measurements of the primary particle size distribution become available, these can be included directly in the aggregate generation workflow, without changes to the software.

The geometry generation was evaluated by calculating the pore size distributions, with results demonstrating acceptable agreement with the measurements. However, a direct comparison of these distributions to silica porosity measurements is challenging, due to the differences in the measurement methodology and the assumptions made.
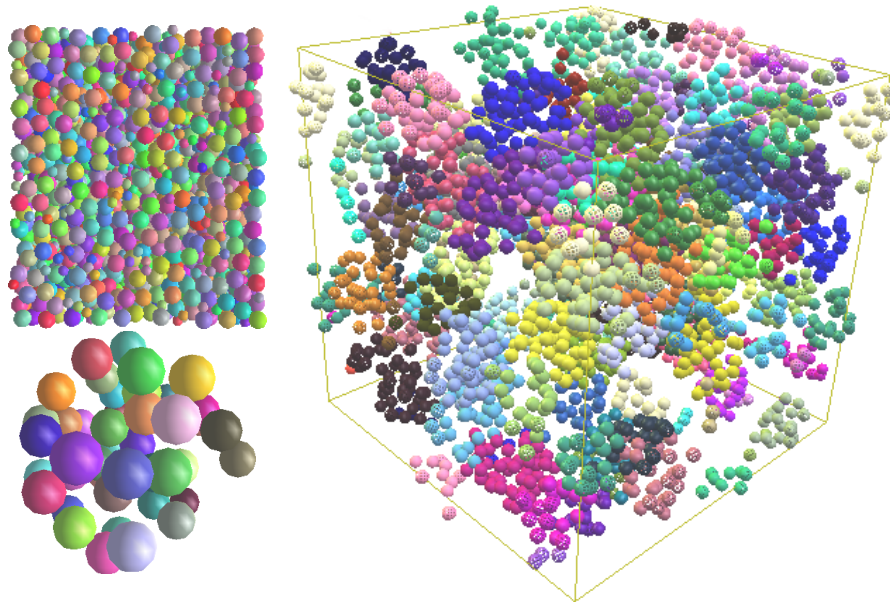
Figure 3.9: *Visualization of geometry generation for the sample GT. On the [top left], two compressed particle systems, silica primary particles and pores. In the [bottom left], particles outside of aggregate predicate are removed, the pore particle system is also removed. On the [right] a periodic compressed packing of GT aggregates, each aggregate is rigid and only compressed externally.*

In this work, the pores are evaluated as maximum inscribed spheres fitting within the pore, whereas the MIP measurement measures the entire pore volume. Since the volume and/or diameter of a maximum inscribed sphere is slightly smaller than the equivalent volume/diameter of the entire pore, the pore distributions evaluated in this work would be shifted slightly towards smaller radii. Furthermore, the geometries generated were not evaluated for particle-particle contacts which is an important consideration for solid thermal conductivity. However, a parameter is included in the third workflow to adjust the particle radius after compression. This adjustment allows for studies to be performed evaluating the influence of the particle contact area on the silica's ETC.

Through an extension of the proposed methodology, various additional structures may also be imported as aggregates and included in the geometry packing. Two potential use cases would be for the addition of structural fibers and/or opacifier particles. Structural fibers are often used to increase mechanical stability of VIPs. However, these impact the thermal conductivity [19], thus requiring a balance to
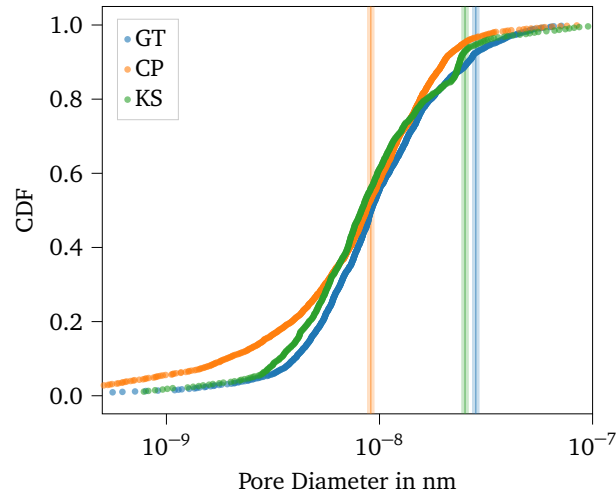
Figure 3.10: *Cumulative density function of pore diameters with vertical bars as indicators of the average primary pore sizes of silica samples GT (28.3 nm), CP (9.1 nm) and KS (25.2 nm) measured [56].*

be found. Furthermore, opacifiers such as TiO_2 are often used to decrease radiative thermal transfer, however these additional particles also have an impact on the solid conductivity [36]. The methodology proposed here relies heavily on the use of spherical particles; as such, long fibers would be generated as long thin series of overlapping spheres. In the case of opacifier particles, these would be generated in much the same way as the silica aggregates are generated in the first workflow, shown in Figure 3.1. These opacifier aggregates can be directly imported in the second workflow and compressed in the third workflow. By keeping track and exporting the different particle types (silica, structural fibers and opacifiers) as individual XMLs, these structures can be imported separately and their material properties adjusted in *OpenLB* during the simulation setup. By including structural fibers and radiation dampening opacifiers, an understanding is obtained not only of the overall impact on the ETC, but also into effects on the local porosity of the silica media.

3.6 Conclusion

The goal of this chapter was to develop a methodology for geometry generation of sub-micrometer particles to create a representative periodic packing of silica aggregates. The provided methodology procedurally generated sub-micron geometry directly from particle measurement data. The generated geometries were compared to measurements through pore size distribution evaluation.

4

Mathematical Modeling and Simulation of Heat Transfer

They are models, but they don't pretend to be the real world.

Freeman Dyson

4.1 Aims and Overview

The goal of this chapter is to develop a methodology for simulating the effective heat transfer through the geometry generated in Chapter 3. The provided methodology should simulate the necessary components of heat transfer at the nano-scale to estimate Effective Thermal Conductivity (ETC) of the silica based Vacuum Insulation Panel (VIP) media. Furthermore, a secondary goal of this chapter is to provide several tools which will be helpful in the development of slip boundary conditions for rarefied fluid flow simulations. These tools include continuous normal calculation in two and three dimensions as well as test cases for these algorithms.

This chapter is organized as follows. The motivation is presented in Section 4.2. Thereafter included in the methods is a description of the heat transfer mechanisms in porous media in Section 4.3.1, followed by modelling the heat transfer through the VIP media with Lattice Boltzmann Methods (LBMs) in Section 4.3.2. The evaluation of the ETC is described in Section 4.3.3 and the simulation variables are described in Section 4.3.4. To complete the methods for this chapter, a description of tools to aid in the development of slip boundary conditions are presented in Section 4.3.5. The validation of the methods is thereafter presented, with grid independence studies available in Section 4.4.1. The validation for the two and three dimensional normal presented in Section 4.4.2 and Section 4.4.3 respectively, with the slip boundary test case described in Section 4.4.4. Lastly, a discussion and outlook are presented in Section 4.5 and conclusion in Section 4.6.

The LBMs presented in this chapter have been developed in collaboration with Maximilian Gaedtke and have been previously published in *Conjugate heat transfer through nano scale porous media to optimize vacuum insulation panels with lattice Boltzmann methods* [68] and *Pore-Scale Conjugate Heat Transfer Simulations Using Lattice Boltzmann Methods for Industrial Applications* [70]. The two and three dimensional normals were developed by Jesse Ross-Jones.

4.2 Motivation

In this chapter a method, taking the procedurally generated compressed packing of 3D spherical silica described in Chapter 3, to simulate the ETC through VIPs without manual intervention, is presented. The three dimensional geometry generation method implemented provides a distinct advantage over other porous media approaches by allowing direct control and tuning of particle packing characteristics such as aggregate size, shape and pore size distributions and study their influence directly on conduction and radiation independently. Radiation and conduction are coupled in order to simulate heat transfer at the nano-scale and for a range of pressures, from 1 bar down to 1 mBar. This enables an in depth understanding of the heat transfer mechanism at the nano-scale and will lead to both an improvement in the lifetime and reduction of the manufacturing costs of VIPs. OpenLB is used as it is an open source implementation of LBM with a parallel execution capable of handling complex geometry [27].

4.3 Methods

The various components of heat transfer through porous media are presented in Section 4.3.1 for convection, conduction, radiation and the coupling effect. Following, the LBM implementations for conduction and radiation are presented in Section 4.3.2, along with the calculation of the ETC in Section 4.3.3. Thereafter, the methodology for estimation of two and three dimensional normal vectors are presented in Section 4.3.5 and Section 4.3.5 respectively.

4.3.1 Heat Transfer through Vacuum Insulation Panels

Heat transfer through a porous material is composed of the heat transfer through fluid, λ_f, through solid, λ_S, through radiation, λ_R, and a coupling effect, λ_C. The combined sum of these terms provides the total effective heat transfer, λ_ϕ, as shown in (4.1) [28].

$$\lambda_\phi = \lambda_f + \lambda_S + \lambda_R + \lambda_C \tag{4.1}$$

Convection

The heat transfer through a fluid (convection) is given by (4.2), where c_p is the specific heat capacity of the gas, ρ_f the gas density, l_f the mean free path of a gas molecule and v the speed of sound. Moreover, $l_f = (n \cdot \sigma_f)^{-1}$, where n is the number density of the gas molecules and σ_f the effective collision cross-section area.

$$\lambda_f = c_p \cdot \rho_f \cdot l_f \cdot v/3 \qquad \text{in } \frac{\text{W}}{\text{m K}} \tag{4.2}$$

Furthermore, as the internal pressure decreases, heat transfer due to convection decreases. This decrease is inversely proportional to the Knudsen number in (4.3),

$$Kn = \frac{l_f}{\Phi} \tag{4.3}$$

where l_f is the mean free path and Φ the characteristic length [35]. With (4.2) and (4.3), where the characteristic length is in this case the pore diameter of the VIP media, the thermal conductivity of the fluid at sub-atmospheric pressures is

$$\lambda_f(p_f) = \frac{\lambda_{f0}}{(1 + 2\beta_f \cdot Kn)} \qquad \text{in } \frac{W}{m\,K}. \tag{4.4}$$

β_f is a weighting factor which describes the efficiency of energy transfer from gas molecules to the solid boundaries. λ_{f0} is the effective heat transfer in continuum (1 bar pressure). Commonly used β_f values for air and water vapor are 1.63 and 1.5 respectively [81].

Conduction

The solid thermal conductivity, λ_S, of a material is dependent on the density and the thermal conductivity of the compacted material. One proposed method of approximating the thermal conductivity is given by the Glicksmann model in (4.5),

$$\lambda_S = \left(\frac{2 - f_S}{3}\right)\frac{\rho_S}{\rho_{S0}}\lambda_{S0} \tag{4.5}$$

where the mass fraction, f_S, density of the porous material ρ_S, density of the pure compacted material ρ_{S0} and thermal conductivity of the pure compacted material λ_{S0}. In this work the porous silica geometry is resolved, therefore porosity based approximations are not necessary. The value of λ_S through the pure silica is estimated from vitreous silica [37].

Radiation

Heat is transported via radiation directly from surfaces with higher temperatures to surfaces with lower temperatures, when these surfaces are not in direct physical contact with each other. The radiative heat transfer is given by (4.6) [28]

$$\lambda_R = \frac{16n_o^2 \cdot \sigma_B \cdot T_r^3}{3\mu(T_r)} \qquad \text{in } \frac{W}{m\,K}, \tag{4.6}$$

where n_o is the effective refractive index of the material (for Silica based materials with a high porosity this is approximately 1), σ_B is the Stefan-Boltzmann constant, μ is the temperature dependent extinction coefficient, and T_r the average temperature given in (4.7), for T_i, T_a the inner and outer temperature respectively.

$$T_r = [(T_i^2 + T_a^2)(T_i + T_a)/4]^{1/3} \qquad \text{in K} \qquad (4.7)$$

In order to reduce the radiative heat transfer, a fine coating of carbon, silicium carbide, titanium dioxide or iron oxide can be used [28].

Coupling Effects

The coupling effect arises from the increased heat transport bridging between neighboring particles or fibers on the micro-scale and increases as the heat conductivity of the gas and solid increases [28].

For macroscopic thermal evaluations when $p_f < p_{1/2}$, the coupling term is considered negligible due to the relatively large mean free path of the molecules [28]. $p_{1/2}$ is the fluid pressure at half of the full gaseous thermal conductivity. Since the geometry of the media is fully resolved, including the local pore thermal conductivity, the coupling term is not considered directly in this work. For system pressures above $p_{1/2}$ this may lead to underestimation of the ETC through the silica media.
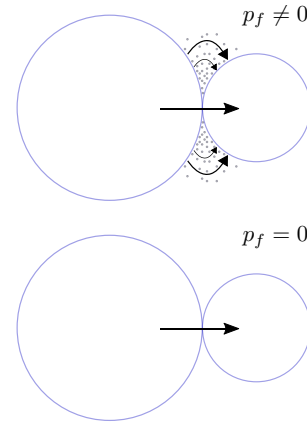
Figure 4.1: *Coupling effect when $p_f \neq 0$ [28].*

4.3.2 Thermal conductivity with lattice Boltzmann methods

In this work, two lattice Boltzmann algorithms solve the conjugate heat transfer in the particle geometry. As Wang et al. [82] state, LBM is well suited for simulating heat transfer in resolved porous media. Two lattice Boltzmann equations have been combined to solve the conjugate heat transfer through the particle geometry. One lattice is used to solve the diffusion equation for the temperature as described in Section 4.3.2, and a second lattice for radiative transport described in Section 4.3.2. The two lattices are coupled to compute heat flux and effective heat transfer through the

porous media. For the constant temperature and constant light intensity boundaries, the regularized boundary scheme following Latt is adopted [49].

LBM for Energy Equation

To solve the energy equation, the domain is composed $\Omega = \Omega_s \cup \Omega_f$, where Ω_f and Ω_s define the fluid and solid domain respectively, as shown in Figure 4.2. Two diffusion equations for the temperature T are solved following Wang's method for conjugate heat transfer [83].

$$\rho_f c_{p\_f} \frac{\partial T}{\partial t} = \lambda_f \nabla^2 T \quad \text{in} \quad \Omega_f, \tag{4.8}$$

$$\rho_s c_{p\_s} \frac{\partial T}{\partial t} = \lambda_s \nabla^2 T \quad \text{in} \quad \Omega_s, \tag{4.9}$$

where ρ is the density and the indices f and s denote the fluid (air) and solid material (silica), respectively, t is the discrete time and λ the thermal conductivity.
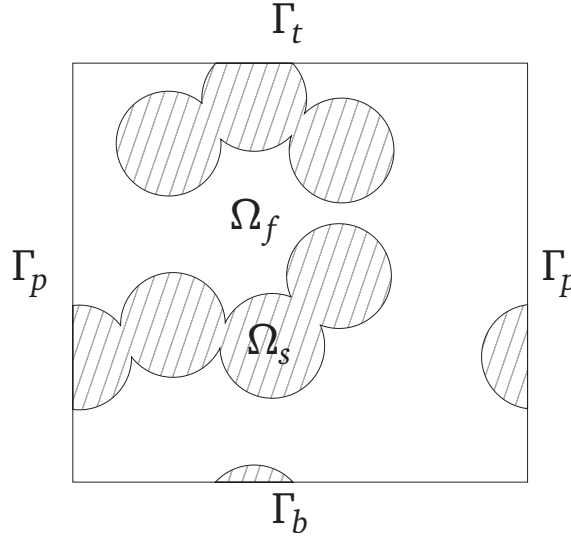
Figure 4.2: *The two domains for LBM, Ω_s and Ω_f for the solid and fluid respectively, with periodic boundaries Γ_p with top and bottom temperature boundaries Γ_t and Γ_b [68].*

The diffusion equation is solved via the LBM with

$$f_i(x + \Delta x, t + \Delta t) = f_i - \frac{1}{\tau}(f_i - f_i^{eq}), \tag{4.10}$$

where f_i is the discrete probability function in discrete direction i, with location x, and grid spacing Δx, as well as time t, with time step width Δt, and τ denotes the relaxation time. The equilibrium function f_i^{eq} is given according to [58].

$$f_i^{eq} = w_i T(x, t),\tag{4.11}$$

where w_i denotes the discrete lattice direction's weights and $T(x, t)$ is the local temperature. A three-dimensional velocity set with seven discrete directions, D3Q7, is used.

The local temperature $T(x, t)$ as well as heat flux $q(x, t)$ are calculated, using the distribution function's moments and discrete velocities c_i, through

$$T(x, t) = \sum_i f_i(x, t) \text{ and } q(x, t) = \frac{\tau - \frac{1}{2}}{\tau} \sum_{i=0}^{6} c_i f_i(x, t).\tag{4.12}$$

The diffusion equation is solved for both the solid and fluid material within a single lattice with respect to different temperature conductivities by using location dependent relaxation times $\tau|_{\Omega_s} = \tau_s$ and $\tau|_{\Omega_f} = \tau_f$. This approach is valid for $\rho_s \cdot c_{p\_s} = \rho_f \cdot c_{p\_f}$ [82]. To meet this condition, the fluid's density in lattice units is chosen as $\rho_f^* = 1$ and the solid's density in lattice units as $\rho_s^* = \rho_f^* \frac{c_{p\_f}}{c_{p\_s}}$ and the position dependent relaxation time given by

$$\tau(x) = \frac{\lambda(x)}{\rho \cdot c_p \cdot c_s^2} + 1/2.\tag{4.13}$$

LBM for radiation transfer equation

Mink et al. [57] have shown to solve the P1-approximation of the Radiative Transfer Equation (RTE) by means of LBM by introducing a mesoscopic sink term. Based on the assumptions related to the P1-approximation (homogeneous participating media, spatially constant scattering and absorption parameters σ_s and σ_a) the RTE can be transformed into the diffusion-reaction equation for light intensity density ϕ

$$\frac{1}{c} \frac{\partial \phi}{\partial t} = \frac{1}{3(\sigma_a + \sigma_s)} \nabla^2 \phi - \sigma_a \phi.\tag{4.14}$$

Here, c denotes the speed of light and the artificial diffusion coefficient D is defined by

$$D(\sigma_a, \sigma_s) = \frac{1}{3(\sigma_a + \sigma_s)}.$$ (4.15)

Mink proposes the lattice Boltzmann equation

$$g_i(x + \Delta x, t + \Delta t) = g_i - \frac{1}{\tau_g}(g_i - g_i^{eq}) - \frac{3\sigma_a(\sigma_a + \sigma_s)}{8} g_i \,,$$ (4.16)

with the discrete probability function g_i, the equilibrium function $g_i^{eq} = w_i\phi$. In contrast to the general transient reaction-diffusion LBM, where the non-dimensional relaxation time τ_g is a function of the diffusivity, this approach allows for τ_g to be set to 1. This is achieved through a suitable target equation which does not depend on the diffusion coefficient, but instead on the absorption and scattering coefficients.

The spatial light intensity is given by the distribution function's zeroth moment

$$\phi(x) = \sum_i g_i.$$ (4.17)

The boundary radiation intensities are chosen following the Stephan Boltzmann law [81] according to the local lattice temperatures by

$$\phi = \left(\frac{T_{(x,t)}}{T_{hot}}\right)^4.$$ (4.18)

The absorption coefficient σ_a is approximated as

$$\sigma_a = 9.2693 \times 10^{-3} \cdot log(P)^2 + 1.3437 \times 10^{-1} \cdot log(P) + 4.7933 \times 10^{-1},$$ (4.19)

interpolating from Alberti et al. [1] and Farag [25], while the scattering coefficient σ_s is estimated as 0.1 for the infrared regime [26].

Conjugate Heat Transfer

Two D3Q7 lattices are combined, one for solving the energy equations as described in Section 4.3.2 and the second for the radiation as described in Section 4.3.2. The infrared intensity distribution is solved and coupled with the temperature through the emissivity, absorption and scattering of the studied media using the radiative transfer

equation by means of LBM. The radiation and conduction are coupled in order to simulate heat transfer for a range of pressures, from 1 bar down to 1 mbar.

The radiation and conduction are currently one way coupled at the upper and lower boundaries [68]. As such, the temperature of the solid domain is used together with the emission/absorption coefficients of the surface to evaluate the radiation from and to these surfaces. For the domain between the upper and lower boundaries, averaged emission/absorption coefficients are used on the basis of a representative elementary volume (REV) [42]. This is due to the radiation wavelength being larger and of a similar order of magnitude as the pore and particle sizes present in the domain.

4.3.3 Calculating effective lambda

As previously mentioned heat transfer through a VIP is composed of the heat transfer through fluid λ_f, through solid λ_S, through radiation λ_R and a coupling term λ_C. The sum of these terms provides the total effective heat transfer λ_ϕ as shown in (4.1). Here, heat conductivity due to the coupling term is negligible due to the relatively large mean free path of the molecules [28].

The effective heat conductivity λ_ϕ though the resolved packing is calculated by

$$\lambda_\phi = \frac{q_\phi L}{\Delta T} \tag{4.20}$$

where L is the cell length, ΔT is the temperature difference between the upper (Γ_t) and lower boundary (Γ_b) and the effective heat flux q_ϕ is given by

$$q_\phi = q_s + q_f + q_r. \tag{4.21}$$

The heat fluxes for the solid q_s and for the fluid q_f are calculated by the temperature distribution's first momentum in (4.12). The heat flux due to radiation q_r is calculated by

$$q_r = \sigma_a(4\sigma_B T^4 - \phi), \tag{4.22}$$

where σ_B is the Stephan-Boltzmann constant.

The particle packing's ETC is examined at the bottom layer of the volume in the simulation. A steady state is assumed to be reached, when the calculated ETC does not change more than 0.01% over the latest 10,000 time steps.

4.3.4 Simulation variables

The simulation input parameters are driven by the microscopic properties of air at low pressures and those of vitrus silica.

Table 4.1: *Solid (silica) and fluid (air) parameters used in effective thermal conductivity studies*

	Parameter	Value	Unit	Source
Silica	c_{p_s}	1052	J/(kg K)	[64]
	λ_s	1.38	W/(m K)	[37, 64]
	ρ_s	2201	kg/m^3	[64]
Air	c_{p_f}	1.007×10^3	J/(kg K)	[81]
	λ_{f0}	26.606×10^{-3}	W/(m K)	[81]
	R_s	287.058	J K/kg	[48]
	p_f	0.01–1	bar	
	β_f	1.63	-	[28]
	σ_f	3.7×10^{-10}	m	[61]
	n_0	2.69×10^{25}	m^{-3}	[38]
	σ_B	$5.670\,367 \times 10^{-8}$	W/m^2/K^4	[81]

As mentioned in Section 4.3.1, at sub-atmospheric pressures, the heat transfer through a fluid is given by(4.4) As the pressure inside the VIP decreases, the heat transfer through the fluid decreases inversely proportional to the Knudsen number in (4.3) [28, 81]. where the characteristic length Φ, is defined in this work as the pore size (maximum inscribed sphere fitting within a pore, see Section 3.3.6) of the silica geometry and l_f is the mean free path given by

$$l_f = \frac{1}{\sqrt{2}\pi\sigma_f^2 n} \qquad \text{in m.} \qquad (4.23)$$

with n being the molecular number density, or number of molecules per volume $\frac{N}{V}$m^{-3}. The molecular diameter of air is $\sigma_f = 3.7 \times 10^{-10}$ m.

An example calculation for the mean free path at 0.6 bar by evaluating the molecular number density via the ideal gas law ($\frac{n_1}{n_0} = \frac{p_{f,1}}{p_{f,0}} \rightarrow n_1 = \frac{p_{f,1} * n_0}{p_{f,0}}$) follows

$$n_1 = \frac{0.6[bar] * 2.69 \cdot 10^{25}[m^{-3}]}{1[bar]} = 1.614 \times 10^{25} \qquad \text{in m}^{-3}. \qquad (4.24)$$

The mean free path is then

$$
\begin{aligned}
l_f &= \frac{1}{\sqrt{2}\pi\sigma_f^2 n_1} \\
&= \frac{1}{\sqrt{2}\pi(3.7 \cdot 10^{-10}[m])^2 \cdot 1.614 \cdot 10^{25}[m^{-3}]} = 1.0187 \times 10^{-7} \qquad \text{in m}
\end{aligned}
\tag{4.25}
$$

or 101.866 nm.

An initial estimate for the average pore size δ is given by (4.26) from the VDI Heat Atlas [81]. Where d_p is the primary particle diameter and Π the porosity of the silica.

$$
\delta = \frac{2}{3} \cdot d_p \cdot \frac{\Pi}{(1 - \Pi)} \qquad\qquad \text{in m.} \tag{4.26}
$$

Using (4.23) and (4.3) the Knudsen range of the system for various pressures can be evaluated. A pressure of 600 mbar and a pore size (characteristic length) of 200 nm results in a Knudsen number of 0.5; a pressure of 100 mbar and pore size of 200 nm: Kn = 3; and a pressure of 500 mbar and pore size of 100 nm: Kn=1.2. The range of Knudsen numbers of interest in the VIP media is then in the range of $10^{-1} \leq Kn \leq 10^1$ or the transition regime. This would necessitate the need for slip and partial slip boundaries, however, free convection can be neglected when the pore size is smaller than 3 mm [33], as is the case for the VIP media.

The density of the air, ρ_f, is calculated from the ideal gas law,

$$
\rho_f = \frac{p_f}{(R_s \cdot \overline{T})} \qquad\qquad \text{in kg/m}^3 \tag{4.27}
$$

where p_f is the system pressure, R_s the specific gas constant (287.058 J/(kg K) [81]) and the average system temperature $\overline{T}$ is 305.65 K.

4.3.5 Lattice Boltzmann Modeling for the Transition Regime

A review of fluid-solid interactions was written by Cao et al. [13], where the dependence of the slip length on various physical factors is discussed. These factors include: liquid polarity, viscosity, temperature, pressure, surface wettability, surface roughness, shear rate, and the presence of nano-bubbles or gas films.

To calculate the wall velocities the normal direction at the boundary is required [13, 34, 52]. For this purpose, continuous normal implementations were developed for two and three dimensions. These implementations are described here and the code implementation is available in "https://gitlab.com/jesserj/heattransfernanosilica/".

Continuous Normals in Two Dimensions

This section describes the algorithm for estimating the continuous normal for a two dimensional polygon. Two input parameters are required, the starting coordinate $origin$ of interest and a direction vector $direction$ in which to search for the normal vector.

The working concept is to identify two points residing on the surface of the polygon both equidistant from the $origin$ given (in the given $direction$). These two points define a tangent line on the polygon from which the the normal vector is defined.

The first step defines $precision$ which is the cut off criteria for the search algorithm. Following, a check is made to find out if $origin$ is inside or outside the object and this Boolean value is stored ($originValue$). Next, the distance from the given point ($origin$) in the given direction ($direction$) to the object surface is calculated ($dist$). The intersection of the direction vector with the object surface, provides the 'point on surface' (POS), with is defined using the distance to the surface (from $origin$) and the unit vector of direction ($direction$); this is given by: $POS = origin + direction \cdot dist$.

The next step then iterates twice, once rotating anticlockwise then once clockwise to find two points on the object surface, using a form of binary search. Starting at an angle of $-90°$ (or $90°$ for the second iteration), $direction$ is rotated. The algorithm iteratively rotates the point 'towards' and/or 'away' successively, reducing the $pitch$ (change in angle of rotation) by half, until the angle of rotation becomes smaller than the $precision$ defined. The search range is between $1°$ and $179°$. For each rotation, a check is made to see if $currentPoint$ is inside the object: $if (currentValue == originValue)$ then rotate 'away,' otherwise rotate 'towards' the origin. This is accomplished by either adding or subtracting the current $pitch$ to the previous angle of rotation. Following each iteration the $pitch$ is divided by two.

As mentioned, the loop ends when the $pitch$ is smaller than the $precision$ defined. This is then an indication that $currentPoint$ is as close to the surface as defined by $precision$. For each of the angles $-90°$ and $90°$, the $currentPoint$ from each iteration is stored in $point1$, and $point2$ respectively. These two points lie on (or very close to)

the surface of the object and define a tangent line. The normal direction from the objects surface is $normal = [(point2(2) - point1(2)), -(point2(1) - point1(1))]$. A visual demonstration of the algorithm is shown later in Figure 4.5.

Continuous Normals in Three Dimensions

This section describes the algorithm for estimating the continuous normal for a three dimensional surface. The algorithm described here operates similarly to the estimation of the two dimensional normal presented in Section 4.3.5. Two input parameters are required, a starting coordinate $origin$, and a direction vector $direction$, to search.

The working concept is to identify three points residing on the surface of the object all equidistant from the $origin$ defined (in the given $direction$). These three points define a tangent plane from which the normal vector at this point on the object's surface is defined.

The first step defines $precision$ which is the cut off criteria for the search algorithm. Following, a check is made to find out if $origin$ is inside or outside the object and this Boolean value is stored ($originValue$). Next, the distance from the given point ($origin$) in the given direction ($direction$) to the object surface is calculated ($dist$). The intersection of the direction vector with the object surface, provides the 'point on surface' (POS), with is defined using the distance to the surface (from $origin$) and the unit vector of direction ($directionN$), this is given by: $POS = origin + directionN \cdot dist$.

The following step calculates $directionPerp$, a vector orthogonal to $directionN$, as well as its unit vector $directionPerpN$. An important adjustment to ensure that the search algorithm scales with the provided geometry, was made to scale $directionN$ by the magnitude of the given direction vector. In this way, different applications of the algorithm are able to control how large the search vectors are depending on the geometry.

With each of these vectors and coordinates defined, the vector $directionPerpN$ is rotated around the direction vector through the angles $theta$: 0°, 120° and 240°. The algorithm for rotation of a vector around an axis of rotation defined by a second vector is given by the Rodrigues rotation [6], with the implementation provided in Source Code 4.1. For each angle $theta$, an orthogonal vector ($directionPerpN$) is rotated around $directionN$ and the coordinates at the tip of this vector are calculated as: $perpPoint = POS + perp$.

```
1  template <typename S>
2  bool IndicatorF3D<S>::rotOnAxis(Vector<S,3>& vec_rot, const
       Vector<S,3>& vec, const Vector<S,3>& axis, S& theta)
3  {
4    vec_rot = vec ;
5    Vector<S,3> crossProd;
6    crossProd[0] = axisN[1]*vec[2] - axisN[2]*vec[1];
7    crossProd[1] = axisN[2]*vec[0] - axisN[0]*vec[2];
8    crossProd[2] = axisN[0]*vec[1] - axisN[1]*vec[0];
9
10   S dotProd = axisN[0]*vec[0] + axisN[1]*vec[1] + axisN[2]*vec
       [2];
11   vec_rot = std::cos(theta)*vec + (crossProd)*std::sin(theta)
       + axisN*(dotProd)*(1 - std::cos(theta));
12
13   return true;
14 }
```

Source Code 4.1: *Rodrigues rotation [6]*

A new axis of rotation *rotAxis* is defined by evaluating the cross product of *perp* and *directionN*, and is used to rotate *perpPoint* around *POS* in a binary search pattern. To determine which direction is 'towards' or 'away' from the *origin*, a *testPoint* is used, where $testPoint = perpPoint$ rotated 45° around *rotAxis*. If the distance between *testPoint* and the *origin* ($|testPoint - origin|$) is less than the distance between *perpPoint* and the *origin* ($|perpPoint - origin|$) then a positive angle rotates 'towards' the *origin*; otherwise it rotates 'away'.

The algorithm then iteratively rotates the point 'towards' and/or 'away' successively, reducing the *pitch* angle of rotation by half, until *pitch* becomes smaller than the *precision* defined. The search range is between 1° and 179°. For each rotation, a check is made to see if *currentPoint* is inside the object, $if (currentValue == originValue)$ then it rotates 'away;' otherwise it is to rotate 'towards' the origin. Following each iteration the *pitch* is divided by two.

As mentioned, the loop ends when the *pitch* is smaller than the *precision* defined. This is then an indication that the *currentPoint* is as close to the surface as defined by *precision*. For each of the angles 0°, 120° and 240°, the *currentPoint* from each iteration is stored in *point*1, *point*2, and *point*3, respectively. These three points lie on (or very close to) the surface of the object and define a tangent plane. The normal direction from the objects surface is the cross product of the two vectors $[point1 - point2]$ and $[point1 - point3]$.

4.4 Validation

Using the proposed methods, several simulation setups were generated to evaluate the reliability and accuracy of the approach. The first study presented is a grid independence study used to confirm convergence of the model, in Section 4.4.1. Thereafter, the two and three dimensional normals are evaluated in Section 4.4.2 and Section 4.4.3 respectively. Lastly, the results of a slip boundary test case are presented in Section 4.4.4.

4.4.1 Grid independence

To confirm grid independence, a simplified geometry, shown in Figure 4.3, the consideration of a single sphere between two plates is used to evaluate the ETC. The top boundary (Γ_t) is held at a constant temperature of 306.15 K, and the bottom boundary (Γ_b) 305.15 K. The remaining 4 boundaries are periodic. The radiation intensity is calculated using the local lattice temperature and (4.18). The resolution of the simulation, N, is defined as the number of grid cells used to resolve the diameter of the sphere. Two convergence studies are conducted, corresponding to before and after the implementation of the local distance field. N is increased with the following steps 4, 8, 16, 32, 64 in the first study and additionally 128 in the second, with diffusive scaling and $\tau_f = 0.9$. In lieu of an analytical solution a simulation with resolution 128 (256) is used to calculate the relative error by

$$\epsilon_\phi(N) = \frac{\lambda_\phi(N) - \lambda_\phi(N_{max})}{\lambda_\phi(N_{max})} \tag{4.28}$$

where ϕ is the ETC of air, solid or radiation and ϵ the relative error. The relative error versus the system resolution is shown in Figure 4.4.

4.4.2 Validation of Two Dimensional Normal

A validation test case was developed to evaluate the error of the two dimensional normal estimation. The error is calculated by finding the difference between the estimated normal and the known normal for a point on a circle. Defining a circle (with *radius* and *center*), any *origin* (within the circle) and *direction* provided to the two dimensional normal implementation, will result in a normal pointing towards
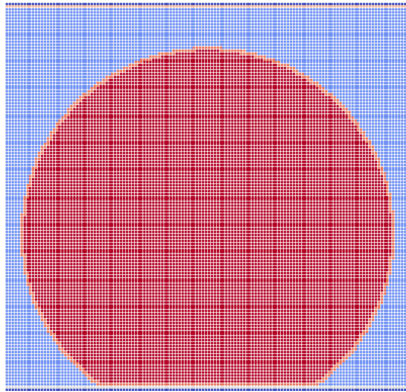
(a) *Two dimensional slice through the geometry*
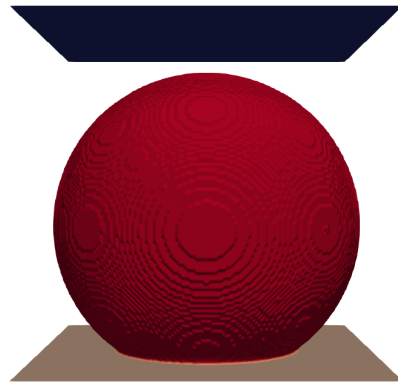
(b) *Three dimensional view of geometry*

Figure 4.3: *Simplified geometry used to calculate experimental order of convergence. Top and bottom boundaries held at constant temperature and the other 4 boundaries are periodic.*
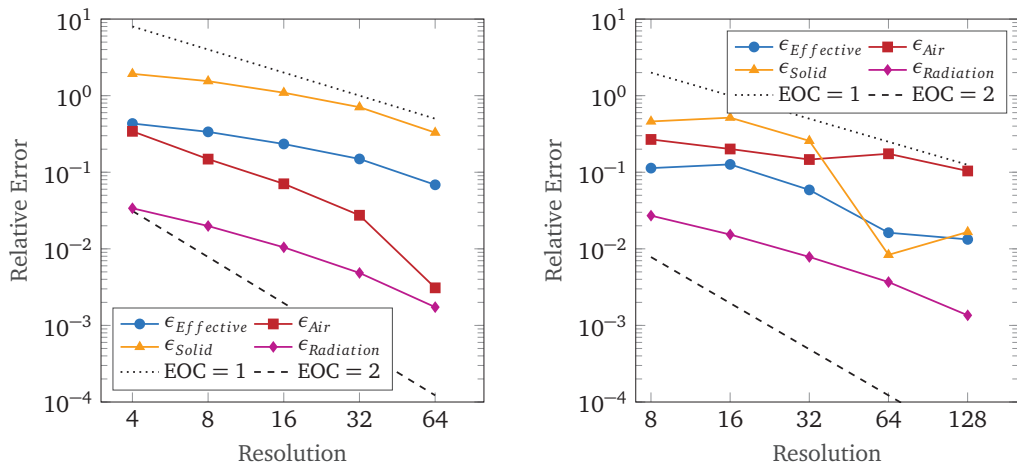
Figure 4.4: *Relative error as a function of simulation resolution.*

the center of the circle. Knowing the radius of the circle, the center of the circle can be re-estimated. The error of the two dimensional normal estimation is calculated as the distance between *center* and the estimated center, as shown in Source Code 4.2.

```
1    // Check error of 2D normal using a circle
2    Vector<S,2> POS; //Point on Surface
3    POS[0] = origin[0] + direction[0]*distance/direction.norm();
4    POS[1] = origin[1] + direction[1]*distance/direction.norm();
5
6    Vector<S,2> normalVec;
7    T norm = radius/normal.norm();
8    normalVec[0] = POS[0]+normal[0]*norm;
9    normalVec[1] = POS[1]+normal[1]*norm;
10
11   clout << "Error = " << (normalVec - center).norm() << endl;
```

Source Code 4.2: *Error calculation of 2D normal*

A visual example of the estimation of the two dimensional normal is shown in Figure 4.5, with the inputs of $direction = \begin{bmatrix} 0.707 \\ 0.707 \end{bmatrix}$ and $origin = \begin{bmatrix} 3 \\ 0 \end{bmatrix}$. Following the algorithm description in Section 4.3.5, the blue point shows the position on the surface POS, each $currentPoint$ is shown in red and the points found to be on the surface $point1$ and $point2$ shown in **black**, with the estimated $normal = \begin{bmatrix} -1.6843 \\ -1.0575 \end{bmatrix}$ shown in orange.
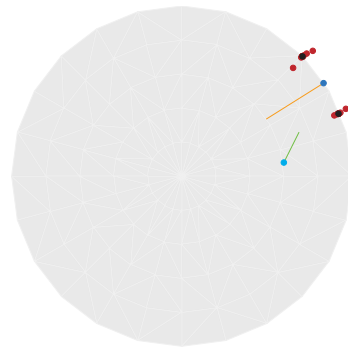
Figure 4.5: *Two dimensional normal implementation*

4.4.3 Validation of Three Dimensional Normal

Two validation test cases were developed to calculate the error of the three dimensional normal estimation. The error is calculated by finding the difference between the estimated normal and the known normal for a point on a sphere. The first case defines a sphere (with $radius$ and $center$). Any $origin$ (within the sphere) and $direction$ provided as inputs will result in a normal pointing towards the center of the sphere. Knowing the radius of the sphere, the center of the sphere can be re-estimated. The error of the three dimensional normal estimation is calculated as the distance between $center$ and the estimated center, as shown in Source Code 4.3.

```
1   // Check error of 3D normal using a sphere
2   Vector<S,3> POS; //Point on Surface
3   POS[0] = origin[0] + direction[0]*distance/direction.norm();
4   POS[1] = origin[1] + direction[1]*distance/direction.norm();
5   POS[2] = origin[2] + direction[2]*distance/direction.norm();
6
7   T normDir = sqrt(direction[0]*direction[0] + direction[1]*
        direction[1] + direction[2]*direction[2]);
8
9   Vector<S,3> normalVec;
10  T norm = radius/normal.norm();
11  normalVec[0] = POS[0]+normal[0]*norm;
12  normalVec[1] = POS[1]+normal[1]*norm;
13  normalVec[2] = POS[2]+normal[2]*norm;
14
15  clout << "normalVec = " << normalVec[0] << "=" << POS[0] <<
        "+" << normal[0] << "*" << norm << endl;
16  clout << "Error = " << (normalVec - center).norm() << endl;
```

Source Code 4.3: *Error calculation of 3D normal with a sphere*

A second test case uses a cylinder to validate the three dimensional normal estimation. This case was required to validate that the modification of the input direction magnitude properly adjusts the search radius. In this case, the normal may be emitted by the top or bottom circular plane surface, or from the curved surface. As such, the test case is split in two as shown in Source Code 4.4. The cylinder is defined by two center coordinates ($center1$ and $center2$) of the top and bottom surface as well as a $radius$. A correctly estimated normal then either points vertically, or if emitted by the curved surface points towards the center of the cylinder. Similar to the spherical case, the error is calculated as the distance between the known cylinder center and the estimated center.

```
1   // Check error of 3D normal using a cylinder (2 cases, top/
        bottom or side surface)
2   if(std::abs(normal[0]) <= 1e-06 && std::abs(normal[1]) <= 1e
        -06){
3     clout << "Top/bottom surface: " << endl;
4       clout << "normal = [" << normal[0] << "," << normal[1]
            << "," << normal[2] << "]" << endl;
5   }
6   else{
7       clout << "Side surface: " << endl;
```

```
8        clout << "normal = [" << normal[0] << "," << normal[1]
             << "," << normal[2] << "]" << endl;

10       Vector<S,3> POS; //Point on Surface
11       POS[0] = origin[0] + direction[0]*distance/direction.
             norm();
12       POS[1] = origin[1] + direction[1]*distance/direction.
             norm();
13       POS[2] = origin[2] + direction[2]*distance/direction.
             norm();

15       Vector<S,3> normalVec;
16       T norm = radius/normal.norm();
17       normalVec[0] = POS[0]+normal[0]*norm;
18       normalVec[1] = POS[1]+normal[1]*norm;
19       normalVec[2] = POS[2]+normal[2]*norm;

21       Vector<S,3> newCenter;
22       newCenter[0] = center1[0];
23       newCenter[1] = center1[1];
24       newCenter[2] = center1[2]+POS[2];

26       clout << "POS = " << POS[0] << "," << POS[1] << "," <<
             POS[2] << endl;
27       clout << "center point cylinder  = [" << newCenter[0] <<
             "," << newCenter[1] << "," << newCenter[2] << "]"
             << endl;
28       clout << "predicted center point = [" << normalVec[0] <<
             "," << normalVec[1] << "," << normalVec[2] << "]"
             << endl;

30       clout << "Error = " << (normalVec - newCenter).norm()/
             radius << endl;
31   }
```

Source Code 4.4: *Error calculation of 3D normal with a cylinder*

4.4.4 Slip boundary Test Case

To evaluate implementations of off-axis slip boundary conditions in *OpenLB*, a test case was developed and the code repository is described in the Appendix Section D. Using the preliminary slip boundary conditions which have been implemented, the test case was used to simulate fluid flow inside a two dimensional inclined channel which can be rotated to any angle.

(a) 2D Channel 0°

(b) 2D Channel 10°

(c) 2D Channel 30°

(d) 2D Channel 45°
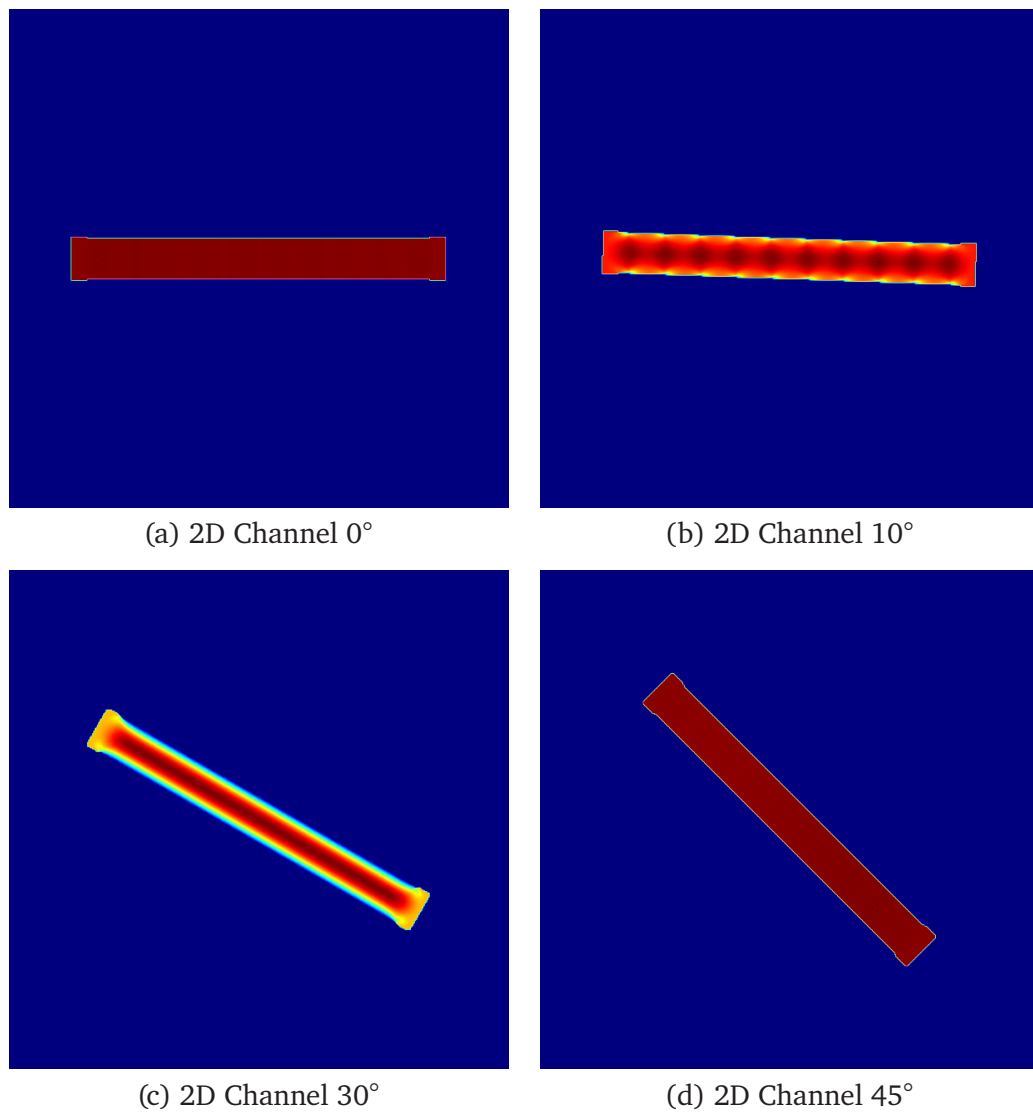
Figure 4.6: *Slip boundary conditions simulation results, velocity profile.*

The resulting velocity profiles are displayed in Figure 4.6. The slip boundary conditions work well for on-axis boundaries, such as 0° as well as for 45°. This is evident from the homogeneous velocity across the width of the cylinder. In the case of acute angles however, due to the discretization, velocity jumps are visible. Furthermore, as can be seen in Figure 4.6, a channel flow develops fully for angles of approximately 30°.

4.5 Discussion and Outlook

In this chapter the heat transfer methods through porous materials were presented, followed by the LBM implementations to solve the energy and radiation transfer equations. These implementations were tested for mesh sensitivity and the Error of Convergence (EOC) was evaluated. Thereafter, two algorithms were presented to estimate the two and three dimensional normals for continuous surfaces, alongside a test case for evaluation of two dimensional slip boundary implementations.

In the first EOC study, thermal conductivity through air and due to radiation have a superlinear experimental order of convergence. In the second study using the local distance field, the thermal conductivity due to radiation and through the solid have an approximately linear experimental order of convergence. The thermal conductivity through the air is likely sublinear due to the abundance of curved boundaries.

The two and three dimensional normal algorithms were validated by calculating the normal vectors for geometries with analytical normals. Although both of the normal implementations show satisfactory results, improvements can be made to both algorithms. The search pattern converges in the same number of time steps. A suggested improvement is to evaluate the distance of the $currentPoint$ from the surface after each rotation of $direction$. Using the distance to the surface, a more sophisticated update to the rotation angle may be made in a single iteration, reducing the number of Rodrigues rotations calculated. However, this may only be slightly faster since the simultaneous distance calculation is also iterative. The slip boundary test case showed that the current implementation of slip boundary conditions works as expected for on-axis boundaries as well as boundaries at 45°. For off-axis boundaries however, fluctuations in velocity are evident. New implementations of slip boundaries can now be tested in *OpenLB* using the continuous normal in two and three dimensions.

4.6 Conclusion

The primary goal of this chapter was to develop a methodology to numerically estimate effective heat transfer through the geometry which was generated in Chapter 3. The methodology presented is able to numerically estimate heat transfer due to radiation and conduction through both the nano-porous silica particles and fluid air over a range of pressures, 0.01 bar to 1 bar. Further, the secondary goal of this chapter was to develop several geometric tools helpful in the development of slip boundary conditions for rarefied fluid flow simulations. These tools included continuous normal calculation in two and three dimensions and accompanying test case validation algorithms.

5

Application and Validation

It doesn't matter how beautiful your theory is, it doesn't matter how smart you are. If it doesn't agree with experiment, it's wrong.

Richard Feynman

5.1 Aims and Overview

The goal of this chapter is to numerically evaluate the Effective Thermal Conductivity (ETC) through silica Vacuum Insulation Panels (VIPs) media using the geometry and the Lattice Boltzmann Methods (LBMs) described in Chapter 3 and Chapter 4 respectively. The ETC should match measured and literature values for silica VIP media over a range of system pressures from 0.1 bar to 1 bar.

This chapter is organized as follows. The motivation is presented in Section 5.2. Methods are presented in Section 5.3, including a description of the ETC measurement system in Section 5.3.1 and an estimation of the measurement uncertainty in Section 5.3.2. The results of the ETC studies are presented in Section 5.4, with the evaluation of a globally defined pore size in Section 5.4.1, a comparison to literature values in Section 5.4.2, the effects of compression on the ETC in Section 5.4.3, and then followed by the results evaluating the ETC with a locally defined pore size and their comparison to literature and measured values in Section 5.4.4. Lastly, a discussion and outlook are presented in Section 5.5 and conclusion in Section 5.6.

The results presented in this chapter have been developed in collaboration with Sebastian Sonnick and Maximilian Gaedtke. VIP measurements were performed by Sebastian Sonnick, visualizations were performed by Maximilian Gaedtke and Jesse Ross-Jones. The result analysis and evaluation was performed by Jesse Ross-Jones. These results have also been previously published in *Conjugate heat transfer through nano scale porous media to optimize vacuum insulation panels with lattice Boltzmann methods* [68] and *Pore-Scale Conjugate Heat Transfer Simulations Using Lattice Boltzmann Methods for Industrial Applications* [70].

5.2 Motivation

By generating a single holistic tool which can be used to generate silica geometry, and then automatically simulate the thermal conductivity through the generated geometry, an in depth understanding of the effects of particle geometry and heat transfer in VIPs is obtained. By simulating over a range of decreasing internal pressures, the minimum pressure required for a low effective heat transfer, which yields both an improvement in the lifetime and reduction of the manufacturing costs of VIPs, can be determined.

5.3 Methods

The measurement methodology for evaluation of the ETC of VIP media is presented in Section 5.3.1. This is followed by an estimation of the measurement uncertainty of the measurement system in Section 5.3.2. The methodologies for geometry generation and subsequent numerical heat transfer evaluation were previously presented in Chapter 3 and Chapter 4 and are not repeated here.

5.3.1 Thermal conductivity measurements

In order to measure the thermal conductivity of the VIPs, two measurement systems were constructed. The first measurement system described here, is composed of a wooden box filled with mineral wool to minimize heat losses. The VIP is placed between two heating plates underneath and a cooling plate on-top as shown in Figure 5.2, and is constructed with two openings, one for connection to a vacuum pump through a solenoid valve, and the second for attachment of a Pirani pressure sensor. A vacuum pump and sensor are used in combination to regulate the pressure in the panel as shown in Figures 5.1 and 5.2. The attached vacuum pump is able to achieve a pressure of 10^{-4} mbar.
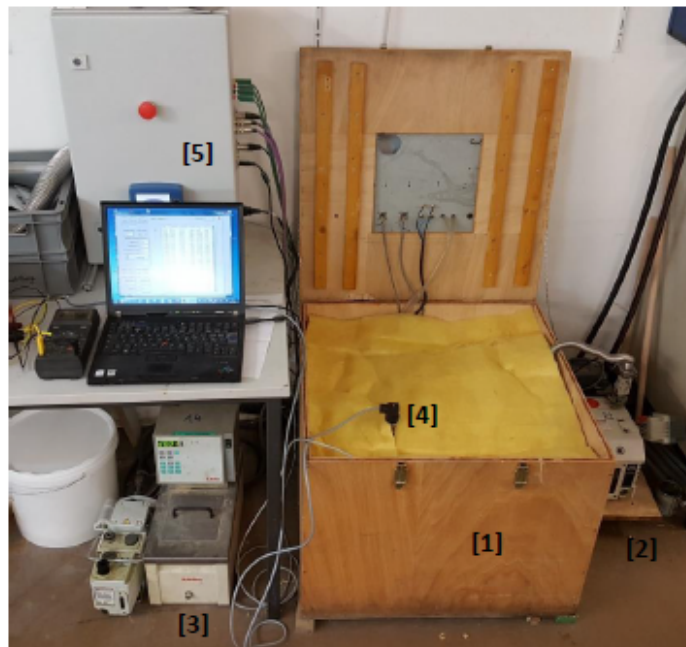
Figure 5.1: *Thermal conductivity measurement system composed of: [1] insulated enclosure, [2] vacuum pump, [3] thermostat, [4] pressure sensor, [5] measurement electronics and laptop.*

To measure the thermal conductivity of a panel, the cooling plate is held at a constant temperature of 20 °C while the top hot plate maintains 40 °C. A second hot plate, placed underneath the first, is used to make up for heat losses through the bottom of the measurement system. The power required to maintain the hot plate temperature is recorded. Once the result reaches a stable level for 750 seconds, the pressure in the
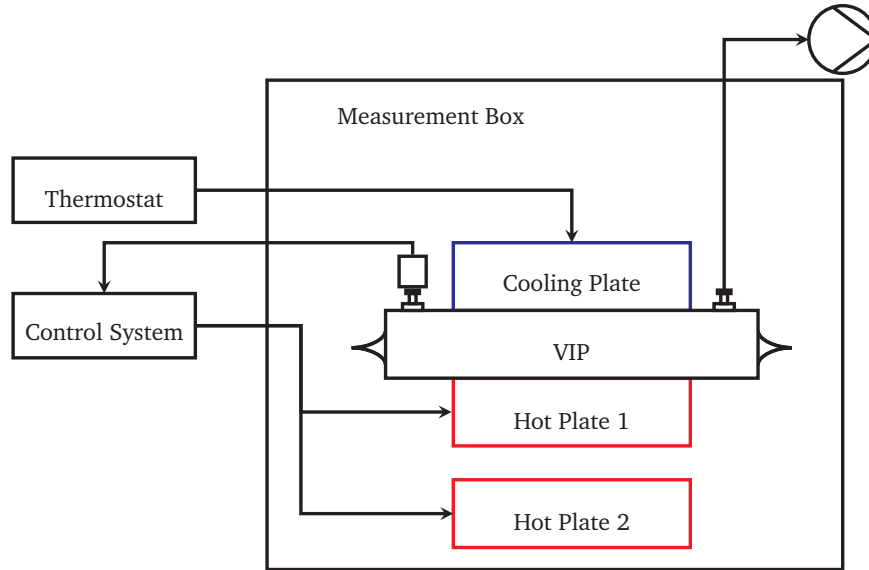
Figure 5.2: *Schematic diagram of measurement system. The power required to maintain the top hot plate at 40 °C is proportional to the effective thermal conductivity.*

panel is reduced and a new measurement begins. The ETC λ_ϕ is measured according to

$$\lambda_\phi = \frac{(\dot{Q}_M - \dot{Q}_L) \cdot d_{VIP}}{A \cdot (\overline{T}_{cold} - \overline{T}_{hot})} \qquad \text{in } \frac{W}{m\,K}. \tag{5.1}$$

where $\dot{Q}_M$ is the measured power needed to maintain the top hot plate at 313,15 K (40 °C), $\dot{Q}_L$ the measured power losses, d_{VIP} the thickness of the panel, A the area of the panel being measured, $\overline{T}_{cold}$ is 293,15 K (20 °C) and $\overline{T}_{hot}$ is 313,15 K (40 °C).

In order to prepare the sample plate composed of precipitated silica to be tested, the silica is first homogenized in a blender. This step reduces large clumps and produces a sample of consistent thickness. A 50 t hydraulic press and stamp are then used to compress the silica with a predetermined pressure. The pressed silica plate is then placed in a drying oven at 100 °C to remove residual moisture, following which it is then placed within an aluminum moisture diffusion barrier surrounded by a fleece fabric and sealed with a vacuum sealer. Fleece material is used to minimize the amount of powder escaping the form during the vacuum and to aid in distribution of pressure applied within the panel. The panel's thickness is measured at several points using the average thickness to calculate the ETC.

To determine undesired heat flux loss to the environment or through the foil surrounding the core material, the thermal conductivity of a known standard material is measured before each measurement. For this purpose a standard polystyrene board from National Institute of Standards and Technology (NIST) is used. To calculate thermal conductivity as a function of temperature and density in (5.2) from Zarr et al. [85] holds.

$$\lambda_{standard} = 0.00111 - 0.0000424 \cdot \rho + 0.000115 \cdot T \pm 1.5\% \qquad \text{in } \frac{\text{W}}{\text{m K}} \qquad (5.2)$$

To evaluate heat losses, the standard plate is measured under the same conditions as the sample, including foil type, dimensions and temperatures of cooling and heating. The expected heat flux can then be calculated with

$$\dot{Q}_{exp} = \frac{\lambda_{standard}}{d_{VIP}} \cdot A \cdot \Delta T \qquad \text{in W} \qquad (5.3)$$

The heat losses into the environment and through the foil can then be determined by subtracting the expected heat flux, $\dot{Q}_{exp}$, from the measured heat flux

$$\dot{Q}_L = \dot{Q}_M - \dot{Q}_{exp} \qquad \text{in W} \qquad (5.4)$$

5.3.2 Measurement Uncertainty

Calculating the propagation of uncertainty using Tables 5.1 and 5.2, together with the uncertainty for the thickness and area of the VIP, 5 % and 1 % respectively, in (5.1), a total uncertainty of 8.73 % for the thermal conductivity measurement is obtained.

Table 5.1: *Measurement uncertainty for temperature sensors.*

Sensor	Type	Error
Thermocouple	PT100	± 0.270K
Transducer	MU-PT100-I420	0.100 %
NIDAQ	USB.6008	0.153 %
	Total Error	0.200 %

Two pressure sensors are used, a Pirani sensor and a Siemens SITRANS P200 capacitive sensor to measure at low and high pressures respectively. The capacitive sensor has a

Table 5.2: *Measurement uncertainty for power sensor.*

Sensor	Type	Error
Power	Shunt Resistor	1.000 %
NIDAQ	USB.6008	0.147 %
	Total Error	1.010 %

maximum uncertainty of 0.5 %, whereas the Pirani sensor is used between 0.01 and 10 mbar and has a maximum uncertainty of 15 %.

5.4 Results

Two heat transfer studies were conducted using numerically generated precipitated silica media. The initial study uses a globally defined pore size, whereas in the subsequent study the local pore size and local Knudsen number is evaluated. Both studies numerically simulate the effective heat transfer through the three-dimensional packing of silica particles, with the top (Γ_t) and bottom (Γ_b) boundaries held at constant temperatures, 306.15 K and 305.15 K respectively. The remaining four boundaries being periodic. ETC is composed of two heat transfer components, conduction through the solid and gas as well as radiation.

The results of the initial study are presented first, whereby a breakdown of the ETC is described in Section 5.4.1, followed by a comparison to literature values in Section 5.4.2, and lastly, the effects of compression on the aggregate geometry and comparison to measurements in Section 5.4.3. Thereafter, the results of the subsequent study, incorporating the implementation of a locally defined pore size, are presented in Section 5.4.4.

5.4.1 ETC with a globally defined pore size

To evaluate the ETC of the silica geometry, the top boundary (Γ_t) was held at a constant temperature of 306.15 K, and the bottom boundary (Γ_b) at 305.15 K, the remaining 4 boundaries being periodic. The ETC is calculated as described in Section 4.3.3 and the resolution of the simulation applied, N, is 16.

Figure 5.3 shows the thermal conductivity breakdown as a function of the system pressure, being composed of the thermal conductivity through the air and solid, as
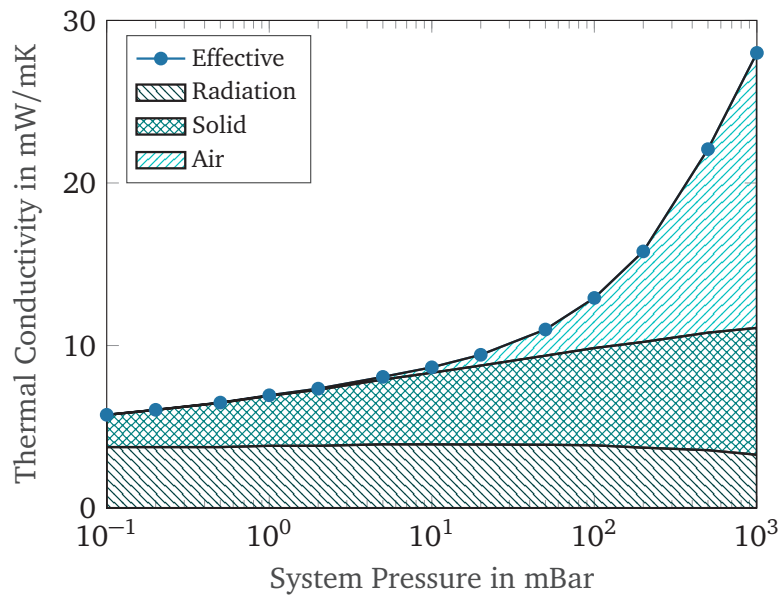
Figure 5.3: *Thermal conductivity breakdown of due to air, radiation and through the solid material.*

well as radiation. As the system pressure decreases, the thermal conductivity of the air clearly decreases. Below 50 mbar the thermal conductivity of air ceases to have a significant effect. The radiation and temperature distributions in the geometry can be seen in Figures 5.4 and 5.5 respectively.

The thermal transfer due to radiation remains relatively constant as the system pressure decreases. At higher pressures, the density of air particles increases and thus absorption of radiation increased reducing the heat flux due to radiation slightly.

Likewise, the thermal conductivity through the solid decreases following the decrease in system pressure. While this should not be the case at very low pressures, at higher pressures, this essentially creates the coupling effect observed between particles. This is due to the air providing the heat flow a second parallel path, therby increasing the heat contribution through the solid. Since the estimation of pore size, and consequently the mean free path, of the system is defined globally, these supposed heat flow paths of least resistance between particles appear to exist even at low pressures. This is a shortcoming of using a globally defined pore size. The solution for this is to calculate the pore size for every lattice unit permitting evaluation of the thermal conductivity per lattice.
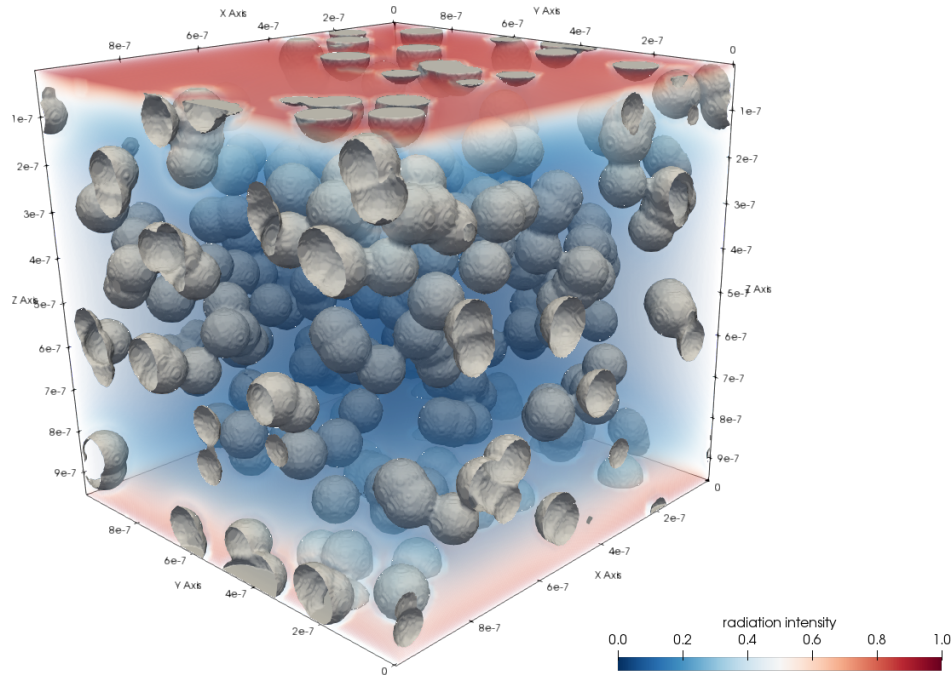
Figure 5.4: *Radiation distribution through periodic packing of silica aggregates.*

5.4.2 Comparing ETC with literature values

Figure 5.6 presents a comparison of the simulations results and literature values obtained from Fricke et al. [28] for heat conductivity of silica over various pressures. Similar to the previous case, the top boundary (Γ_t) is held at a constant temperature of 306.15 K, and the bottom boundary (Γ_b) at 305.15 K. The other 4 boundaries are periodic. The ETC is calculated as described in Section 4.3.3 and the resolution of the simulation, N, is 16.

Literature values show that a constant thermal conductivity is reached below 10 mbar, whereas the thermal conductivity in the simulation continues to decrease slowly. As previously mentioned this is due to the solid conductivity and a global pore size and mean free path. In order to obtain improved accuracy at low air pressures, the local pore size of each lattice unit will be calculated and therefore define a thermal conductivity per lattice. The average relative error between the simulated and reference values is 6.12 %. Good agreement is obtained at ambient pressures, with a relative error of 1.54 %, increasing to 47.22 % at 0.1 bar.
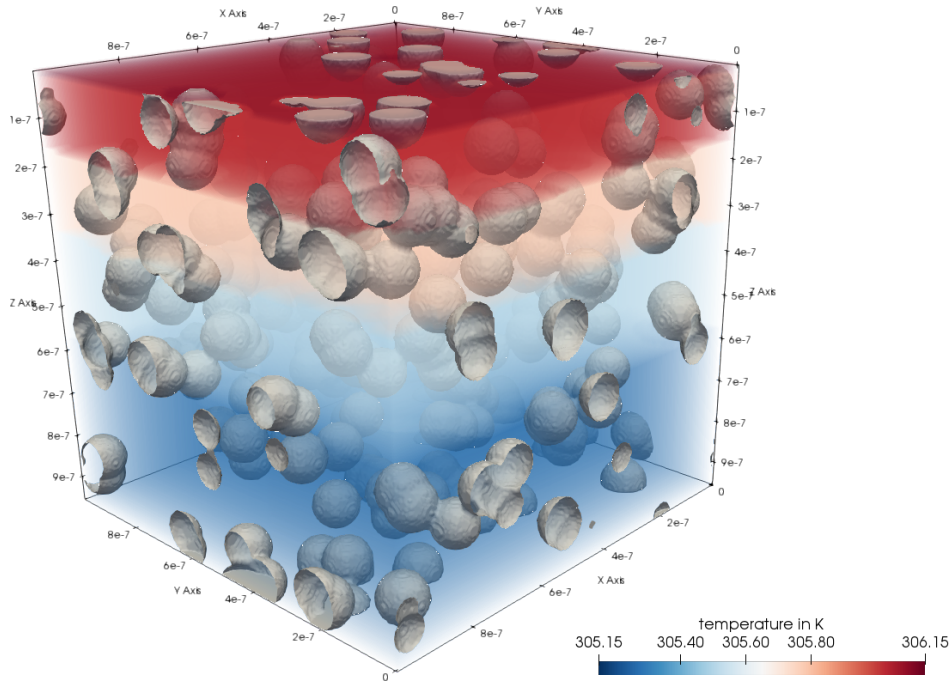
Figure 5.5: *Temperature distribution through periodic packing of silica aggregates.*

5.4.3 Effect of compression on ETC

In order to investigate the effect of different compression forces on the thermal conductivity of the VIPs, several panels were compressed within a range of pressures, and their thermal conductivity measured. The results of compressing the panels applying 15, 20, 25 and 30 bar are shown in Figure 5.7a.

As the compression force increases, the thermal conductivity through the panel decreases. One explanation for this phenomenon is that the pore size decreases with increasing compression force. Therefore, as discussed in Section 5.4.1 the Knudsen number decreases and as a result the thermal conductivity through the air also decreases.

In order to see if a similar effect would be observed in the numerical simulations, various geometries were generated with varying degrees of compression. The porosity and average pore size was calculated for each geometry and then used to simulate the heat transfer through the generated geometry in *OpenLB*. The results are shown
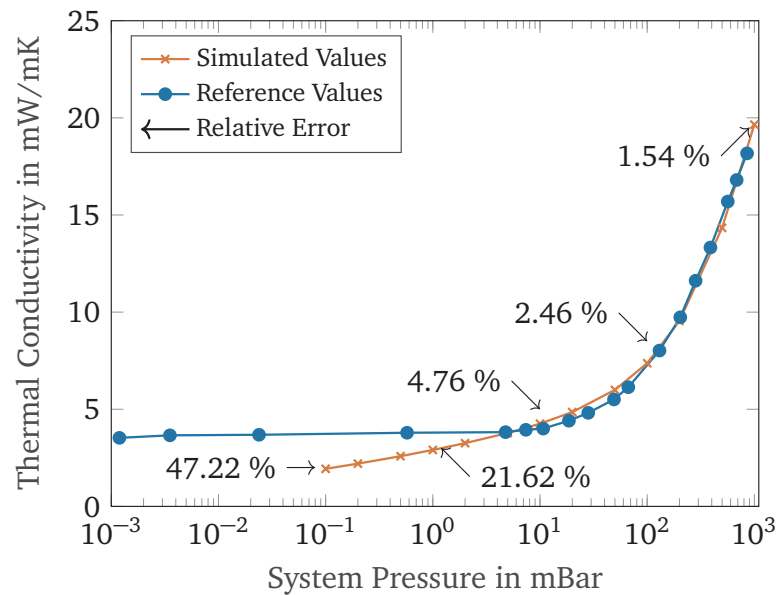
Figure 5.6: *Comparison of effective thermal conductivity to reference values [28]. Simulated effective thermal conductivity decreases at low pressures due to solid conductivity being influenced by the globally defined mean free path.*

in Figure 5.7b, where the compression level is proportional to the number of iterations applied to compress the particle geometry.

A similar tendency to that which was observed in the measurements is revealed; the thermal conductivity decreases as the particle geometry is compressed. The VIP compressed with 25 and 30 bar closely follow the simulation results with compression level 0 and 2 respectively, both with a relative error of 3.7 %. However, further work is needed to link the specific compression force to simulated compression levels in *YADE*. Furthermore, an offset of 3.5 mW/(m K) is added to correct for thermal bridging artifacts and power losses present in the measurement results.

5.4.4 ETC with a locally defined pore size

In order to overcome the previously mentioned limitations, the LBM heat transfer model was adjusted to include the calculation of the local pore size. The method for calculating the local pore distance is described in Chapter 3, Section 3.3.5. Similar to previous studies, to simulate the effective heat transfer through the three-dimensional

(a) *Measured ETC results.*   **(b)** *Simulated ETC results.*
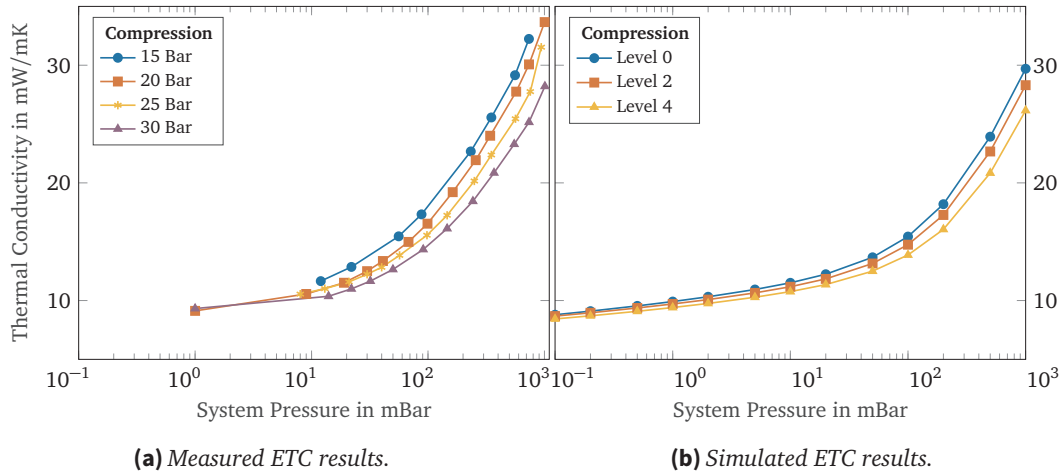
Figure 5.7: *Effect of compression forces on ETC, A) Measurement of the effect different compression forces on the thermal conductivity of the VIP. B) Simulation results of the effect of different compression forces on the thermal conductivity of the VIP (3.5 mW/mK is added to correct for thermal bridging artifacts in the measurement).*

packing of silica particles, the top (Γ_t) and bottom (Γ_b) boundaries are held at constant temperatures, 306.15 K and 305.15 K respectively. The remaining four boundaries are periodic, and the resolution of the simulation, N, is set to 16 lattice units per smallest particle diameter. ETC is composed of the conduction through the solid, gas as well as radiation.

In order to evaluate the simulation results, heat transfer is simulated over a range of pressures from 0.1 mbar up to 1 bar for silica sample GT. An example of a 3D packing of silica particles (GT) is shown in Figure 5.8 alongside the simulated temperature field. The ETC results are shown in Figure 5.9, as well as measured values of effective heat conductivity through VIPs with precipitated silica [50]. The measured VIPs contained pure precipitated silica without opacifiers and were measured at the same temperatures as the simulation.

While the effective heat transfer now closely predicts measured values at lower pressures (which was not the case in the previous study Section 5.4.1), an obvious and significant discrepancy is evident at higher pressures where the relative error is 34.5 %. This discrepancy is primarily due to the lack of larger pores, in the order of 200 nm and above, in the simulation geometry.

In addition to the precipitated silica sample GT, samples KS and CP were also numerically evaluated. Despite the lack of larger pores, the effective heat conductivities
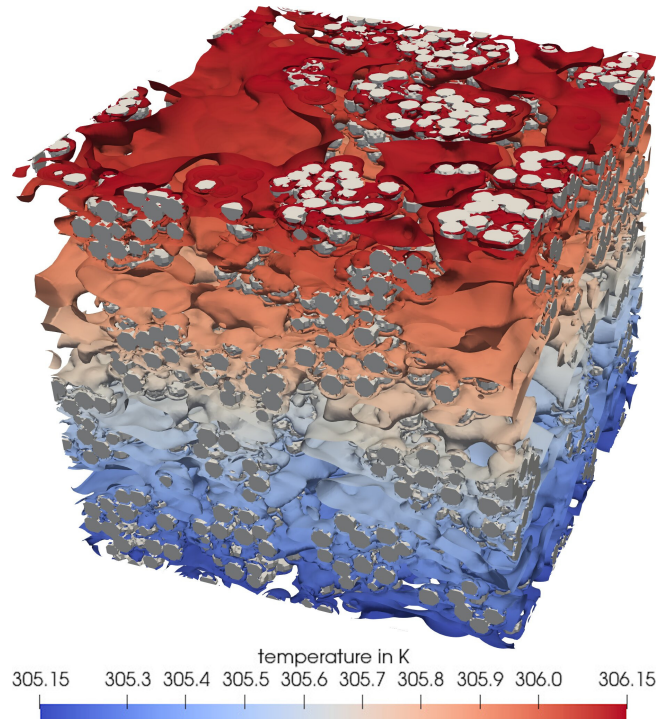
Figure 5.8: *Temperature distribution simulated through three-dimensional packing of silica particles (GT).*

predicted follow the trends reported in literature [75], with KS having the highest thermal conductivity at ambient pressure of $20.78\,\mathrm{mW/(m\,K)}$, followed by GT at $19.29\,\mathrm{mW/(m\,K)}$ and CP at $16.4\,\mathrm{mW/(m\,K)}$. These results are presented in Figure 5.10. The smaller particle sizes and equivalent aggregate sizes of the CP silica sample, leads to a smaller average pore size (as confirmed in 3.1) and decreased thermal conductivity at atmospheric pressure. The higher overall porosity of the GT silica sample but larger average pore size leads to lower thermal conductivities at lower system pressures.

5.5 Discussion and Outlook

Two sets of studies were performed to evaluate the suitability of the LBM models developed. In the first study, where a global pore size was defined and applied, the ETC was underestimated at lower system pressures. In order to remedy this artefact, a
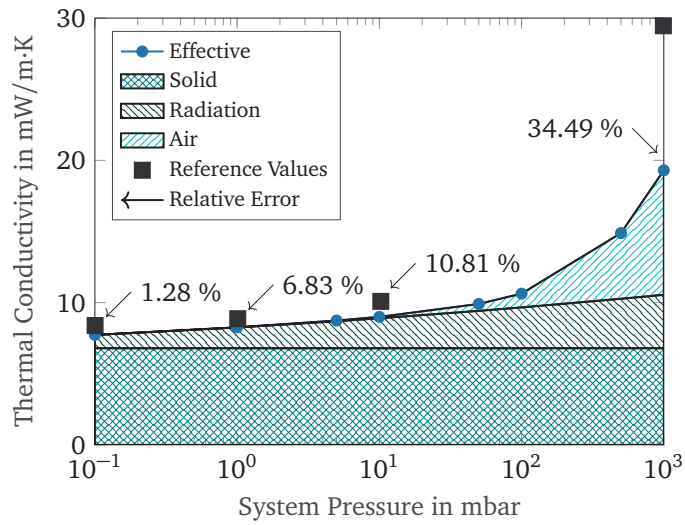
Figure 5.9: *Effective thermal conductivity simulated for the GT sample with a breakdown of components, compared with the measured thermal conductivity of a VIP with a medium of precipitated silica [50].*
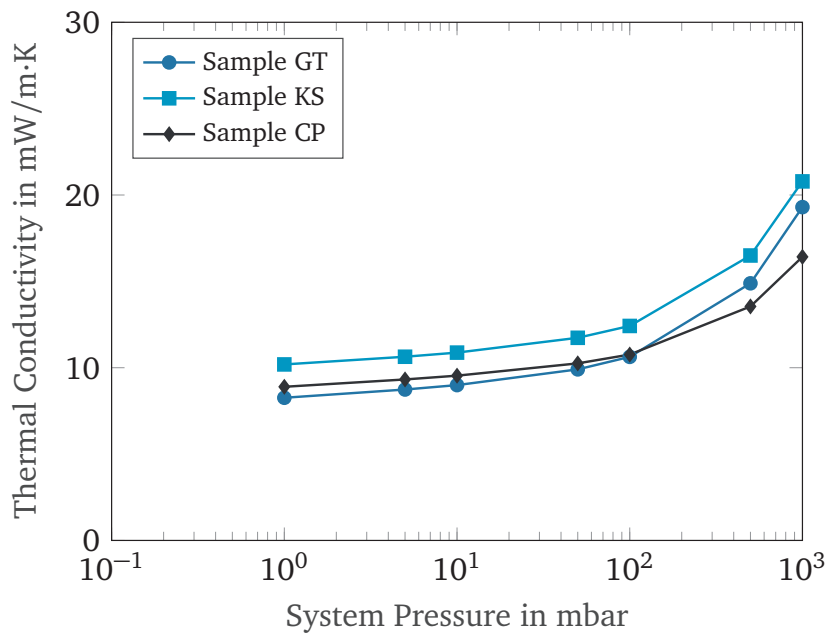
Figure 5.10: *ETC for silica samples GT, KS, and CP from 1 bar to 1 bar.*

local pore size calculation was implemented such that the local Knudsen number and consequent local heat transfer could be evaluated. This update to the methodology significantly improved the ETC at lower pressures, however due to the resulting shift towards smaller pores and the lack of larger pores, the resultant ETC estimation at higher system pressures yields lower ETC estimated values than those measured.

Future steps will be to overcome computational restrictions when simulating large pores while continuing to resolve the pore space within the silica aggregates (on the order of single nanometers). The large pores occur in the handling process of the silica medium during the manufacture of the VIPs. Not considering these larger pores leads to an underestimation of the effective heat transfer through the media at higher pressures. However, it is important to keep in mind that the reduction or complete absence of such pores is advantageous to the development of high performance VIPs which operate with low ETC at or just below ambient pressures. Moreover, in order to produce high efficiency VIPs, significant effort must be made during the manufacturing processes to ensure homogeneity of small pores throughout the VIP media, since as demonstrated, large pores and fissures in the VIP media result in increases of thermal conductivity. Although VIP still provide reduction of thermal conductivity over nano-porous materials, they require a vacuum to do so.

Other filler fluids such as Argon may also be numerically evaluated and their impact on the ETC compared to measured values. This may be achieved by adjusting the simulation variables as described in Chapter 4, Section 4.3.4. However, this may require the explicit consideration of coupling effects between particle if the gas to be studied has a higher thermal conductivity at certain pressures. The influence of the coupling effect may be studied by using the distance field and a morphological closing [71] to generate a new field with increased heat transfer between close proximity particles.

Using a slight variation on the proposed methodology, various additional structures can be imported as alternative aggregates to be included in the geometry packing study. Two example uses would be the ability to add structural fibers and/or opacifiers to the ETC numerical simulation. Structural fibers are commonly used to increase the mechanical stability of VIPs media. However, the fibers impact the thermal conductivity [19] negatively, requiring an optimum to be found between structural stability and ETC. From a radiative perspective, opacifiers are commonly used to decrease radiative thermal transfer, but these additional particles also impact the solid conductivity [36] negatively, again requiring an optimum to be found between reduction in radiative heat transfer and overall ETC. Since the methodology presented in this work relies

heavily on particles being spherical, the proposal is for long fibers to be generated as long thin series of overlapping spheres. In the case of opacifier particles, these would be generated in much the same way the silica aggregates are generated, as shown in Figure 3.1. The additional aggregates can be directly imported and compressed as described in Chapter 3, Section 3.3.4. Furthermore, by exporting the different particle types (silica, structural fibers and opacifiers) as individual XMLs, the geometries can be imported separately and their material properties adjusted in *OpenLB* during the simulation setup. By including fibers and opacifiers, an understanding is obtained not only of the overall impact on the effective thermal conductivity, but also into the effects on the local porosity of the silica media by analysing the pore size distribution as described in Chapter 3, Section 3.3.5.

Since this work presents an automated numerical method, featuring direct control and tuning of the micro-structure, optimization of the nano-porous geometry to minimize heat transfer may now be performed, by feeding back the simulated ETC to a grid search and gradient descent algorithm which control the parametric geometry [77]. By establishing an inverse problem, parameter optimization may be conducted to minimize heat transfer for different target temperatures, and additives. Constraints may also be placed on the input parameters to match commercially available silica. This step is facilitated by further improvements in computational performance, such as speed improvements obtained with GPU accelerated LBM-DEM implementations such as those demonstrated by Xiong et al. [84]. Moreover, by combining the numerical simulation and measurement data as an optimisation problem as described by Klemens et al. [45], additional insights regarding the porosity and particle size distributions of measured geometries can be obtained.

5.6 Conclusion

The goal of this chapter was to numerically evaluate the ETC through VIPs silica media using the aforementioned geometry and LBMs. The ETC results are comparable to both reference values and measured values over a range of system pressures. The outcome is an automated numerical method, featuring direct control and tuning of the micro-structure, to obtain a complete pathway from measured particle characteristics to the resulting effective macroscopic heat transfer.

6

Conclusions and Future Work

6.1 Summary

In this work, measurements of nano-silica particles using Static Light Scattering (SLS) were performed and used to characterize their size and form. A numerical simulation for spherical and ellipsoidal particles was developed to characterize the light scattering patterns based on shape and diameter. Thereafter, the primary particle size, primary pore size, aggregate diameter, shape and standard deviation, as well as overall packing porosity were used to drive a procedural workflow to generate mesoscopic geometries of precipitated silica. Heat transfer through these nano-porous geometries was simulated with Lattice Boltzmann Methods (LBMs), including the components due to radiation as well as to conduction through solid and fluid components. The local pore size was calculated in order to simulate local heat transfer through individual nano-pores. The simulation results were compared to physical measurement as well as to literature values. This culminates in an automated numerical method, featuring direct control and tuning of the desired micro-structure parameters, to obtain a complete methodological pathway from measured particle characteristics to the resulting effective macroscopic heat transfer.

6.2 Challenges Encountered

The following challenges are highlights of those which were encountered during the course of this work and can be considered the main achievements. They were mostly overcome through careful consideration and persistent discussions with supervisors and colleagues.

- Estimating particle diameter for silica particles 314 nm, 507 nm, 681 nm, 900 nm and 987 nm to within 5 % using very low laser power, for use in explosive environments and with minimal impact on the sample under study, posed challenges to be met. Estimation was accomplished through measurement of angle dependent light scattering with the use of high sensitivity Customized Photon Counting Modules (CPMs) in combination with development of an algorithm to compare measured and simulated light scattering signals which is independent of absolute intensity values. The method finds matches between both sets of data despite large variations in magnitude which is not achievable with least squares' based methods.

- Measuring angle dependent light scattering of particles with enough resolution to overcome aliasing was achieved through mechanical automation of the SLS measurements to measure from 20° to 160° in 2° increments.

- Developing an algorithm to evaluate the three dimensional normal vector at any given point of a continuous surface given only the information of whether a selected coordinate is inside or outside of the surface was challenge that required significant thought.

- Keeping the geometry generation fully parametric and based on measurements was a slow and iterative process. The final workflow includes measurements from Small Angle X-Ray Scattering (SAXS), Mercury Intrusion Porosimetry (MIP) and Analytical Ultracentrifugation (AUC) and encompasses the primary particle size, primary pore size, aggregate diameter, shape and standard deviation, as well as overall packing porosity. Implemented in the workflow are also additional inputs for primary particle size distribution, aggregate pore size distribution and particle contact area for when these measurements become available for the silica aggregates.

- Obtaining numerical particle geometries which were periodic required compressing the particles/aggregates with virtual particles mirrored across all axis (X, Y, Z as well as XY, XZ, YZ and XYZ). The final generated geometries are periodic in all axis directions.

- Generating particle aggregate forms based on SAXS mass fractal dimensions was realized by using predicates to model long cylindrical, disk-like and spherical forms. Moreover, SLS measurements and Montecarlo Light Scattering (MLS) simulations were performed to use light scattering to improve particle form measurements.

- Generating particle aggregate geometry with a defined pore size was realized by using a second particle system to model the pores and maintain the aggregates' internal porosity.

- Maintaining aggregate porosity during packing compression was achieved by applying rigid constrains to particles within an aggregate such that compression would take place between individual aggregates and not between particles within an aggregate.

- Verifying the results of the geometry generation was accomplished by calculating pore size and thereafter pore size distributions. Pore size was obtained through the evaluation of the euclidean distance to the surface followed by the removal of overlap from the resulting local maxima. The use of Delaunay triangulation for pore evaluation, on the other hand, was unsuccessful.

- Validating the numerically evaluated heat transfer against analytical solutions was not possible as these were not found in literature. Given this limitation, measurements of silica media parameters were taken, and also found in literature, and used to determine real heat transfer through the media, which were ultimately compared with the simulation results. At a system pressure of 0.1 mbar the relative error was 1.28 %.

6.3 Future Work

Building upon this work, the following topics are interesting future project ideas. These ideas have been described further in the relevant chapters and have been summarized here. Please refer to the discussion chapter of the corresponding topic for more detail.

Silica Measurements and Simulation

- Further testing of form estimation using the SLS apparatus and evaluation software to evaluate shape estimation accuracy.

- Implementing a real-time measurement system for feedback control of silicic acid precipitation to control silica particle diameter.

- Performing rigorous size classification, to separate the silica aggregates by size in order to evaluate aggregate size and form with SLS.

- Further development of curve matching algorithm, for example with Dynamic Time Warping (DTW) [21], to improve classification results.

- Considering diffracted and refracted rays separately in MLS to capture polarization effects.

- Including secondary intersections, allowing for not only concave particles, but also particle clusters.

Modeling and Generation of Silica Geometries

- Including measurements of the primary particle size distribution of the silica when they are available, directly in the aggregate generation workflow without changes to the software, to study its influence on the Effective Thermal Conductivity (ETC).

- Further studies to convert the calculated pore size distributions (based on the maximum inscribed sphere) to those measured by MIP, to add pore size distribution as a tunable parameter.

- Calculating the particle contact area and using the particle size overlap parameter in order to evaluate the impact on ETC.

- Studying the impact of additional structures, such as opacifiers and structural fibers, on the ETC to further optimize Vacuum Insulation Panel (VIP) for ETC performance and structural stability.

Lattice Boltzmann Methods

- Simulating larger geometries with larger pores (> 150 nm) to closer match physical measurements.

- Simulating using other filler gases to evaluate their overall impact on ETC for different applications and temperature ranges.

- Including slip boundaries to evaluate impact of natural convection or forced convection for evacuation on ETC.

- Evaluating the computational efficiency of two and three dimensional normal calculations to improve performance of the algorithms.

- Including a coupling term using the distance field for use with gases and/or media of higher thermal conductivity [28].

- Developing a multi-dimensional sensitivity analysis of input parameters on ETC.

> *It's the questions we can't answer that teach us the most. They teach us how to think. If you give a [person] an answer, all [they] gain is a little fact. But give [them] a question and [they'll] look for [their] own answers.*

Patrick Rothfuss

Bibliography

[1]   Michael Alberti et al. "Re-creating Hottel's emissivity charts for water vapor and extending them to 40 bar pressure using HITEMP-2010 data base". In: *Combustion and Flame* 169 (2016), pp. 141–153. DOI: `10.1016/j.combustflame.2016.04.013`.

[2]   A Multidisciplinary Approach. *Nearly Zero Energy Building Refurbishment*. 2013. DOI: `10.1007/978-1-4471-5523-2`.

[3]   Liliana de Luca Xavier Augusto et al. "Microfiber Filter Performance Prediction Using a Lattice Boltzmann Method". In: *Communications in Computational Physics* 23.4 (2018). DOI: `10.4208/cicp.OA-2016-0180`.

[4]   Ruben Baetens et al. "Vacuum insulation panels for building applications: A review and beyond". In: *Energy and Buildings* 42.2 (2010), pp. 147–172. DOI: `10.1016/j.enbuild.2009.09.005`.

[5]   A. Batard et al. "Modelling of long-term hygro-thermal behaviour of vacuum insulation panels". In: *Energy and Buildings* 173.June (2018), pp. 252–267. DOI: `10.1016/j.enbuild.2018.04.041`.

[6]   Serge Belongie. *Rodrigues' Rotation Formula*. Tech. rep. MathWorld–A Wolfram Web Resource, created by Eric W. Weisstein.

[7]   Axel Berge et al. "Literature Review of High Performance Thermal Insulation". In: *Civil and Environmental Engineering* 2 (2012), pp. 1–28.

[8]   Bjarne Stroustrup. "YADE Programming and Programs". In: (2015), p. 17. DOI: `10.5281/zenodo.34043`.

[9]   Blender Online Community. *Blender- a 3D modelling and rendering package*. Blender Foundation. 2018.

[10] Mathias Bouquerel et al. "Heat transfer modeling in vacuum insulation panels containing nanoporous silicas - A review". In: *Energy and Buildings* 54 (2012), pp. 320–336. DOI: 10.1016/j.enbuild.2012.07.034.

[11] A. M. Brasil et al. "Evaluation of the fractal properties of cluster-cluster aggregates". In: *Aerosol Science and Technology* 33.5 (2000), pp. 440–454. DOI: 10.1080/02786820050204682.

[12] K. Buchin et al. "Exact algorithms for partial curve matching via the Fréchet distance". In: *Proceedings of the Annual ACM-SIAM Symposium on Discrete Algorithms* (2009), pp. 645–654. DOI: 10.1137/1.9781611973068.71.

[13] Bing Yang Cao et al. "Molecular momentum transport at fluid-solid interfaces in MEMS/NEMS: A review". In: *International Journal of Molecular Sciences* 10.11 (2009), pp. 4638–4706. DOI: 10.3390/ijms10114638.

[14] Cheng-Yang Cao et al. "Experimental investigation on combustion behaviors and reaction mechanisms for 5-aminotetrazole solid propellant with nanosized metal oxide additives under elevated pressure conditions". In: *Applied Thermal Engineering* 162 (Nov. 2019), p. 114207. DOI: 10.1016/j.applthermaleng.2019.114207.

[15] F.K. Chan et al. "Feasibility Study of a Quadrilateralized Spherical Cube Earth Database". In: *Computer Sciences Corporation* 75 (1975).

[16] R. Coquard et al. "Modeling of Heat Transfer in Nanoporous Silica - Influence of Moisture". In: *8th International Vacuum Insulation Symposium 2007* 363 (). DOI: 10.1016/j.jnoncrysol.2012.11.053.

[17] R. Coquard et al. "Modelling of the conductive heat transfer through nano-structured porous silica materials". In: *Journal of Non-Crystalline Solids* 363.1 (2013), pp. 103–115. DOI: 10.1016/j.jnoncrysol.2012.11.053.

[18] Yan Jun Dai et al. "A theoretical model for the effective thermal conductivity of silica aerogel composites". In: *Applied Thermal Engineering* 128 (2018), pp. 1634–1645. DOI: 10.1016/j.applthermaleng.2017.09.010.

[19] Metin Davraz et al. "The Effect of Fiber, Opacifier Ratios and Compression Pressure on the Thermal Conductivity of Fumed Silica Based Vacuum Insulation Panels". In: *Arabian Journal for Science and Engineering* 41.11 (2016), pp. 4263–4272. DOI: 10.1007/s13369-016-2031-8.

[20]   Hu Dong et al. "Pore-network extraction from micro-computerized-tomography images". In: *Physical Review E - Statistical, Nonlinear, and Soft Matter Physics* 80.3 (2009), pp. 1–11. DOI: 10.1103/PhysRevE.80.036307.

[21]   Alon Efrat et al. "Curve Matching , Time Warping , and Light Fields : New Algorithms". In: *Journal of Mathematical Imaging and Vision* 27.1 (2007), pp. 203–216. DOI: 10.1007/s10851-006-0647-0.

[22]   Franck Enguehard. "Multi-scale Modeling of Radiation Heat Transfer through Nanoporous Superinsulating Materials". In: *International Journal of Thermophysics* 28.5 (Nov. 2007), pp. 1693–1717. DOI: 10.1007/s10765-006-0143-1.

[23]   European Commision. *2030 climate & enegry framework*. 2014. URL: https://ec.europa.eu/clima/policies/strategies/2030.

[24]   Wen-Zhen Fang et al. "Numerical predictions of thermal conductivities for the silica aerogel and its composites". In: *Applied Thermal Engineering* 115 (Mar. 2017), pp. 1277–1286. DOI: 10.1016/j.applthermaleng.2016.10.184.

[25]   Ihab Hanna Farag. "Radiative Heat Transmission from Non-Luminous Gases. Computational Study of the Emissivities of Water Vapor and Carbon Dioxide". In: (1976).

[26]   R W Fenn et al. "Optical and Infrared Properties of the Atmosphere". In: *Handbook of Geophysics and the Space Environment* (1985), pp. 1–80.

[27]   Jonas Fietz et al. "Optimized Hybrid Parallel Lattice Boltzmann Fluid Flow Simulations on Complex Geometries". In: *Lecture Notes in Computer Science (including subseries Lecture Notes in Artificial Intelligence and Lecture Notes in Bioinformatics)*. Vol. 7484 LNCS. 2012, pp. 818–829. DOI: 10.1007/978-3-642-32820-6_81.

[28]   Jochen Fricke et al. "Vakuum-Isolations-Paneele für Gebäude". In: *ZAE Bayern* (2007).

[29]   Maximilian Gaedtke et al. "Total enthalpy-based lattice Boltzmann simulations of melting in paraffin/metal foam composite phase change materials". In: *International Journal of Heat and Mass Transfer* 155 (July 2020), p. 119870. DOI: 10.1016/j.ijheatmasstransfer.2020.119870.

[30]   Shengyan Gao et al. "Two methods for pore network of porous media". In: *International Journal for Numerical and Analytical Methods in Geomechanics* 36.18 (Dec. 2012), pp. 1954–1970. DOI: 10.1002/nag.1134.

[31]   Tao Gao et al. "Thermal conductivity of amorphous silica nanoparticles". In: *Journal of Nanoparticle Research* 21.6 (2019). DOI: 10.1007/s11051-019-4556-8.

[32]   L Gatineua et al. "Surface area, mass fractal dimension, and apparent density of powders". In: *Journal of Colloid and Interface Science* 124.1 (2004), pp. 156–161. DOI: 10.1016/0021-9797(88)90336-0.

[33]   F A Govan et al., eds. *Thermal Insulation, Materials, and Systems for Energy Conservation in the '80s*. ASTM International, Jan. 1983. DOI: 10.1520/STP789-EB.

[34]   Zhaoli Guo et al. "Discrete effects on boundary conditions for the lattice Boltzmann equation in simulating microscale gas flows". In: *Physical Review E - Statistical, Nonlinear, and Soft Matter Physics* 76.5 (2007), pp. 3–7. DOI: 10.1103/PhysRevE.76.056704.

[35]   Dieter Hänel. "Molekulare Gasdynamik". In: (2004), p. 223. DOI: 10.1007/3-540-35047-0.

[36]   Ya Ling He et al. "Advances of thermal conductivity models of nanoscale silica aerogel insulation material". In: *Applied Thermal Engineering* 81 (2015), pp. 28–50. DOI: 10.1016/j.applthermaleng.2015.02.013.

[37]   U. Heinemann et al. "Radiation-conduction interaction : An investigation on silica aerogels". In: *International Journal of Heat and Mass Transfer* 39.10 (July 1996), pp. 2115–2130. DOI: 10.1016/0017-9310(95)00313-4.

[38]   D J Jacob. *Introduction to Atmospheric Chemistry*. Princeton University Press, 1999.

[39]   A. Kaemmerlen et al. "Radiative properties of extruded polystyrene foams: Predictive model and experimental results". In: *Journal of Quantitative Spectroscopy and Radiative Transfer* 111.6 (Apr. 2010), pp. 865–877. DOI: 10.1016/j.jqsrt.2009.11.018.

[40]   Simen Edsjø Kalnæs et al. *Vacuum insulation panel products: A state-of-the-art review and future research pathways*. Mar. 2014. DOI: 10.1016/j.apenergy.2013.11.032. URL: https://linkinghub.elsevier.com/retrieve/pii/S0306261913009264.

[41]   Ankang Kan et al. "A simple and effective model for prediction of effective thermal conductivity of vacuum insulation panels". In: *Future Cities and Environment* 1.0 (Aug. 2017), p. 4. DOI: 10.5334/s40984-015-0001-z.

[42]   Sungwook Kang et al. "Mechanism of heat transfer through porous media of inorganic intumescent coating in cone calorimeter testing". In: *Polymers* 11.2 (2019). DOI: 10.3390/polym11020221.

[43]   Jongmin Kim et al. "Vacuum insulation properties of glass wool and opacified fumed silica under variable pressing load and vacuum level". In: *International Journal of Heat and Mass Transfer* 64 (Sept. 2013), pp. 783–791. DOI: 10.1016/j.ijheatmasstransfer.2013.05.012.

[44]   Sedong Kim et al. "Experimental investigation of heat transfer coefficient with Al2O3 nanofluid in small diameter tubes". In: *Applied Thermal Engineering* 146 (Jan. 2019), pp. 346–355. DOI: 10.1016/j.applthermaleng.2018.10.001.

[45]   Fabian Klemens et al. "CFD-MRI: A coupled measurement and simulation approach for accurate fluid flow characterisation and domain identification". In: *Computers & Fluids* 166 (Apr. 2018), pp. 218–224. DOI: 10.1016/j.compfluid.2018.02.022.

[46]   Jae-Sung Kwon et al. "Effective thermal conductivity of various filling materials for vacuum insulation panels". In: *International Journal of Heat and Mass Transfer* 52.23-24 (Nov. 2009), pp. 5525–5532. DOI: 10.1016/j.ijheatmasstransfer.2009.06.029.

[47]   Sylvain Lallich et al. "Experimental Determination and Modeling of the Radiative Properties of Silica Nanoporous Matrices". In: *Journal of Heat Transfer* 131.8 (2009), p. 82701. DOI: 10.1115/1.3109999.

[48]   Klaus Langeheinecke et al. *Thermodynamik für Ingenieure*. Springer Fachmedien Wiesbaden, 2013. DOI: 10.1007/978-3-658-03169-5.

[49]   Jonas Lätt. "Hydrodynamic limit of lattice Boltzmann equations". In: *Science* 20.6 (2007), p. 124. DOI: 10.1016/j.future.2003.12.011.

[50]   Huiqiang Li et al. "Degradation of VIP barrier envelopes exposed to alkaline solution at different temperatures". In: *Energy and Buildings* 93 (2015), pp. 208–216. DOI: 10.1016/j.enbuild.2015.02.006.

[51]   Like Li et al. "Conjugate heat and mass transfer in the lattice Boltzmann equation method". In: *Physical Review E - Statistical, Nonlinear, and Soft Matter Physics* 89.4 (2014). DOI: 10.1103/PhysRevE.89.043308.

[52]   Duncan A. Lockerby et al. "Switching criteria for hybrid rarefied gas flow solvers". In: *Proceedings of the Royal Society A: Mathematical, Physical and Engineering Sciences* 465.2105 (2009), pp. 1581–1598. DOI: 10.1098/rspa.2008.0497.

[53] S. Lowell et al. *Characterization of Porous Solids and Powders: Surface Area, Pore Size and Density*. Vol. 16. Springer Netherlands, 2004. DOI: `10.1007/978-1-4020-2303-3`.

[54] A. L. Mackay. "To find the largest sphere which can be inscribed between four others". In: *Acta Crystallographica Section A* 29.3 (1973), pp. 308–309. DOI: `10.1107/S0567739473000768`.

[55] A.C. Marques et al. "Novel design and performance enhancement of domestic refrigerators with thermal storage". In: *Applied Thermal Engineering* 63.2 (Feb. 2014), pp. 511–519. DOI: `10.1016/j.applthermaleng.2013.11.043`.

[56] Manuel Meier et al. "Multi-scale characterization of precipitated silica". In: *Powder Technology* 354 (Sept. 2019), pp. 45–51. DOI: `10.1016/j.powtec.2019.05.072`.

[57] Albert Mink et al. "A 3D Lattice Boltzmann method for light simulation in participating media". In: *Journal of Computational Science* 17 (2016), pp. 431–437. DOI: `10.1016/j.jocs.2016.03.014`.

[58] A A Mohamad. *Lattice Boltzmann Method*. Springer London, 2011. DOI: `10.1007/978-0-85729-455-5`.

[59] Laven P. "MiePlot (A computer program for scattering of light from a sphere using Mie theory & the Debye series)". In: *http://www.philiplaven.com/mieplot.htm* (2011).

[60] Mikhail N. Polyanskiy. *Refractive Index Database*. (Visited on 03/26/2019).

[61] S Post. *Applied and Computational Fluid Mechanics*. Jones & Bartlett Learning, 2011.

[62] Scott Post. *Applied and Computational Fluid Mechanics*. Vol. 48. 01. 2010, pp. 48–0298–48–0298.

[63] Z. G. Qu et al. "Approach for predicting effective thermal conductivity of aerogel materials through a modified lattice Boltzmann method". In: *Applied Thermal Engineering* 132 (2018), pp. 730–739. DOI: `10.1016/j.applthermaleng.2018.01.013`.

[64] *Quarzglas Technisches Datenblat*. Tech. rep. Final Advanced Materials.

[65] Riyadh Al-Raoush et al. "Comparison of Network Generation Techniques for Unconsolidated Porous Media". In: *Soil Science Society of America Journal* 67.6 (2010), p. 1687. DOI: `10.2136/sssaj2003.1687`.

[66] Nadège Reboul et al. "A statistical analysis of void size distribution in a simulated narrowly graded packing of spheres". In: *Granular Matter* 10.6 (2008), pp. 457–468. DOI: 10.1007/s10035-008-0111-5.

[67] Denis Rochais et al. "Numerical simulation of thermal conduction and diffusion through nanoporous superinsulating materials". In: *Proceedings of the 17th European Conference on Thermophysical Properties* (2005).

[68] Jesse Ross-Jones et al. "Conjugate Heat Transfer through Nano Scale Porous Media to Optimize Vacuum Insulation Panels with Lattice Boltzmann Methods". In: *Computers and Mathematics with Applications* 77.1 (2019), pp. 209–221. DOI: 10.1016/j.camwa.2018.09.023.

[69] Jesse Ross-Jones et al. "Feasibility Study for a Chemical Process Particle Size Characterization System for Explosive Environments Using Low Laser Power". In: *Micromachines* 11.10 (Sept. 2020), p. 911. DOI: 10.3390/mi11100911.

[70] Jesse Ross-Jones et al. "Pore-Scale Conjugate Heat Transfer Simulations Using Lattice Boltzmann Methods for Industrial Applications". In: *Applied Thermal Engineering* (Sept. 2020), p. 116073. DOI: 10.1016/j.applthermaleng.2020.116073.

[71] Jean Serra. *Image Analysis and Mathematical Morphology*. Academic Press, Inc., 1983.

[72] Dmitriy Silin et al. "Pore space morphology analysis using maximal inscribed spheres". In: *Physica A: Statistical Mechanics and its Applications* 371.2 (2006), pp. 336–360. DOI: 10.1016/j.physa.2006.04.048.

[73] D. K. Singh et al. "Myo-inositol based nano-PCM for solar thermal energy storage". In: *Applied Thermal Engineering* 110 (2017), pp. 564–572. DOI: 10.1016/j.applthermaleng.2016.08.202.

[74] Václav Šmilauer et al. "Using and Programming". In: *Yade Documentation* (2015). DOI: 10.5281/zenodo.34043.

[75] Sebastian Sonnick et al. "Correlation of pore size distribution with thermal conductivity of precipitated silica and experimental determination of the coupling effect". In: *Applied Thermal Engineering* 150 (2019). DOI: 10.1016/j.applthermaleng.2019.01.074.

[76] Christopher M. Sorensen et al. "The prefactor of fractal aggregates". In: *Journal of Colloid and Interface Science* 186.2 (1997), pp. 447–452. DOI: 10.1006/jcis.1996.4664.

[77] V. Subramaniam et al. "Topology optimization of conjugate heat transfer systems: A competition between heat transfer enhancement and pressure drop reduction". In: *International Journal of Heat and Fluid Flow* 75 (Feb. 2019), pp. 165–184. DOI: 10.1016/j.ijheatfluidflow.2019.01.002.

[78] Tobias Teumer et al. "In-line haze monitoring using a spectrally resolved back scattering sensor". In: *BrewingScience* 71.5-6 (2018). DOI: 10.23763/BrSc18-06teumer.

[79] The Council of the European Union. *Council Directive 96/53/EC*. 1996. URL: https://eur-lex.europa.eu/eli/dir/1996/53/oj (visited on 10/15/2019).

[80] The Council of the European Union. *Directive (EU) 2015/719*. 2015. URL: https://eur-lex.europa.eu/eli/dir/2015/719/oj (visited on 10/15/2019).

[81] VDI e. V. *VDI-Wärmeatlas*. Springer Berlin Heidelberg, 2013. DOI: 10.1007/978-3-642-19981-3.

[82] Jinku Wang et al. "A lattice Boltzmann algorithm for fluid-solid conjugate heat transfer{star, open}{star, open}The present work was supported by the National Natural Science Foundation of China (Grant No. 59995550-2)." In: *International Journal of Thermal Sciences* 46.3 (2007), pp. 228–234. DOI: 10.1016/j.ijthermalsci.2006.04.012.

[83] Jinku Wang et al. "A lattice Boltzmann algorithm for fluid–solid conjugate heat transfer". In: *International Journal of Thermal Sciences* 46.3 (Mar. 2006), pp. 228–234. DOI: 10.1016/j.ijthermalsci.2006.04.012.

[84] Qingang Xiong et al. "Large-scale DNS of gas-solid flows on Mole-8.5". In: *Chemical Engineering Science* 71 (2012), pp. 422–430. DOI: 10.1016/j.ces.2011.10.059.

[85] Robert R Zarr et al. *Standard Reference Materials: SRM 1453, Expanded Polystyrene Board, for Thermal Conductivity from 281 K to 313 K*. Tech. rep. National Institute of Standards and Technology, Dec. 2012. DOI: 10.6028/NIST.SP.260-175.

[86] Hanfei Zhang et al. "Microencapsulation of molten salt in stable silica shell via a water-limited sol-gel process for high temperature thermal energy storage". In: *Applied Thermal Engineering* 136 (2018), pp. 268–274. DOI: 10.1016/j.applthermaleng.2018.02.050.

[87] Yannan Zhao et al. "Interaction of mesoporous silica nanoparticles with human red blood cell membranes: Size and surface effects". In: *ACS Nano* 5.2 (2011), pp. 1366–1375. DOI: 10.1021/nn103077k.

Appendix

A List of Figures

B List of Tables

C List of Source Code

D Source Code

The entirety of the code described in this work is available at:
"https://gitlab.com/jesserj/heattransfernanosilica/".

Additionally, the following code is available in the OpenLB git repository:

```
conjugateHeat3d_vip
└── conjugateHeat3d
```

The application *conjugateHeat3d_vip* has geometry files as well as scripts to run each
of the cases for simulating heat transfer through nano-silica. The commit hash is:
e75690ce9440e8d09f528fc0feca0182ec496f3e

```
testingNormal
├── testingNormal2d
├── testingNormal3d
└── testingNormal3d_cylinder
```

The applications for *testingNormal* are test cases for the two and three dimensional
normal. For two dimensions a circle test case is included. For three dimensions, sphere
and cylinder test cases are included. The commit hash is:
5ec461ba8f72fa7ee317c29d1307998441a61dd8

```
poiseuilleSlip_inclined2d
└── poiseuilleSlip_inclined2d
```

The application *poiseuilleSlip_inclined2d* is the test case for slip boundaries using a rotat-
ing cuboid. The commit hash is: dd7f8f7d1970de31928e80b0dc4e57d2e74c7d86